Nonnormal Perturbation Growth and Optimal Excitation of the Thermohaline Circulation using a 2D Zonally Averaged Ocean Model

by

Julie Alexander
B. Sc., University of Victoria, 1983
M. Sc., University of Victoria, 1985

A Dissertation Submitted in Partial Fulfillment
of the Requirements for the Degree of

DOCTOR OF PHILOSOPHY

in the School of Earth and Ocean Sciences

Nonnormal Perturbation Growth and Optimal Excitation of the Thermohaline Circulation using a 2D Zonally Averaged Ocean Model

by

Julie Alexander
B. Sc., University of Victoria, 1983
M. Sc., University of Victoria, 1985

Supervisory Committee

Dr. Adam Monahan, (School of Earth and Ocean Sciences)
Supervisor

Dr. Andrew Weaver, (School of Earth and Ocean Sciences)
Departmental Member

Dr. Ian Putnam (Department of Mathematics and Statistics)
Outside Member

Dr. John Fyfe (Canadian Center for Climate Modeling and Analysis)
Additional Member

Supervisory Committee

Dr. Adam Monahan, (School of Earth and Ocean Sciences)
Supervisor

Dr. Andrew Weaver, (School of Earth and Ocean Sciences)
Departmental Member

Dr. Ian Putnam (Department of Mathematics and Statistics)
Outside Member

Dr. John Fyfe (Canadian Center for Climate Modeling and Analysis)
Additional Member

Abstract

Generalized linear stability theory is used to calculate the optimal initial conditions that result in transient amplification of the thermohaline circulation (THC) in a zonally-averaged single basin ocean model. The eigenmodes of the tangent linear model verify that the system is asymptotically stable but the nonnormality of the system permits the growth of perturbations for a finite period through the interference of nonorthogonal eigenmodes. It is found that the maximum amplification of the THC anomalies occurs after 6 years with both the thermally driven and salinity driven components playing major roles in the amplification process. The transient amplification of THC anomalies is due to the constructive and destructive interference of a large number of eigenmodes and the evolution over time is determined by how the interference pattern evolves. It is found that five of the most highly nonnormal eigenmodes are critical to the initial cancellation of the salinity and temperature contributions to the THC while 11 oscillating modes with decay timescales ranging from 2 to 6 years are the major contributors at the time of maximum amplification. This analysis demonstrates that the different dynamics of salinity and temperature anomalies allows the dramatic growth of perturbations to the THC on

relatively short (interannual to decadal) timescales. In addition the ideas of generalized stability theory are used to calculate the stochastic optimals which are the spatial patterns of stochastic forcing that are most efficient at generating variance growth in the THC. It is found that the optimal stochastic forcing occurs at high latitudes and induces low-frequency THC variability by exciting the salinity-dominated modes of the THC. The first stochastic optimal is found to have its largest projection on the same five highly nonnormal eigenmodes found to be critical to the structure of the optimal initial conditions. The model's response to stochastic forcing is not controlled by the least damped eigenmodes of the tangent linear model but rather by the linear interference of these highly nonnormal eigenmodes. The process of pseudoresonance suggests that the nonnormal eigenmodes are excited and sustained by stochastically induced perturbations which in turn lead to maximum THC variance. Finally, it was shown that the addition of wind stress did not have a large impact on the nonnormal dynamics of the linearised system. Adding wind allowed the value of the vertical diffusivity to be reduced to achieve the same maximum linearised THC amplitude as was used in the case with no wind stress.

Table of Contents

List of Tables

List of Figures

Acknowledgements

I wish to thank my supervisor, Adam Monahan, for his positive feedback and guidance. I also thank my husband, Stewart Langton, for his unfailing support and encouragement and for enlightening conversations about the merits of completing this endeavour at this stage in my life.

I am also grateful to my sister Antoinette Oberg for her input and vast knowledge of the academic process and life long learning. Finally I would like to thank my parents Lewis and Antoinette Alexander for their continuous love and support.

Dedication

I dedicate this work to my father Lewis Woodson Alexander. His belief in the intrinsic value of education has inspired me to devote my life to studying and teaching. And his confidence that I could achieve whatever I set my mind to has enabled me to do exactly that.

.

Chapter 1

Introduction

1.1 Thermohaline circulation

The thermohaline circulation (THC) investigated in this study represents the zonally averaged Atlantic meridional overturning circulation (AMOC) (Wunsch 2002). The THC which spans the entire Atlantic on both hemispheres plays an important role in global climate variability because of its role in northward oceanic heat transport. There are four major processes associated with the THC that result in large volume (and heat) transport: upwelling (which transports volume from depth to near the ocean surface), surface currents (which transport relatively light water to high Northern latitudes), deep water formation (where water becomes dense and sinks) and deep currents that close the loop. Much of the total oceanic northward heat transport in the present-day Atlantic, estimated to be 1.2+/-0.3 PW at 24^{o}N (e.g. Gananchaud and Wunsch 2004), is due to the THC. This circulation system consists of two main overturning cells. The first cell is associated with the formation of North Atlantic Deep Water (NADW) in the Greenland-Iceland-Norwegian (GIN) Seas and the Labrador Sea. The freshly formed NADW flows over the shallow sill between Greenland, Iceland, and Scotland and is upwelled in the Southern Ocean. This upwelling is a consequence of the Ekman transport driven by strong westerly winds. In the Southern Ocean some NADW is exported to other oceans while some travels around Drake Passage and mixes with lighter Antarctic Intermediate Water (AAIW) which is thought to form most intensively around the southern tip of South America. The second cell is associated with the formation of Antarctic Bottom Water

(AABW), which originates in the Wedell and Ross seas, flows north in the deep layers of the ocean, mixes with NADW and returns to the Southern Ocean.

The major driving mechanism for the THC is mixing that transports heat from the surface to the deepwater masses crossing surfaces of equal density (diapycnal mixing). Winds and tides generate internal waves that break and cause turbulent mixing in the ocean. At low latitudes this mixing of heat to the deeper ocean causes the density of the water to decrease and the water to rise to the surface. This warm water is then advected poleward into the North Atlantic where atmospheric cooling and salt rejection during sea ice growth causes an increase in the density and subsequent sinking. These deep water masses then spread and flow southward in the intermediate and deep layers of the ocean. This circulation system therefore creates a meridional density gradient between high and low latitudes.

Evidence from general circulation model (GCM) simulations (Manabe and Stouffer 1999) and paleoproxies (Clark et al. 2002, O'Hare et al. 2005) suggest that variations in the intensity of the THC are likely to change the climate significantly. The mild climate in Northwestern Europe relative to northwestern North America is primarily due to the heat transported by the THC; thus a reduction in the THC strength has strong implications for the climate in this region. Changes in the strength of the THC may also impact the El Nino-Southern Oscillation (e.g. Timmermann et al., 2005), the position of the Intertropical Convergence Zone (e.g. Vellinga and Wood, 2002), the marine ecosystem in the Atlantic (e.g. Schmittner, 2005), and sea level in the North Atlantic (e.g. Levermann et al., 2005). For these reasons the variability and stability of the THC is a subject of considerable scientific interest (e.g. Wood et al. 2003, Meehl et al. 2007).

Fluctuations in the intensity of the THC occur over a wide range of space and time scales ranging from hundreds to thousands of kilometers and from decades to millennia respectively. The timescales of the variability of the THC are influenced by many processes including Rossby wave dynamics, advection by the mean flow, convection, the hydrological cycle and atmospheric forcing. In general, the decadal timescale of the THC variability is related to the time required to advect surface density anomalies from the middle to the high latitudes. This process moves water from regions of upwelling into regions of downwelling where it affects the THC (Weaver et al. 1993, Saravanan and McWilliams 1997, Vellinga and Wu 2004, Sevellec et al. 2006). While no single mechanism of decadal-centennial THC oscillations has been identified the presence of variability has been shown to be robust to changes over a wide range of relevant model parameters such as wind stress forcing (Chen and Ghil 1995, Huck et al. 2001), model resolution (Fanning and Weaver 1998) and buoyancy forcing (Pierce et al. 1995), although details such as the dominant timescales are much more model dependent. Modeling studies of the THC have proposed three mechanisms to explain the variability of the THC: (a) damped modes of the uncoupled ocean that are stochastically excited by atmospheric variability, (b) unstable modes of the uncoupled ocean that express themselves spontaneously; and (c) unstable or weakly damped coupled modes of the ocean-atmosphere system.

This study focuses on models of the THC which fall into the first of the above classes. Such systems are characterised by fixed points (steady states) with local linearised dynamics such that perturbations are asymptotically stable. That is, all (sufficiently small) perturbations of the system away from the fixed point eventually

decay to zero amplitude. Traditional linear stability theory characterises the asymptotic stability properties of fixed points through the analysis of the eigenstructure of the locally linearised dynamics (e.g. Pedlosky 1987). In such studies, the focus is on the long-time behavior of the system; transient behavior of perturbations is not considered. In fact, it is possible for perturbations to stable linear systems to grow substantially in amplitude (by potentially orders of magnitude) over finite times before eventually decaying; this phenomenon is referred to as transient amplification (Trefethen and Embree 2005). Mathematically speaking, transient amplification of perturbations to a linear system are only possible if the linear dynamical operator A is nonnormal – that is, if it does not commute with its adjoint ($AA^T - A^T A \neq 0$, where A^T is the complex transpose of A). It is possible to diagnose those perturbations to a linear system which display the most pronounced transient amplification over finite times; these so-called "optimal perturbations" represent the directions of greatest sensitivity to forcing and are therefore dynamically important (Farrell and Ioannou 1996). In particular, they generally play an important role in determining the response of a linear system to sustained stochastic forcing – in the present case, the response of the THC to fluctuating atmospheric forcing.

Nonnormality is the rule rather than the exception in geophysical fluid dynamics linearised around steady states. In the past two decades the ramifications of the idea that the atmosphere is a nonnormal system have been explored mainly by Farrell and his coworkers on topics such as midlatitude cyclogenisis (Farrell 1982a, b, 1984, 1985, 1988, 1989), the dynamics of midlatitude atmospheric jets (Farrell and Ioannou 1995), the atmospheric energy spectrum (Farrell and Ioannou 1993d), quasigeostrophic turbulence (DelSole 1996, 1999), forecast error growth in atmospheric models (Farrell 1990, Mureau

et al. 1993, Molteni et al. 1993), atmospheric predictability and ensemble weather prediction (Lorenz 1965, Lacarra and Talagrand 1988, Ferranti et al. 1990, Errico et al. 1993, Buizza and Palmer 1995) and climate variability (DelSole and Hou 1999). Applying generalized stability theory to oceanic problems has been a more recent endeavor with the majority of the work involving different aspects of the El Nino-Southern Oscillation (ENSO) (e.g. Moore and Kleeman 1996, 1997a, b, 1999a, b, 2001, Kleeman and Moore 1997, 1999, Penland 1989, 1996, Penland and Sardeshmukh 1995a, b and Zavala-Garay et al. 2003) and the wind driven circulation (e.g. Moore et al. 2002 and Chhak et al. 2006a, b).

The focus of this study is the transient amplification and response to stochastic surface forcing of THC anomalies due to nonnormal dynamics. In this context the Wright and Stocker 2D zonally averaged ocean (WS) model is represented as a linearly damped (stable) system which displays no variability unless forced externally. Previous studies have considered the nonnormal dynamics of the THC in models of varying complexity such as Stommel's 2 box model (Lohmann and Schneider 1999), a 3 box model (Tziperman and Ioannou 2002), a two dimensional coupled box atmosphere-ocean model (Zanna and Tziperman 2005), a 2D latitude-depth ocean THC model (Sevellec et al. .2007) and the GFDL coupled atmosphere-ocean GCM CM2.1 (Tziperman et al. 2008). This study differs from these earlier studies in that it uses a more complex model than the box models, it considers temperature and salinity dynamics (while Sevellec et al. (2007) only considers salinity dynamics) and it explores optimal initial conditions as well as stochastic optimals (while Tziperman et al. (2008) calculate only the optimal initial conditions using the techniques of inverse modeling).

1.2 Outline of research

The next chapter (Chapter 2) reviews generalized stability theory. The consequences of the nonnormality of the system and the mechanism responsible for transient growth of perturbations are discussed.

Chapter 3 describes the Wright and Stocker 2D zonally averaged model used in this study, and the manner in which the linearised operator is obtained.

The initial temperature and salinity perturbations that lead to maximum transient growth of THC perturbation amplitude in the WS model, referred to as the optimal initial conditions are presented in Chapter 4. The eigenmodes that dominate the transient growth process are also investigated in this chapter.

In Chapter 5 the spatial patterns of stochastic surface forcing that lead to maximum variance of the THC norm, referred to as the stochastic optimals are calculated. The relationship between the optimal initial conditions and the stochastic optimals is also explored.

The effects of adding wind stress to the WS model on the nonnormal dynamics of the system are examined in Chapter 6.

Chapter 7 concludes this dissertation with all major results highlighted. Also included in this chapter are suggestions for future research that could provide insight into the stability and variability of the THC.

Chapter 2

Generalized stability theory

2.1 Introduction

The variability of the THC considered in this study is assumed to be of sufficiently small amplitude that it can be characterised as a stable linear dynamical system. Recent observations from 2004-2005 of the variability of the maximum meridional overturning from the Rapid Climate Change (RAPID) mooring array indicate that the transport at 26.5^{o}N has a standard deviation of 5.6 Sv (1 Sv $=1.0X10^{6}m^{3}s^{-1}$) around the mean value of 18.7 Sv on subannual timescales (Cunningham et al. 2007) however, because these are local measurements not all of this variability is expected to be relevant to basin-scale THC variability. In a study by Mysak et al. (1993) the response of the WS model to a 0.1 Sv random freshwater flux was considered. They found that the large positive overturning cell in the North Atlantic was generally stable with the amplitude of the perturbation response of the streamfunction less than 10% of the time mean of the maximum streamfunction for a wide range of horizontal and vertical diffusivities. This modest amplitude response to a relatively large fluctuating forcing justifies the consideration of linearised dynamics in the WS model. The focus on linear dynamics means that this work will not encompass the full range of dynamics relevant to large-amplitude THC fluctuations such as the jumps between different equilibria induced by stochastic forcing such as those found in idealized models by Cessi (1994), in an OGCM by Weaver and Hughes (1994) and in the WS model by Aeberhardt et al. (2000) or the switching between positive and negative THC cells found in the GCM study of Weaver et

al. (1991). However, linear dynamics can be expected to yield insight into THC variability on timescales ranging from interannual to centennial. Schmidt and Mysak (1996) showed that in a large region of WS model parameter space stochastically forced oscillations of the THC with century-scale periods could be accurately represented by resonant modes of a linearised model. Using a simple box model damped linear THC oscillations excited by stochastic atmospheric forcing were studied by Griffies and Tziperman (1995). They concluded that their linear interpretation of the dominant oscillating mode was sufficient for understanding the mechanism accounting for stochastically forced variability of the THC. Using linear stability analysis Saravanan and McWilliams (1997), Huck and Vallis (2001) and Kravtsov and Ghil (2004) attributed the decadal oscillation of the THC found in their models to a linearly unstable or weakly damped eigenmode of the system excited by atmospheric noise. In general the traditional 2D zonally averaged models with constant surface fluxes do not exhibit self-sustained variability of the THC (Huck et al. 1999). Most previous systematic studies of linearised THC dynamics employed traditional linear stability theory, which focuses on the eigenmodes of the tangent linear operator (that is, the nonlinear dynamical operator linearised around some steady state) and searches for perturbations that grow or decay exponentially with time (e.g. Pedlosky 1987), to characterise the stability of the THC dynamics. Traditional linear stability theory focuses on the long-term behavior of the linearised system. If all of the eigenvalues of the tangent linear operator are negative, then the system is asymptotically stable and all small perturbations applied to the steady state will decay to zero as $t \to \infty$. If the tangent linear operator possesses at least one

eigenvalue with a positive real part, then small perturbations will grow exponentially and the tangent linear dynamical system is considered to be unstable in the asymptotic limit.

A different approach to exploring the growth and decay of perturbations in a linear dynamical system, known as generalized stability theory (Farrell and Ioannou 1993, Farrell and Ioannou 1996), considers the evolution of perturbations to a linear system over finite times. Transient growth of a perturbation is possible if the linear operator governing the dynamics is nonnormal, that is, if it does not commute with its adjoint $AA^T - A^T A \neq 0$ (note for a finite dimensional matrix operator the adjoint is given by the Hermitian transpose). In contrast to normal operators (which by definition commute with their adjoint), the eigenvectors of nonnormal operators are not orthogonal in general and standard eigenvalue methods may fail to characterise the linearised dynamics over finite times. Recently it has been recognized that the property of nonnormality in the governing matrix operator of a linear system can lead to a rich variety of behavior. In particular, when a nonnormal operator possesses all negative eigenvalues the transient behavior may differ entirely from the asymptotic behavior suggested by the eigenvalues alone. This type of system can support rapid perturbation growth due to the linear interference of several nonorthogonal eigenmodes. Fields of study where nonnormality of the dynamics has been demonstrated to be important include: hydrodynamic instability, matrix iterations, meteorology, Markov chains, control theory, and analysis of high-powered lasers (e.g. Trefethen and Embree, 2005).

The importance of nonnormality in geophysical fluid dynamics has been recognized for many years. After Butler and Farrell (1992) made the startling discovery that small

perturbations to Couette flows may be amplified by factors of many thousands even in an asymptotically stable system the use of generalized stability theory began to appear more frequently in the literature (as discussed in detail in Chapter 1). In an important 1996 paper, Farrell and Ioannou laid out most of the results of generalized stability theory used in this study.

2.2 Theory

The focus of generalized stability theory is the growth and decay of solutions to a linear dynamical system governed by an autonomous (i.e. time independent) matrix operator A. The differential equation can be written as $\frac{dP}{dt} = AP$ whose solution is $P(t) = e^{tA}P(0) = B(t)P(0)$. The matrix $B(t) = e^{tA}$ is called the propagator of the system because it propagates the perturbation vector $P(t)$ forward in time. The central distinguishing feature of A is its normality or nonnormality. If A is normal (i.e. commutes with its Hermitian transpose) then it has a complete set of orthogonal eigenvectors and the growth and decay of perturbations is governed by it eigenvalues. Eigenvalues with negative real part govern steadily decaying perturbations while eigenvalues with positive real part correspond to exponentially growing perturbations. If A is nonnormal its eigenvectors are nonorthogonal and transient growth of perturbations can occur due to the linear interference of these eigenvectors.

A measure of perturbation growth of P_0 over time τ can be written

$$\lambda = \frac{M(\tau)}{M(0)} = \frac{(P(\tau), P(\tau))}{(P_0, P_0)} = \frac{(e^{A\tau}P_0, e^{A\tau}P_0)}{(P_0, P_0)} = \frac{(e^{A^T\tau}e^{A\tau}P_0, P_0)}{(P_0, P_0)} \quad (2.1)$$

where $M(\tau)$ is the norm of the perturbation and $(\bullet,\bullet)$ is the inner product in the Euclidean norm. It follows that growth of perturbations in nonnormal systems is determined by the eigenanalysis of the symmetric matrix $e^{A^T\tau}e^{A\tau} = B^T(\tau)B(\tau)$. The linear superposition of eigenmodes that yields the fastest growing perturbation with respect to a given norm and time interval is called an "optimal perturbation" (Farrell and Ioannou 1996). The optimal perturbation for the optimization time τ is the first right singular vector of $B(\tau)$ or equivalently, the eigenvector of $B^T(\tau)B(\tau)$ with largest eigenvalue. This vector will be referred to as P_0, the optimal initial condition that leads to the maximum transient growth of $P(t)$.

Perturbation growth is equivalently measured by the norm of the propagator $\left\|e^{tA}\right\|$, (where || || indicates the spectral norm of a matrix that is defined to be the largest singular value of the matrix). As $t \to 0$ the norm of the propagator is governed by the numerical abscissa, $\alpha(A)$., defined to be the maximum eigenvalue of $(A+(A^*)^T)/2$ (Farrell and Ioannou 1996). This implies that $\left\|e^{tA}\right\|$ behaves like $e^{\alpha(A)t}$ as $t \to 0$. The asymptotic behavior is governed by the spectral abscissa, $\omega(A)$, defined to be the eigenvalue of A with maximum real part such that $\left\|e^{tA}\right\|$ behaves like $e^{\omega(A)t}$ as $t \to \infty$. The relevant timescales of transient growth lie between these asymptotic limits. The structures and timescales of the perturbation vector at these intermediate times are found from singular value decomposition of the propagator.

If $P(t)$ is not a quantity of physical interest such as energy, enstrophy, vorticity etc. then new variables must be chosen and a new dynamical operator must be defined. For example, if the transient growth of the physical quantity defined as $U(t) = G^T P(t)$ is to be investigated then the governing differential equation can be written $dU(t)/dt = CU = G^T A(G^T)^{-1}U$ with $X = GG^T$ a symmetric positive definite matrix and $C = G^T A(G^T)^{-1}$ the governing matrix whose nonnormality determines the transient growth behavior (Moore et al. 2002). The optimal initial condition in this case is the eigenvector of $B^T(\tau)XB(\tau)$ with largest eigenvalue. A measure of perturbation growth or decay is the factor by which the norm changes over the time interval τ, and is given by

$$\lambda = \frac{M(\tau)}{M(0)} = \frac{P^T{}_0 B^T(\tau) XB(\tau) P_0}{P^T{}_0 XP_0} \tag{2.2}$$

where $B(\tau)$ is the propagator of the tangent linear equation. The optimal perturbation is the perturbation that yields the largest value of λ subject to the constraint that the norm $M(0) = 1$. According to the Rayleigh–Ritz method, the optimal perturbation is the eigenmode of $B^T(\tau)XB(\tau)$ with largest eigenvalue (Moore et al. 2003). The initial conditions P_0 leading to an optimal growth at time τ are therefore the generalized eigenvectors of the generalized eigenvalue problem

$$B(\tau)^T XB(\tau)P_0 = \lambda XP_0 \quad \textit{subject to } P_0{}^T XP_0 = 1 \tag{2.3}$$

The eigenvalue spectra of A and A^T are identical each having eigenvalues that occur in complex conjugate pairs. Let $\{\lambda_n, \hat{s}_n\}$ and $\{\sigma_n, \hat{r}_n\}$ be the {eigenvalue, eigenvector} sets of A and A^T respectively, where $\lambda_n{}^* = \sigma_n$, and * denotes complex conjugate. $\hat{r}_k$ is the

k^{th} eigenmode of A^T and is referred to as the biorthogonal of $\hat{s}_k$, the eigenvector that is orthogonal to all other eigenvectors. The biorthogonality property between the eigenmodes of A and A^T can be stated as

$$\hat{s}_n^T \hat{r}_m (\lambda_n - \sigma_m^*) = \hat{s}_n^T \hat{r}_m (\lambda_n - \lambda_m) = 0 \tag{2.4}$$

so $\lambda_n = \lambda_m$ for $n = m$ and $\hat{s}_n^T \hat{r}_m = 0$ for $n \neq m$. The optimal initial condition can be written as a linear superposition of the eigenmodes with projection coefficients a_k.

$$P_0 = \sum_{k=1}^{N} a_k s_k \tag{2.5}$$

The amplitude of the k^{th} eigenmode is (Farrell and Ioannou 1996)

$$a_k = \hat{r}_k^{\,T} P_0 / \hat{r}_k^{\,T} \hat{s}_k \tag{2.6}$$

The degree of nonorthogonality of any eigenmode with the remaining members of the eigenspectrum can be quantified by the secant of the angle φ between the eigenmode and its biorthogonal. This quantity can be written as

$$\nu(k) = \left|\hat{s}_k\right| \left|\hat{r}_k\right| / (\hat{r}_k^{\,T} \hat{s}_k) \tag{2.7}$$

(Farrell and Ioannou 1996) and interpreted as a measure of the linear dependence of $\hat{s}_k$ on the remaining members of the eigenspectrum. Large values of ν_k indicate a high degree of linear dependence or a high degree of nonorthogonality of $\hat{s}_k$ with other members of the spectrum.

In mathematical terms, the nonnormality of the linear tangent matrix is a result of the lack of commutivity with its Hermitian transpose; such linearised dynamical operators are the rule rather than the exception in realistic geophysical systems.

Nonnormality occurs when the basic state has nonzero shear and/or deformation. It also occurs whenever the coupling between physical components is anisotropic; e.g., the atmosphere-to-ocean coupling differs from the ocean-to-atmosphere coupling (Moore and Kleeman 1999). Moore and Kleeman (1999) used an intermediate coupled ocean-atmosphere model to identify five factors that contribute to the nonnormality of their system in the Tropics. They were (i) nonsolar atmospheric heating due to changes in SST, (ii) the dissimilarity between the equatorial ocean wave reflection process at eastern and western boundaries, (iii) ocean surface wind stress, (iv) upper-ocean thermodynamics, and (v) dissipation. In a study of the wind-driven ocean circulation in the North Atlantic Chhak et al. (2006) identified sources of nonnormality as gradients in the bathymetry, regions of potential vorticity gradients associated with circulation features like the Gulf Stream, and continental boundaries, all of which act as Rossby wave generators. More generally, Moore et al. (2002) and Aiken et al. (2002) attributed the nonnormal character in their geophysical systems to the shear and strain in the basic-state flow. In ocean models a common source of nonnormality is the advection and diffusion equations for temperature and salinity. Mathematically such equations contain a combination of both gradient and Laplacian operators. For problems with constant coefficients and unbounded domains the resulting operator is normal however, when boundaries or variable coefficients are introduced the operator becomes nonnormal. It the diffusion is weak relative to the advection then the nonnormality is typically of magnitude $O(C^{1/\eta})$ for some $C>1$ where η is the diffusion parameter whose inverse is known as the Peclet number (Trefethen and Embree 2005).

2.3 A two-dimensional example

In the following Chapters of the thesis all of these ideas will be applied to an 800 by 800 dimensional matrix that represents the linearised 2D zonally averaged WS ocean model. To help establish a basic conceptual framework for understanding these following results, a simple two-dimensional example of nonnormal dynamics (building on a similar analysis presented in Farrell and Ioannou (1996)) will now be presented. Although this example is illustrative of many important concepts that are crucial to the understanding of the results of this research it should be noted that this depiction of transient growth is greatly simplified; in large geophysical systems, generally many of the eigenmodes are oscillatory (resulting in complex eigenvalues) which influences the linear interference process and may result in weaker transient amplification than is seen in this illustrative example.

Assume that the tangent linear operator for this two dimensional system is

$$A = \begin{bmatrix} -0.1 & -0.9\cot(\theta) \\ 0 & -1 \end{bmatrix} \tag{2.8}$$

This matrix is stable with eigenvalues $\lambda_1 = -0.1$ and $\lambda_1 = -1$, and eigenvectors $\hat{s}_1 = (1,0)$ and $\hat{s}_2 = (\cos\theta, \sin\theta)$. Each eigenvector is a purely decaying vector with the decay rate of the second eigenvector ten times the rate of the first. The angle between the two eigenvectors is θ, therefore the eigenvectors are orthogonal only if θ=π/2; in this case the matrix is normal and transient growth cannot occur. For any other choice of θ the eigenvectors are nonorthogonal and the resulting matrix is thus nonnormal. The propagator is

$$B(t) = e^{At} = \begin{bmatrix} e^{-0.1t} & (e^{-t} - e^{-0.1t})\cot(\theta) \\ 0 & e^{-t} \end{bmatrix} \tag{2.9}$$

The perturbation growth as measured by $\left\| e^{tA} \right\|$ as a function of time for $\theta = [\pi/100, \pi/10, 4\pi/5]$ is shown in Figure 2.1. The times of maximum growth (optimization times) for these three angles are $\tau = [2.6, 2.4, 2.0]$. The curves in Figure 2.1 also demonstrate the relationship between the magnitude of transient growth and the nonorthogonality of eigenvectors. The further the eigenvectors are away from being orthogonal the larger the transient growth. When the eigenvectors are very close to parallel (or antiparallel) there is very large transient growth, when the eigenvectors are orthogonal there is no transient growth.

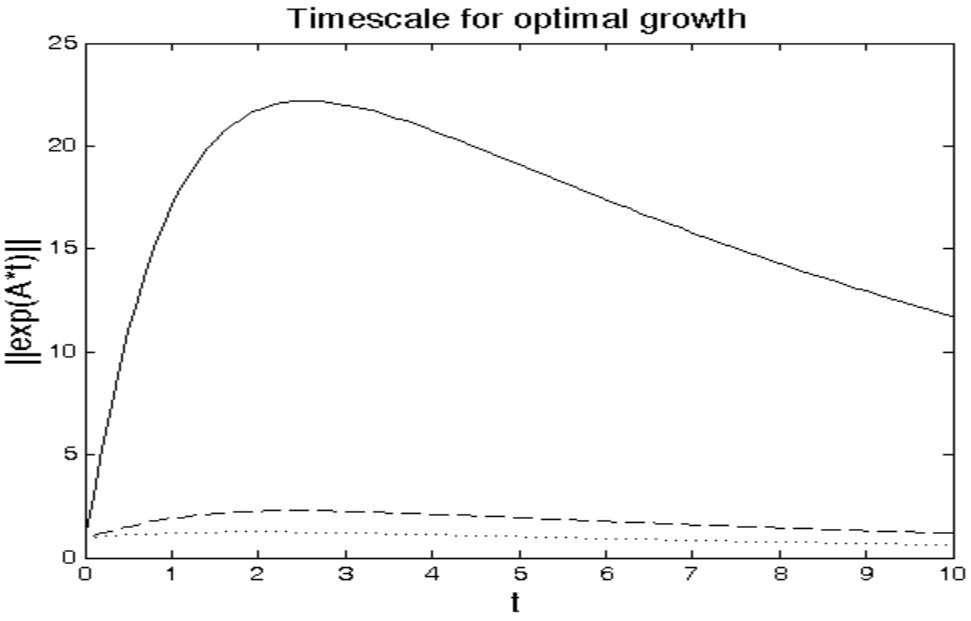

Figure 2.1. Norm of the propagator for the simple two-dimensional nonnormal matrix example with $\theta = \pi/100$ (solid line), $\theta = \pi/10$ (dashed line) and $\theta = 4\pi/5$ (dotted line).

The rest of the discussion of transient growth of perturbations in this two-dimensional example will use $\theta = 4\pi/5$ and the corresponding optimization time of 2.0. This value was chosen because it is an example of highly nonorthogonal eigenvectors. The optimal initial condition is the eigenvector of $B^T(2)B(2)$ with largest eigenvalue, namely $P(0) = (0.65, 0.76)$. The projection coefficients defined in Eq. (2.5) in this case are $a_1 = 1.70$ and $a_2 = 1.29$. Figure 2.2 shows snapshots of the evolution of the optimal initial perturbation for $t = 0,1,2,3$. It can be seen that as $\hat{s}_2$ decays at ten times the rate of $\hat{s}_1$ the perturbation vector amplifies to its maximum at the optimization time of 2 and then decays as it approaches the least damped eigenmode of the system. It should also be noted that both of the coefficients a_1 and a_2 are functions of time. This means that in large dimensional systems the eigenvectors that have large projections onto the optimal initial conditions may not have large projections on the perturbation vector at the time of maximum amplification. This becomes an important point in Chapter 4 when the relevant eigenmodes for the amplification of THC perturbations are determined.

The concept of ν_k defined in Eq. (2.6) as a measure of nonorthogonality of $\hat{s}_k$ with other members of the spectrum is illustrated in Figure 2.3. In Figure 2.3a) φ=0 and $\nu_k = 1$ therefore $\hat{s}_k$ is orthogonal to all other eigenvectors $\hat{s}_j$. In Figures 2.3b) and 2.3c) as φ increases ν_k also increases such that $\nu_k \to \infty$ as $\varphi \to \pi/2$.

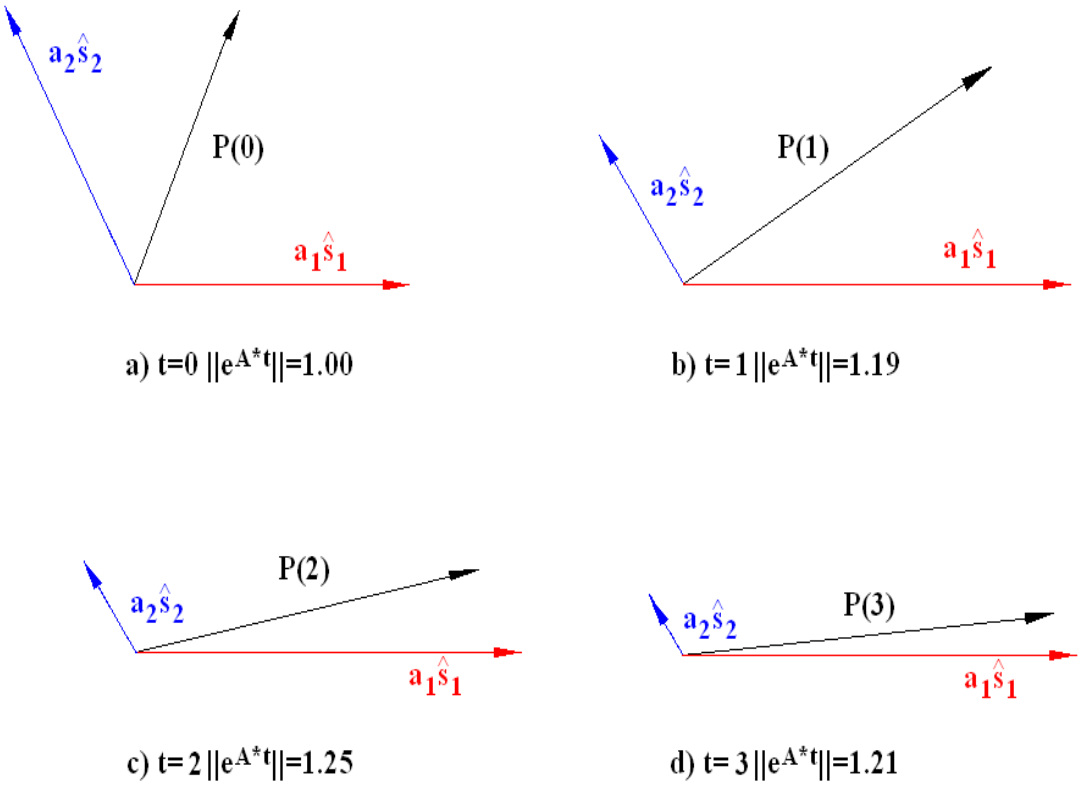

Figure 2.2. Evolution of the perturbation vector $P(t)$ (black line) and its components $a_1\hat{s}_1$ (red line) and $a_1\hat{s}_1$ (blue line) at times a) t=0, b) t=1, c) t=2, and d) t=3. For each time the norm of the propagator which is a measure of the transient amplification is given.

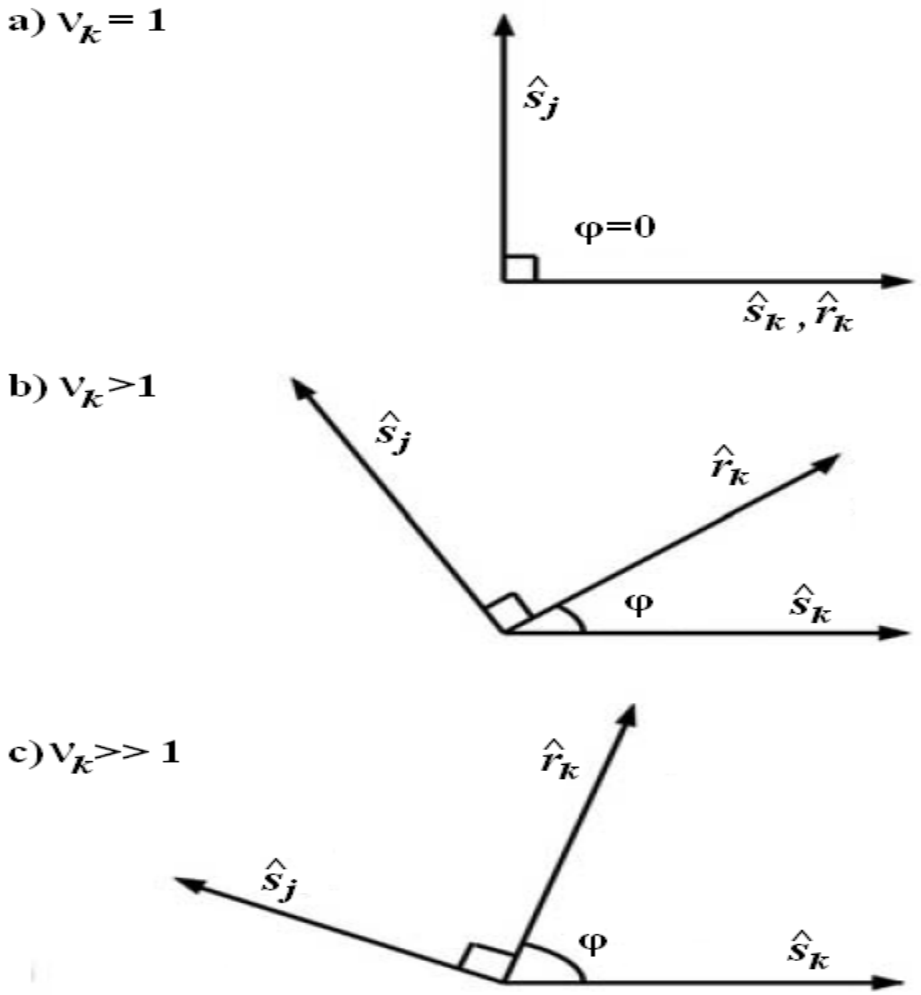

Figure 2.3. Demonstration of ν_k as a measure of the nonorthogonality of any eigenmode $\hat{s}_k$ on the remaining eigenmodes $\hat{s}_j$. φ is the angle between the eigenmode $\hat{s}_k$ and its biorthogonal $\hat{r}_k$. Diagrams are shown for a) φ=0 (orthogonal eigenmodes) with $\nu_k = 1$ b) φ>0 with $\nu_k > 1$ and c) φ close to the limiting case of π/2 with $\nu_k >> 1$.

The next chapter describes the WS 2D zonally averaged model used in this study, and the manner in which the linearised operator is obtained.

Chapter 3

The Wright and Stocker two-dimensional zonally averaged ocean model

3.1 The Wright and Stocker ocean model

The ocean model considered in this study is a 2-D zonally averaged model developed by Wright and Stocker (1991) as a model of reduced complexity for the study of the structure and variability of the large-scale THC. This model, which shall be referred to as the WS model, has been shown to be capable of reproducing the major features of the present-day THC (Stocker and Wright 1991, Wright and Stocker 1991, Wright et al. 1995). Numerous studies have used this model to investigate the mechanisms involved in the variability of the THC, the existence of multiple equilibria, and transitions between these equilibria (e.g. Aeberhardt et al. 2000, Stocker et al. 1992a, b, Schmittner and Stocker 2001, Schmittner and Weaver 2001, Knutti and Stocker 2002).

The WS model has also been shown to be sensitive to changes in internal parameters in a manner similar to OGCMs (Wright and Stocker 1991, Knutti et al. 2000). The sensitivity of the THC to switches between restoring and mixed boundary conditions and the amounts, rates and locations of freshwater input required to trigger a conveyor shutdown have been extensively investigated using the WS model (Stocker and Wright 1991, Wright and Stocker 1991, Stocker et al. 1992a, b, Vellinga 1996) as have the possible impacts of global warming on the atmosphere-ocean system (Schmittner and Stocker 1999, Stocker et al. 1994, Stocker and Wright 1996). Resonant stable centennial scale oscillations about the steady state in a randomly forced WS model were observed

by Schmidt and Mysak (1996). This earlier study focused on the eigenstructure of the linearised dynamics and did not consider transient amplification of THC anomalies.

The state variables of the WS model are temperature and salinity. The model dynamics follow from the Boussinesq equations formulated on a spherical coordinate frame, zonally averaged between the east and west boundaries of the ocean basin of angular width $\Delta\Lambda$. In the following equations, all state variables are zonally averaged.

The prognostic equations are the conservation of energy and salt expressed as advection-diffusion equations:

$$\frac{\partial T}{\partial t}+\frac{1}{c}\frac{\partial}{\partial \phi}\left(\frac{c\upsilon}{a}T\right)+\frac{\partial}{\partial z}(wT)=\frac{1}{c}\frac{\partial}{\partial \phi}\left(\frac{cK_H}{a^2}\frac{\partial T}{\partial \phi}\right)+\frac{\partial}{\partial z}\left(K_V\frac{\partial T}{\partial z}\right) \tag{3.1}$$

$$\frac{\partial S}{\partial t}+\frac{1}{c}\frac{\partial}{\partial \phi}\left(\frac{c\upsilon}{a}S\right)+\frac{\partial}{\partial z}(wS)=\frac{1}{c}\frac{\partial}{\partial \phi}\left(\frac{cK_H}{a^2}\frac{\partial S}{\partial \phi}\right)+\frac{\partial}{\partial z}\left(K_V\frac{\partial S}{\partial z}\right) \tag{3.2}$$

Horizontal momentum balance is represented by geostrophic balance without horizontal or vertical diffusion of momentum:

$$2s\Omega u=-\frac{1}{\rho_* a}\frac{\partial p}{\partial \phi} \tag{3.3}$$

$$-2s\Omega\upsilon=-\frac{1}{\rho_* ac}\frac{\Delta p}{\Delta\Lambda} \tag{3.4}$$

The assumption of balance does not imply that momentum diffusion is unimportant in determining zonally averaged oceanic conditions. In the present formulation momentum diffusion is implicitly taken into consideration by defining a relationship

between the east-west pressure difference and the north-south density gradient as will be discussed below. Vertical momentum balance is represented by hydrostatic equilibrium:

$$\frac{\partial p}{\partial z} = -\rho g \tag{3.5}$$

and mass conservation is represented by the continuity equation:

$$\frac{1}{ac}\frac{\partial}{\partial \phi}(c\upsilon) + \frac{\partial}{\partial z} w = 0 \tag{3.6}$$

A linearised equation of state is used to close the system.

$$\rho = \rho_*\left[1 - \alpha\left(T - T_0\right) + \beta\left(S - S_0\right)\right] \tag{3.7}$$

where $\alpha = 0.223\ K^{-1}$, $\beta = 0.796\ psu^{-1}$ and $\rho_* = 1027 kg/m^3$ is a constant reference density. In the above equations, ϕ is the latitude, $s = \sin\phi, c = \cos\phi$ and z is the vertical coordinate, increasing from $-H$ at the bottom to zero at the surface; u, υ and w are the zonally averaged horizontal and vertical velocity components; T, S, ρ and p denote zonally averaged potential temperature referenced to the surface, salinity, in situ density and pressure; Ω and a are the angular velocity and radius of the Earth, and g is the acceleration due to gravity. The constant horizontal and vertical diffusion coefficients are respectively $K_H = 1.0 \times 10^3 m^2 s^{-1}$ and $K_V = 1.0 \times 10^{-4} m^2 s^{-1}$ for all model runs used to analyze the nonnormal dynamics of the system. Sensitivity of the dynamics to the vertical diffusivity will be discussed at the end of this chapter. For this study the model is a single Boussinesq ocean basin with a uniform depth of 5000m and constant angular width of 60^o in the Northern Hemisphere only, discretized to 20 vertical layers and 20 latitudes.

It is not possible to determine the east-west zonally averaged pressure gradient, $\frac{\Delta p}{\Delta \Lambda}$, from the model equations given above. Wright and Stocker (1991) parameterized this pressure gradient in terms of the north-south density gradient. This parameterization guarantees that $u, v = 0$ at the lateral boundaries and can be approximated by the relation,

$$\frac{\Delta p}{\Delta \Lambda} = -\varepsilon \sin(2\phi)\frac{\partial p}{\partial \phi} \tag{3.8}$$

where ε is a closure parameter that depends on the width of the basin. Wright and Stocker (1991) provide a discussion of the test of the validity of this parameterization. In order to simplify the analysis, a value of $\varepsilon = 0.45$, (as used in Wright and Stocker (1991)), was chosen for this study.

No-flux conditions are specified for T and S at solid boundaries:

$$\frac{\partial T}{\partial s} = \frac{\partial T}{\partial z} = \frac{\partial S}{\partial s} = \frac{\partial S}{\partial z} = 0 \tag{3.9}$$

Furthermore, rigid boundaries are assumed: $\upsilon = 0$ at northern and southern walls and $w = 0$ at the top and bottom of the basin. The vertical flux of heat and salt at the surface are parameterized by

$$-K_V T_z = \frac{H_M}{\Gamma_T}(T - T_*) \tag{3.10}$$

$$-K_V S_z = \frac{H_M}{\Gamma_S}(S - S_*) \tag{3.11}$$

where $H_M = 50m$ is the depth of the surface layer and Γ_T is the relaxation timescale for temperature and Γ_S is the relaxation timescale for salt. Surface temperature and salinity are restored to observed fields of annual mean temperature, T_*, and salinity, S_*, as compiled by Levitus (1982). Plots of S_* and T_* as a function of latitude in the northern hemisphere are shown in Figures 4.1a) and b) respectively. The relaxation times chosen for the model runs used to analyze the nonnormal dynamics in this study are $\Gamma_T = 30$ days and $\Gamma_S = 120$ days (some discussion of sensitivity of the dynamics to these values will follow).

Finally, the meridional overturning stream function Ψ is defined by

$$\upsilon = -\frac{1}{c}\frac{\partial \Psi}{\partial z} \tag{3.12}$$

$$w = -\frac{1}{ac}\frac{\partial \Psi}{\partial \phi} \tag{3.13}$$

with $\Psi = 0$ at the top and bottom of the basin for all latitudes.

The solution procedure for the model dynamics is as follows. The temperature and salinity fields are calculated using forward time-differencing and numerical diffusion associated with the advective terms is reduced using the method described in Wright and Stocker (1991). The density field is determined by the linear equation of state and from this the streamfunction and velocity fields can be calculated as described in Wright and Stocker (1991).

Static instabilities are removed using the convection scheme described in Wright and Stocker (1991). This is an efficient mixing scheme that parameterizes small scale motions

not resolved by the model. Unstable stratification is removed by determining the top and bottom cells of unstable parts of the water column and setting the temperature and salinity to the volume-weighted mean over this region. The effect of convection is to reduce vertical density gradients and mix down any positive density anomalies on very short time scales. For all runs of the full nonlinear model the vertical water columns were swept four times to remove static instabilities.

3.2 Linear theory

In this research the techniques of generalized linear stability theory are used to calculate the linear perturbations that lead to the most rapid growth of THC anomalies. The system of governing equations may be written formally in terms of a nonlinear operator N

$$\frac{dP(t)}{dt} = N(P(t)) \tag{3.14}$$

where $P(t)$ is the state vector of the system consisting of the temperature and salinity at each grid point. If a perturbation P' is added to the steady state solution $\overline{P}$ then the perturbation evolution is described by

$$\frac{dP'}{dt} = \left(\frac{dN}{dP}\right)_{\overline{P}} P' + higher\ order\ terms \approx AP' \tag{3.15}$$

assuming that P' is sufficiently small so that terms of quadratic and higher order in P' are negligible compared to AP'.

The tangent linear operator A which represents the linearised model equations is defined as

$$A = \left(\frac{dN}{dP} \right)_{\bar{P}} \tag{3.16}$$

A time-independent steady state is used to simplify the analysis and dynamical interpretation of the system. In this case the system is autonomous and its eigenmodes evolve exponentially in time. The solution of the tangent linear system is

$$P'(t) = e^{At} P'(t=0) = B(t,0)P'(0) \tag{3.17}$$

where the matrix $B(t,0) = e^{At} \equiv B(t)$ is the propagator of the system since it advances the state vector forward in time and $P'(0) \equiv P_0'$ is the perturbation state vector at t=0.

The linear tangent matrix A is calculated numerically using the full nonlinear model after it has been run to steady state for 12,000 years according to Eq. (3.16). When the prognostic equations for temperature and salinity are perturbed by 0.0001 ^{o}C and 0.0001 ppt respectively each component of the linear tangent matrix is simply the difference between the perturbed value and the steady state value divided by the perturbation magnitude. Huck and Vallis (2001) conclude that the eigenvalues and eigenmodes of the linear tangent matrix obtained in this way are rather insensitive to the amplitude of the perturbations.

Chapter 4

Optimal initial conditions

4.1 Introduction

In this chapter generalized linear stability theory is used to calculate the optimal initial conditions that result in transient amplification of THC anomalies in the WS model. The linear tangent matrix is obtained as described in the last chapter. The system is shown to be stable to perturbations in the asymptotic limit but due to its nonnormality is shown to exhibit large transient growth of THC anomalies. The dominant eigenmodes of the system responsible for the transient amplification process will be identified.

4.2 Results

The full nonlinear model is started from rest with the ocean at a uniform temperature of 4^{o}C and salinity of 35 ppt and run to steady state for 12,000 years under the restoring boundary conditions described in Eq. (3.10) and Eq. (3.11). The steady state salinity field, temperature field and streamfunction reached by the full nonlinear model are shown in Figures 4.1c), 4.1d) and 4.1e) respectively. The streamfunction exhibits a typical overturning circulation with a maximum value of about 10 Sv. This value is smaller than the estimated (15 ± 2) Sv (Ganachaud and Wunsch 2000) but consistent with other results obtained using this model in the absence of wind forcing (Stocker et al. 1994).

The eigenvalues of A are all found to be negative indicating an asymptotically stable system: any initial perturbation to the system will decay to zero after a sufficiently

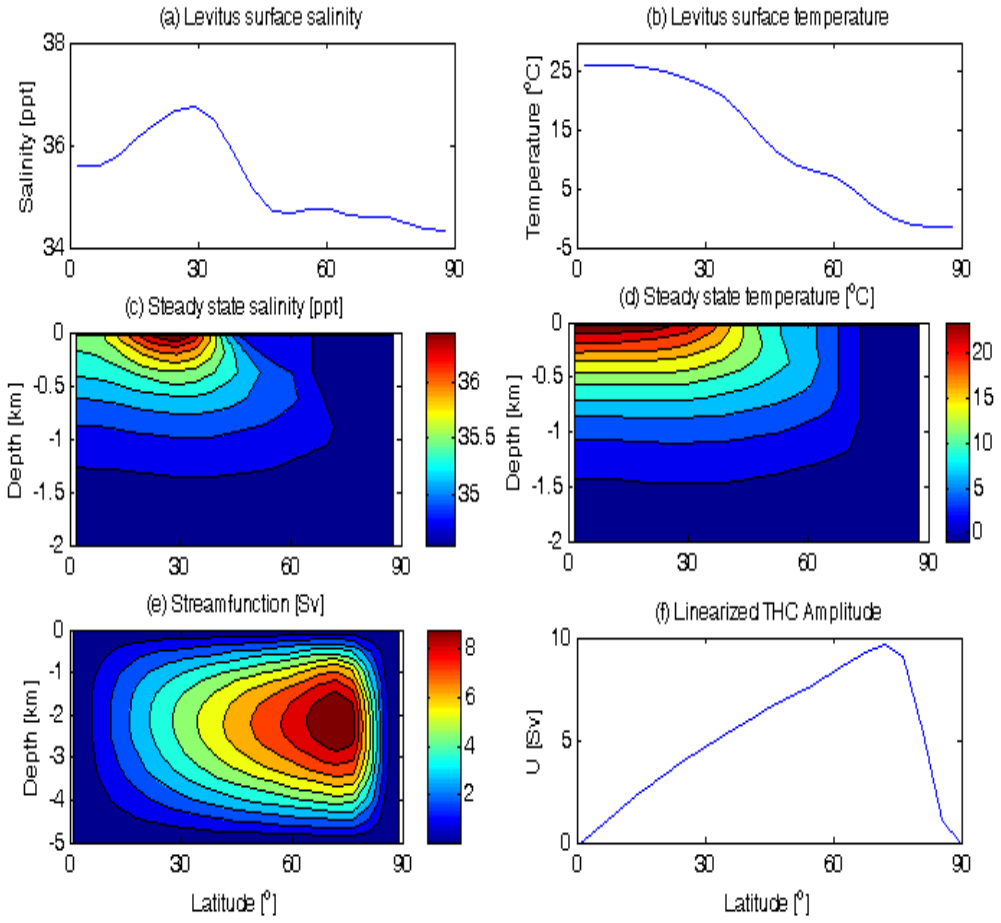

Figure 4.1. Surface forcing fields of (a) salinity and (b) temperature from Levitus (1982), and steady-state fields after 12000 year spinup, (c) salinity, (d) temperature, (e) streamfunction, and (f) linearised THC amplitude.

long time, with an asymptotic decay timescale for each mode given by the reciprocal of the real part of its eigenvalue. Modes with imaginary eigenvalues will oscillate as they decay with timescales of 2π times the reciprocal of the imaginary part of the eigenvalue. Figure 4.2a) shows the decay and oscillatory timescales of the 800 modes of the system. The decay timescales range from days to thousands of years. Of the 800 modes, 552 oscillate as they decay with oscillation timescales ranging from decades to tens of thousands of years. The decay timescale appears to be independent of whether or not the

mode oscillates but the fastest decaying modes do not oscillate. This result is similar to that obtained from Zanna and Tzipermann's (2005) coupled atmosphere-ocean model, in which it was also found that the very fast decaying modes did not oscillate.

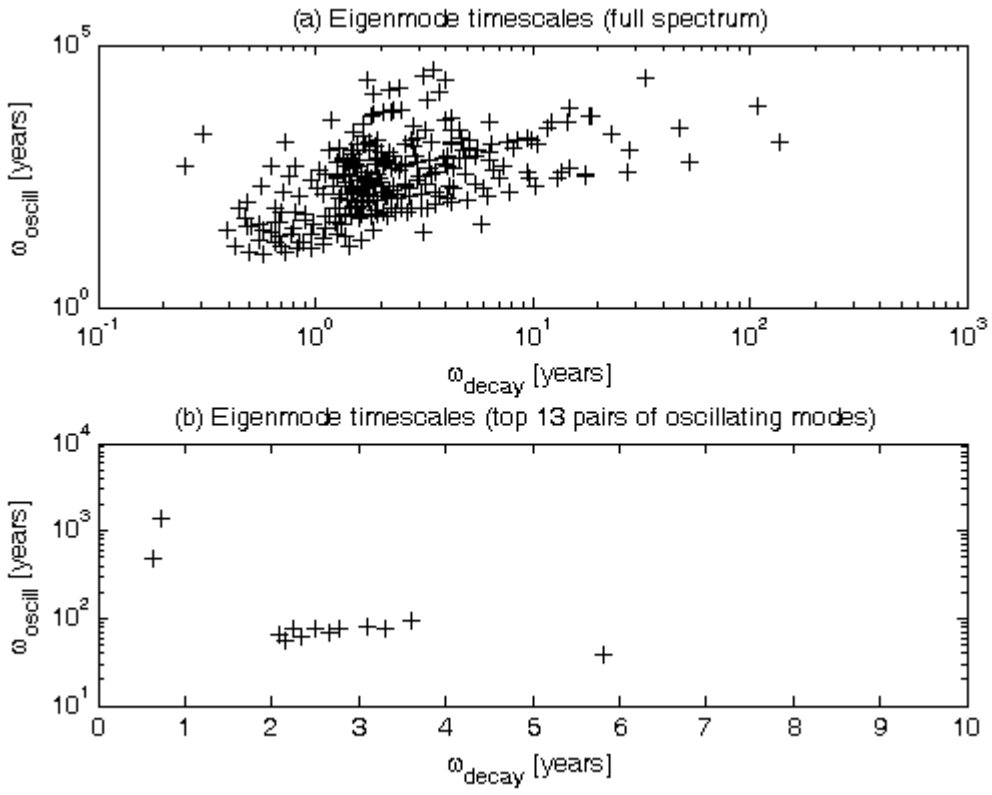

Figure 4.2. (a) Oscillation timescale versus decay timescale for the eigenmodes of the linear tangent matrix A and (b) oscillation timescale versus decay timescale for the top 13 pairs of oscillating eigenmodes responsible for the transient amplification of the THC amplitude. Each eigenmode with a nonzero oscillation timescale has a corresponding complex conjugate whose oscillation timescale is the negative of the original oscillation timescale. Not shown in (b) are the three purely decaying modes that are important contributors to the transient amplification whose decay timescales are 0.65, 0.65 and 0.63 years.

As discussed in Tziperman and Ioannou (2002) a quantity representing the THC amplitude must be defined in order to study the growth of anomalies by the nonnormal

linearised dynamics in the stable regime. This quantity, $U(\phi)$,is analogous to the meridional overturning streamfunction defined in Eq. (3.14) and can be written in terms of the depth averaged meridional velocity, $v(\phi)$

$$U(\phi) = v(\phi)\Delta x H_{top} \tag{4.1}$$

In the above, Δx is the width of the basin and

$$v(\phi) = \frac{1}{H_{top}} \int_{-H_{top}}^{0} v(\phi, z)dz \tag{4.2}$$

where $H_{top} = 2000m$. The meridional velocity is positive in the top 2000 m of the ocean and negative in the bottom 3000m, thus the integration is only over the top portion of the ocean. A plot of $U(\phi)$ as a function of latitude for the steady state solution is shown in Figure 4.1f). The maximum value occurs at about 72^o N which is consistent with the steady state streamfunction reached by the full nonlinear model 12,000 years after spinup (Figure 4.1e).

The quantity to be maximized, $M(t=\tau)$, is the sum over latitudes of the squares of the THC anomaly amplitude,

$$M(t=\tau) = \sum_{\phi=0}^{90^o} \left|U(\phi, t=\tau)\right|^2 \tag{4.3}$$

(from this point onwards, all state variables are perturbation quantities so primes are dropped for notational convenience). Since the THC amplitude is proportional to the meridional velocity, $M(t=\tau)$, is a useful measure of the overall strength of the overturning circulation that is quadratic in the state variables. Evaluating the THC anomaly at the single latitude (72^{o}N) where $U(\phi)$ is a maximum rather than summing

over all latitudes did not yield particularly interesting results: in this case transient amplification and then decay did not occur. Instead, the THC anomaly was initially nonzero and simply decayed over time such that large anomalies occurred only at 72°N rather than over the whole domain. Zanna and Tziperman (2005) also found it dynamically uninteresting to use a norm kernel that maximized the transient growth of the THC at single latitude.

In the linearised dynamics the THC amplitude is directly proportional to the statefunction according to $U(\phi,t) = R_\phi{}^T P(t)$ where R_φ is a linear operator relating temperature and salinity perturbations to overturning strength perturbation, corresponding to a discretized approximation to Eq (4.1). The norm used to measure the growth of the state vector anomaly at time τ, $P(\tau)$, follows from Eq (4.3) with $M(\tau) = P^T(\tau) X P(\tau)$ where the norm kernel matrix X is

$$X = \sum_{\phi=0}^{90^o} (R_\phi R_\phi^T) \tag{4.4}$$

Because temperature and salinity perturbations can counteract each other so as to have no net effect on the strength of the overturning, Eq. (4.4) results in a singular matrix (i.e. its determinant is zero) that in turn may result in infinite amplification factors over finite time. For a transient growth analysis done for the THC in Griffies and Tziperman's (1995) 4 box model the singular norm kernel defined in Eq. (4.4) leads to 2 of the 8 eigenmodes having infinite amplification. To eliminate this possibility Tziperman and Ioannou (2002) regularize the norm kernel by adding a small diagonal matrix to X to create a nonsingular matrix. In this study a matrix with diagonals less than 0.005 percent

of the maximum element of X was added to X resulting in a matrix with small but nonzero determinant.

The timescale for optimal growth, τ_{opt}, is the value of τ maximizing the amplification factor λ given in Eq. (2.2); a plot of λ as a function of τ is given in Figure 4.3. Following the same logic as Sevellec et al. (2007), the first peak that occurs at τ=0.4 years is disregarded because this timescale is too small to be relevant in the WS 2D model. The second maximum where τ_{opt}=6 years was the timescale used in the propagator matrix for all subsequent calculations. It should be noted here that for nonnormal systems amplification processes are the result of the combination of two effects: one that is nonnormal with a timescale representing transient growth and one that is normal with a timescale governed by the least damped eigenmode characterising the asymptotic decay of the perturbation (Trefethen 1997). Thus the timescales of the individual eigenmodes of the system are not necessarily the same as the timescale of the transient amplification of perturbations.

The optimal initial salinity and temperature perturbations calculated from the linearised model equations that maximize the transient amplification of the THC anomaly for τ = 6 years are shown in Figures 4.4a) and 4.4b). The evolution of these anomalies is shown in Figures 4.4c) to 4.4h). The temperature and salinity optimal initial conditions have a dipole structure between 70^{o}N and 80^{o}N with negative temperature and positive salinity anomalies on the surface and with anomalies of opposite sign at depth. At t=6 years (Figures 4.4e) and 4.4f)), the time of maximum amplification, the sign of the

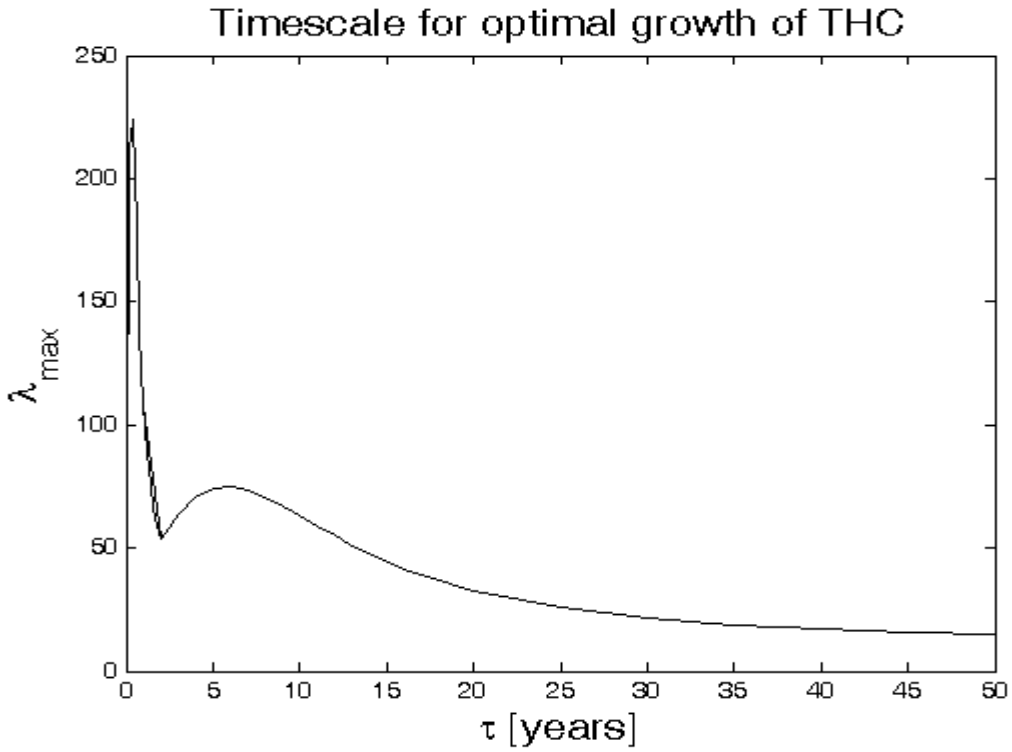

Figure 4.3. Maximum amplification factor (Eq. 2.2) of the linearised model as a function of time.

anomalies in the dipole have reversed for the temperature but not for the salinity. In both cases the anomalies spread out over an even wider range of space. This significant redistribution of temperature and salinity anomalies in space as they amplify rather than a localized growth implies that both advection and non localized effects contribute to the transient growth. The slow decay of the temperature and salinity anomalies is governed by horizontal and vertical diffusion.

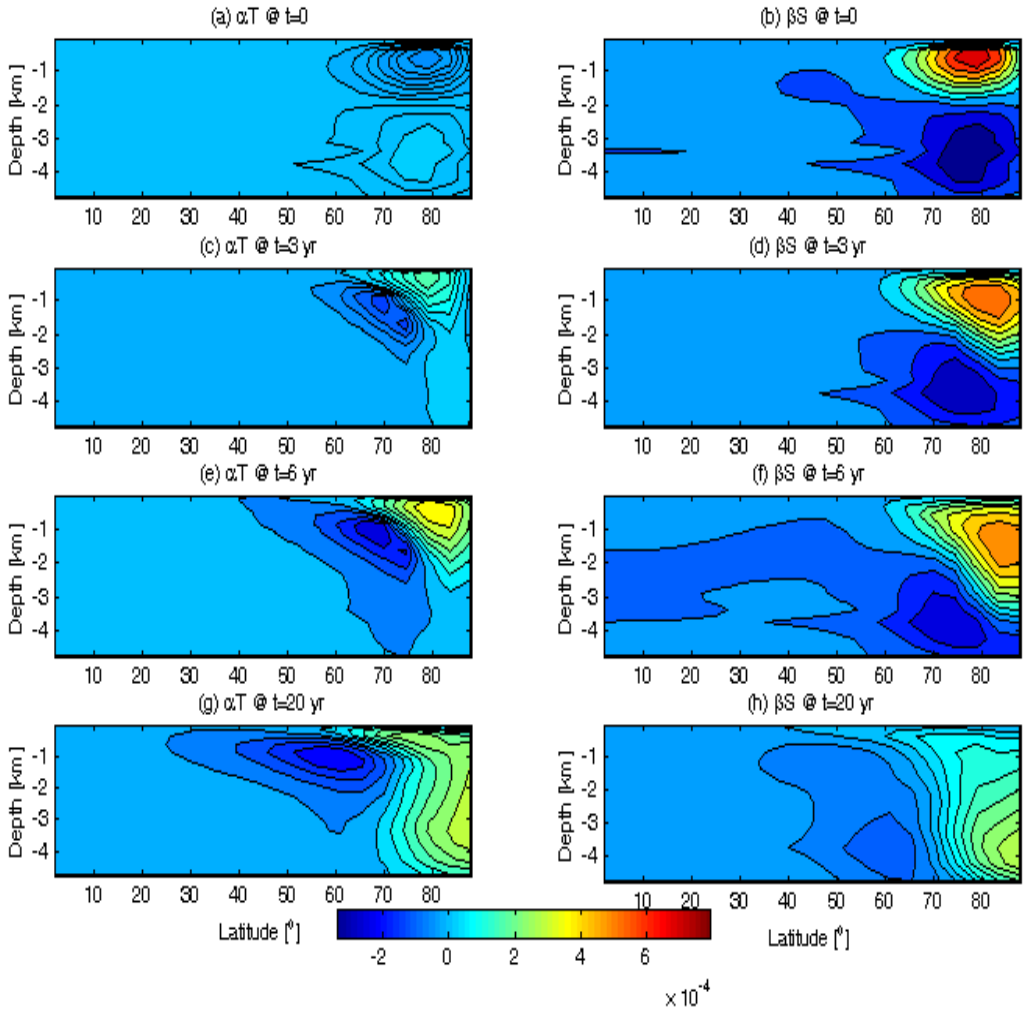

Figure 4.4. (a) Optimal initial temperature perturbation (αT) and (b) optimal initial salinity perturbation (βS) calculated from the linearised model equations that maximize the transient amplification of the THC for τ = 6 years. (c) to (h) αT and βS perturbations at 3 yr, 6 yr and 20 yrs.

The evolution of the THC anomaly, $U(\phi,t) = R_{\phi}^{T} P(t)$, and the contributions to the THC anomaly from the salinity and thermally driven components are displayed as a function of latitude in Figures 4.5a) through 4.5f). Initially the salinity and thermally driven components tend to cancel each other so that the THC anomaly is nearly zero at t=0 (Figure 4.5a). This is consistent with previous studies of THC transient amplification

using both box models (Zanna and Tziiperman, 2007, Tziperman and Iaonnou, 2002) and GCMs (Tziperman et al. 2008). The different evolutions of the temperature and salinity anomalies lead to growth at later times with the salinity contribution dominating the overall amplification of the THC. The maximum growth of the THC occurs at 76.5^{o}N at t=6 years (Figure 4.5d). Throughout most of the evolution of the perturbation, anomalies in each of the temperature and salinity contributions to the THC are of opposite signs and are concentrated in the middle and high latitudes. After 50 years the salinity and temperature components once again exactly cancel one another and the THC amplitude falls to zero (Figures 4.5f). Note that strong anomalies in both temperature and salinity persist for many decades after the anomaly in overturning strength has decayed.

Figures 4.6a) through 4.6d) show the time evolution of the linear THC amplitude and the contributing salinity and temperature components for latitudes 18^{o}N, 36^{o}N, 54^{o}N and 76.5^{o}N respectively. In these plots it can be seen again that the contributions from both the salinity and thermally driven components are significant with the salinity dominating at 76.5^{o}N where the growth of the THC is a maximum (Figure 4.6d). At the lower latitudes the salinity component initially dominates the growth but after the first 6 years when the maximum amplification has been reached and the anomalies begin to decay the thermally driven component dominates the decay. The decay times for the components is longer at low latitudes than it is at the high latitudes (Figures 4.6 a, b & c). Note that at some latitudes the intensification of the overturning strength locally is preceded by a slight weakening.

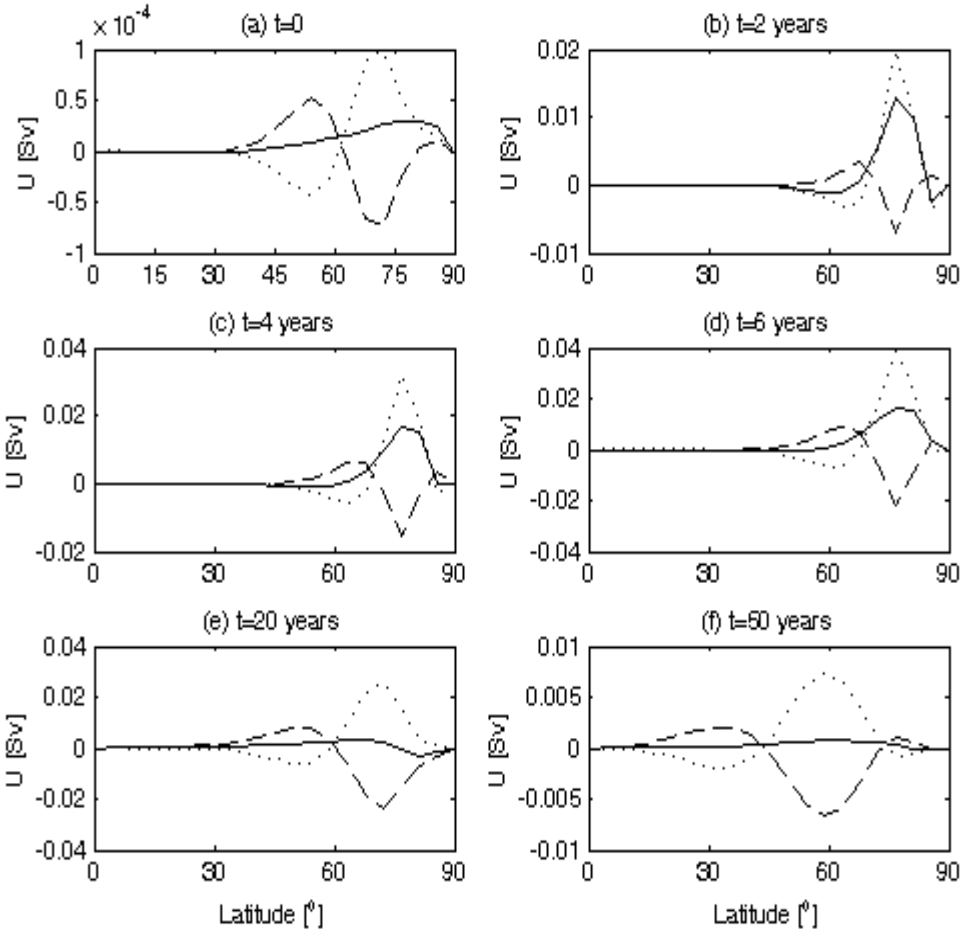

Figure 4.5. Evolution of the linear THC anomaly (solid line) and its contributions from the temperature (dashed line) and salinity (dotted line) as a function of latitude calculated from the linearised model equations starting from the optimal initial conditions that maximize the transient amplification of the THC anomaly for τ = 6 years. (a) t=0, (b) t=2 years, (c) t=4 years, (d) t=6 years, (e) t=20 years and (f) t=50 years. (Note that the scaling for each plot is different and the maximum amplification occurs at t=6 years).

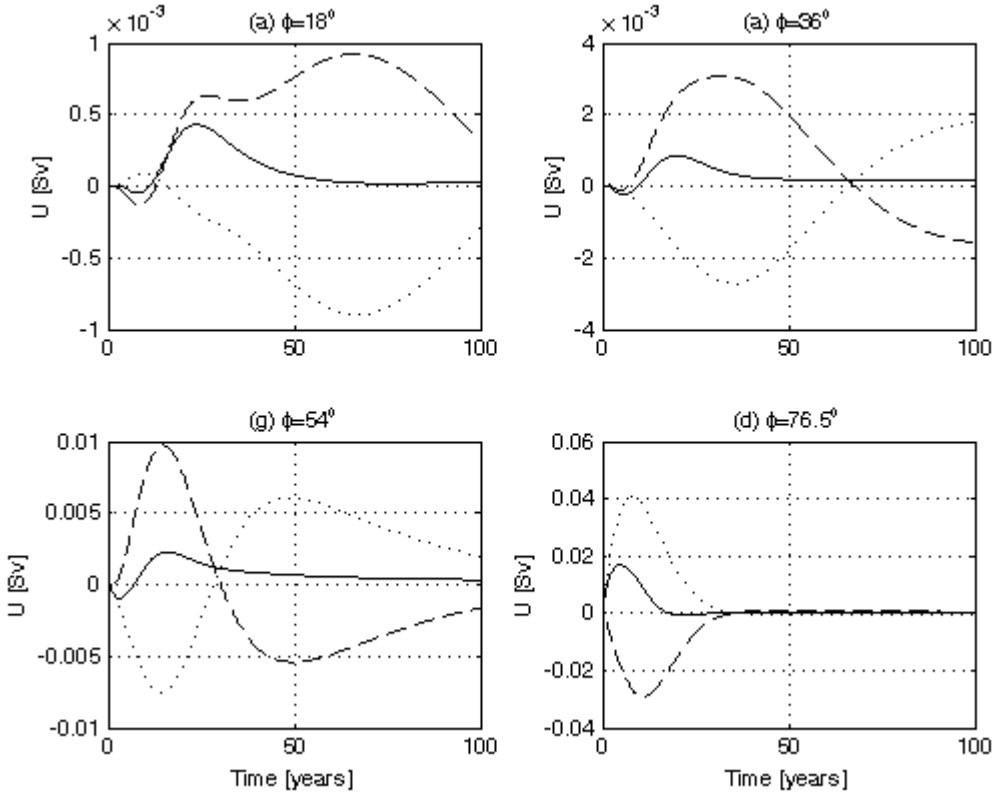

Figure 4.6. Evolution of the linear THC anomaly (solid line) and its contributions from the temperature (dashed line) and salinity (dotted line) as a function of time calculated from the linearised model equations starting from the optimal initial conditions that maximize the transient amplification of the THC anomaly for τ = 6 years. (a)φ=18^o, (b) φ=36^o, (c) φ=54^o and (d) φ=76.5^o.(Note that the scaling of each plot is different and the maximum amplification occurs at 76.5^o).

The THC salinity and temperature components as a function of time and latitude are shown in Figure 4.7a) and 4.7b). Since the contributions from the salinity and temperature components are of opposite sign the negative of the temperature contribution is plotted enabling an easier comparison of their magnitudes and timescales. It can be seen that the salinity contribution reaches a larger maximum value than the temperature contribution while the spatial structures are very similar. The dominance of the salinity

contribution to the total THC can be seen by noting that the sign of the total THC amplitude is the same as the sign of the salinity component (compare Figure 4.8b to 4.7a).The growth of the salinity and thermally driven components of the THC tends to occur for longer periods of time than the growth of the total THC (Figure 4.8b), because the two contributing components tend to cancel each other after about 50 years.

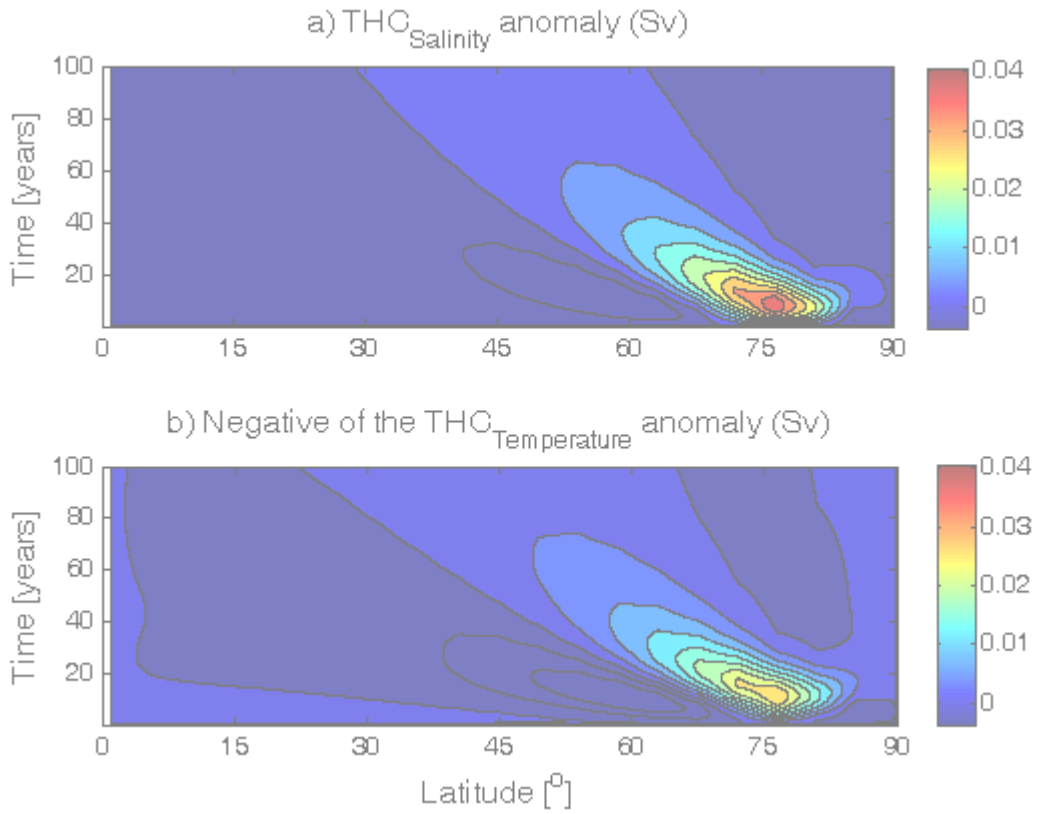

Figure 4.7. a) Evolution of the salinity component of the THC amplitude and b) evolution of the negative of the temperature component of the THC amplitude both as a function of time and latitude calculated from the linearised model equations starting from the optimal initial conditions that maximize the transient amplification of the THC anomaly for τ=6 years

For the above analyses it has been assumed that the evolution of the THC anomaly is governed by linear dynamics. It is therefore important to compare the evolution of the

THC anomaly amplitude, $U(\phi)$, calculated using the full nonlinear model to that calculated using the linear model. This was done by adding the optimal initial conditions state vector (of small norm) to the steady state solution of the Stocker and Wright model and then running the full nonlinear model for a further 200 years. The THC anomaly amplitude calculated from the nonlinear model exhibits a similar transient growth pattern as that of the linear model (Figure 4.8a). The differences are small enough that it may be concluded that the linear approximation is valid for sufficiently small perturbations.

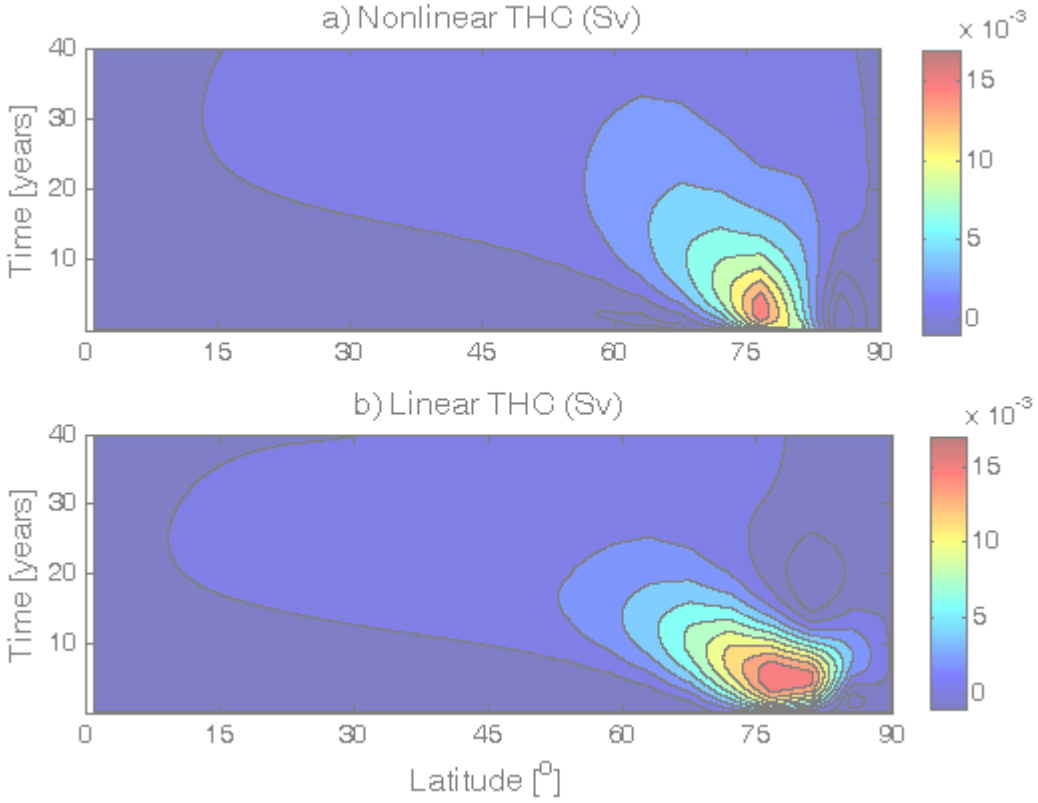

Figure 4.8. (a) THC anomaly calculated from the full nonlinear model and (b) THC anomaly calculated from the linearised model equations starting from the optimal initial conditions that maximize the transient amplification of the THC anomaly for τ=6 years

Even though all of the eigenmodes of the linear operator A are stable, the nonnormality of A results in nonorthogonal, linearly dependent eigenmodes. Transient perturbation growth results from the linear interference of nonorthogonal eigenmodes with different decay times. The timescale of the transient amplification is typically the same as the timescale of the fastest decaying relevant eigenmode (Farrell and Ioannou, 1996). The decay of the perturbations is then governed by the slowest decaying relevant eigenmode. The amount of perturbation growth possible is proportional to the degree of linear dependence of the eigenmodes (Aiken et al. 2002). To investigate the "optimal" eigenmodes of the linear operator which participate in the observed perturbation growth the optimal initial conditions P_0 are projected onto the eigenmodes of A as described in Chapter 2.

The state vector P_0 can be written as a linear superposition of the eigenmodes:

$$P_0 = \sum_{k=1}^{k=800} a_k \hat{s}_k \tag{4.5}$$

where a_k is given in Eq. (2.6).

To determine which eigenmodes are responsible for the transient amplification of the THC the projection coefficients for each eigenvector of the generalized eigenvalue problem $B(\tau)^T XB(\tau)P = \lambda XP$ are calculated using Eq. (2.6). Each of these 800 eigenvectors has a corresponding a_i series of 800 values corresponding to the 800 eigenmodes of the system. These sets of projection coefficients are plotted in Figure 4.9a). The eigenmodes denoted by k are arranged according to increasing modulus of the eigenvalues of A. The eigenmodes that consistently have large projection coefficients are

the ones that are favored by the optimal vectors. It can be seen in Figure 4.9b) that 5 modes have consistently large projection coefficients. Two are oscillating complex conjugate pairs, (641,642) with decay and oscillation timescales of 0.72 years and 1420 years respectively and (667,668) with decay and oscillation timescales of 0.63 years and 478 years respectively. The other three favored eigenmodes are purely decaying ones (658,659 & 666) with decay times of 0.65 years, 0.65 years and 0.63 years respectively.

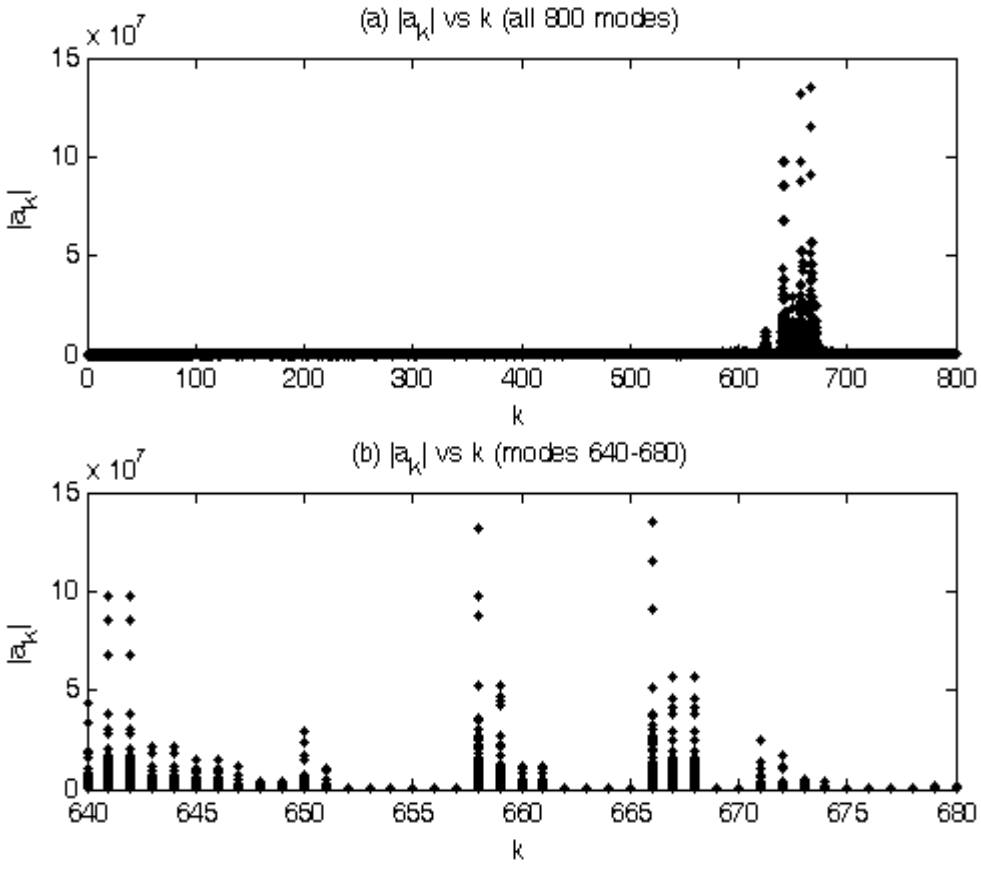

Figure 4.9. (a) Projection coefficients computed by projecting each eigenvector of (Eq.2.5) onto the full set of 800 eigenmodes of A (k=1,..,800). The amplitude coefficients for all 800 eigenvectors are shown for each k and (b) projection coefficients for eigenmodes k=640,..,680

The contribution of an eigenvector to the nonnormality of A can be quantified by the factor $\nu(k) = |\hat{s}_k \| \hat{r}_k | / (\hat{r}_k{}^T \hat{s}_k)$ as discussed in Chapter 2. A plot of $|\nu(k)|$ vs $|a(k)|$ for the optimal initial condition, P_0 is shown in Figure 4.10a). The five eigenmodes (circled in blue) that have consistently large projection coefficients at t=0 are also the most highly nonnormal eigenvectors. However, these five eigenmodes alone are not sufficient for producing transient amplification of THC anomalies. Although the degree of nonnormality does not change as the system evolves in time the projection coefficients do change as the state vector $P(t)$ evolves. To gain further insight into the eigenmodes that are responsible for the transient amplification of THC anomalies on a timescale of 6 years the statevector at t=6 years was projected onto the eigenmodes of A. Figure 4.10b) shows a plot of $|\nu(k)|$ vs $|a(k)|$ at t=6years. It can be seen that the 5 highly nonnormal modes (circled in blue) no longer have large projection coefficients at t=6 years indicating that their contribution to the transient amplification is only important close to t=0. This is consistent with nonnormal operators whose transient behavior differs entirely from the asymptotic behavior suggested by the eigenvalues. The eigenmodes that contribute most to the maximum amplification of the THC anomalies at t=6 years are the ones with large projection coefficients in Figure 4.10b) (circled in red in both Figures 4.10 a) and b)). Eleven pairs of oscillating eigenmodes with decay timescales ranging from 2 to 6 years and oscillation timescales ranging from 35 to 95 years were found to be the most significant contributors to the amplification process. The decay and oscillation timescales of these 11 pairs of modes as well as the 2 oscillating highly nonnormal modes are shown in Figure 4.2b). The eigenmodes with relatively large projection coefficients

that are not circled in Figure 4.10b) all have decay timescales less than 2 years. When these modes were added to the initial perturbation the amplification shown in Figure 4.11 did not change significantly; these modes do not appear to play an important role in the transient amplification process.

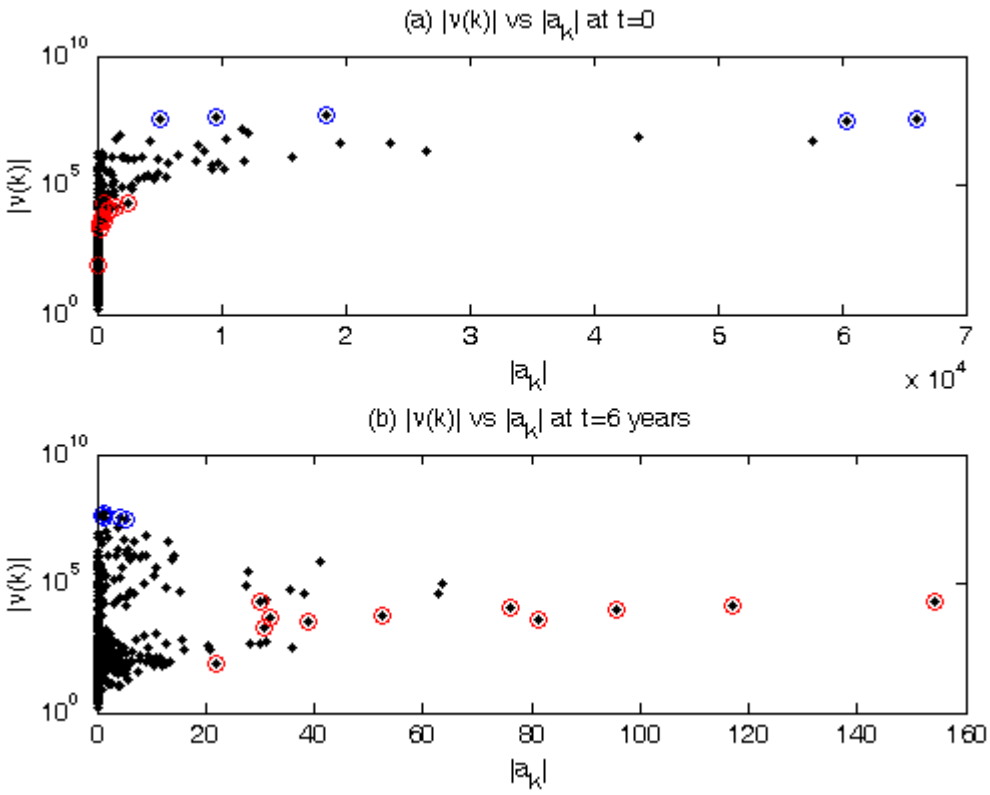

Figure 4.10. (a) $|v(k)|$ vs $|a_k|$ for k=1,..,800 for P_0, the optimal initial conditions and (b) $|v(k)|$ vs $|a_k|$ for k=1,..,800 for P_6, the state vector at t=6 years. The 13 pairs of oscillating modes and 3 nonoscillating modes responsible for the transient amplification are circled in (a) and (b).

Combining the 5 highly nonnormal eigenmodes that are important to the amplification process during the initial few years with the 11 oscillating pairs of modes that are important at the time of maximum amplification leads to a fairly good

representation of the transient amplification of the THC. Figure 4.11 shows the evolution of the linear THC anomaly produced by these 13 pairs of oscillating eigenmodes and three nonoscillating eigenmodes and by the full set of 800 eigenmodes (note that the amplification is in fact greater for the full system than for the low-dimensional projection because the initial perturbation is much smaller). The evolution of a typical optimal perturbation in a nonnormal system is determined by the evolution of the interference pattern of the relevant eigenmodes rather than by the growth or decay of individual eigenfunctions. The fact that the important eigenmodes that have been shown to be responsible for the transient amplification of THC anomalies in this study have very small decay timescales (less than 10 years) is evidence of the importance of more than just the eigenstructure of the linearised dynamics when considering the response of this system to perturbations.

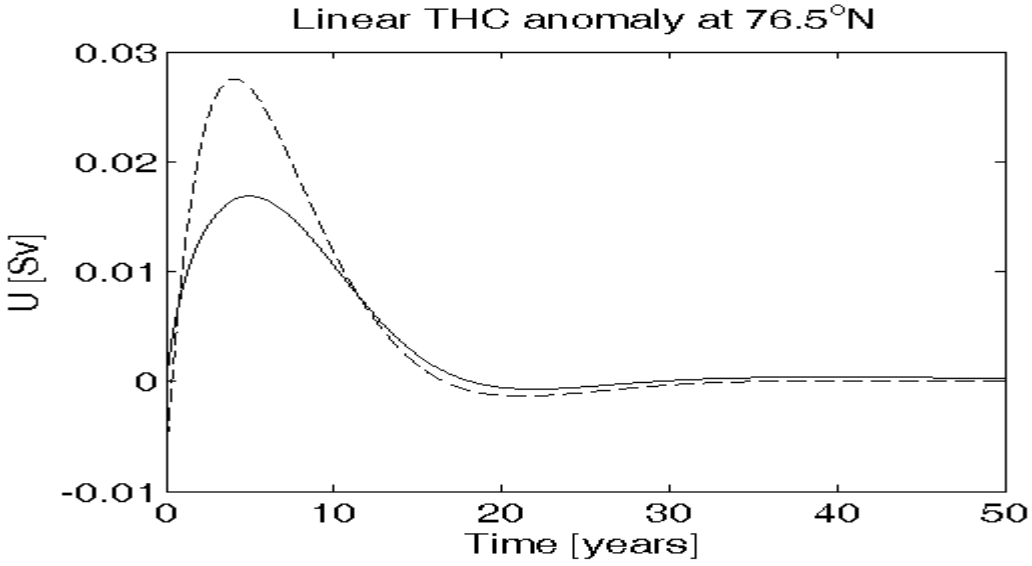

Figure 4.11. Evolution of the linear THC anomaly from all 800 eigenmodes (solid line) and from the top 13 pairs of oscillating eigenmodes and three nonoscillating eigenmodes.(dotted line).

4.3 Discussion

The overturning strength in the WS model is strongly affected by the strength of the vertical diffusivity K_v (Wright and Stocker 1992), a quantity that is not well constrained by observations. To investigate the role that vertical diffusivity plays in the nonnormal dynamics of transient THC amplification the analysis was repeated for a range of vertical diffusivities (see Table 4.1). It was found that by increasing the vertical diffusivity from $K_V = 0.2 \times 10^{-4} m^2 s^{-1}$ to $K_V = 1.0 \times 10^{-4} m^2 s^{-1}$ in the absence of wind forcing the value of the maximum streamfunction increased from 4.3 Sv to 9.7 Sv. Wright and Stocker (1992) obtained a similar result in the absence of wind forcing. Although the strength of the streamfunction from the Stocker and Wright model used in this study has been shown to be sensitive to variations in K_V our analyses show that the nonnormal dynamics that lead to transient amplification of the THC is not highly sensitive to variations in K_V.

Vertical Diffusivity (m^2s^{-1})	Salinity Relaxation Time (days)	Temperature Relaxation Time (days)	Maximum Stream-function (Sv)	Optimization Time (years)	Maximum Amplification
0.2×10^{-4}	50	50	4	25	55
0.2×10^{-4}	120	30	4	19	22
0.4×10^{-4}	120	30	6	11	43
0.6×10^{-4}	120	30	7	8	60
0.8×10^{-4}	120	30	8	7	69
1.0×10^{-4}	120	30	10	6	75

Table 4.1. The maximum value of the streamfunction, timescale for optimum growth and maximum amplification of the THC anomaly for different vertical diffusivities and relaxation times for the surface salinity and temperature.

The optimal initial conditions over the range of vertical diffusivities used here do not differ significantly in either strength or spatial pattern while the value of the maximum amplification of the THC anomaly from Eq. (4.5) increases from 22 to 75. Furthermore, the general patterns of growth and decay of the two contributions to the THC anomaly amplitude are not affected by changing the vertical diffusivity. Both the dominance of the salinity component in the THC anomaly growth and the latitude of maximum growth are also independent of vertical diffusivity.

The quantity that does depend strongly on vertical diffusivity in the nonnormal analysis of the THC growth is the time of maximum amplification. It was found that increasing K_v by a factor of five (while keeping all other variables constant) decreased the optimization time by about a factor of three (almost the same factor as for amplification). Note that increasing K_v increases the mean overturning strength, so a reduction in the amplification timescale is consistent with an increase in the rate of anomaly advection (although this does not account entirely for the reduction in the amplification timescale).

The optimization time was also found to be dependent on the relaxation timescales of the temperature and salinity boundary conditions. Changing the relaxation timescales from 50 days for each of the temperature and salinity to 30 days for the temperature timescale and 120 days for the salinity timescale (while keeping the vertical diffusivity fixed at $K_V = 0.2 \times 10^{-4} m^2 s^{-1}$) resulted in the optimization time changing from 25 years to 19 years. Once again, the mechanism of transient amplification of the THC was not affected by this change even though the value of the maximum amplification decreased from 55 to 22.

In general 2D zonally averaged models are not expected to permit the investigation of ocean processes characterised by time scales less than a decade and by horizontal spatial scales less then several hundred to thousand kilometers. The two main processes that drive the meridional overturning circulation are the traditional thermohaline mechanism that results in mixing of heat from the surface to the deepwater and the wind-driven upwelling caused by the strong westerly circumpolar winds in the Southern Ocean. The timescales associated with these processes are much longer than a decade but these processes do not fully determine the Atlantic meridional overturning circulation's spatial extent and strength (Kuhlbrodt et al. 2007). Horizontal gyre circulation, atmospheric cooling, precipitation, evaporation and ice melting are some of the variety of processes that can affect the strength and spatial pattern of the meridional overturning circulation. The timescales for these localized processes are usually less than a decade. Even when a model does not explicitly resolve these processes studies have shown that ocean processes characterised by time scales less than a decade can be investigated using 2D zonally averaged models.

Hirschi and Stocker (2002) found that a 3D ocean general circulation model and the WS 2D zonally averaged ocean model produced similar patterns and timescales of propagation of density anomalies. They applied freshwater perturbations at 47.5^{o}S for 2 months and studied the propagation of the resulting density anomalies. The 3D ocean model showed a sharp density signal that propagated as an internal oceanic Kelvin wave reaching the mid latitudes of the northern hemisphere within 2 years. In the zonally averaged model the density signal reached the mid latitudes of the northern hemisphere after about 5 – 10 years. Although the 2D model responded more slowly to the

perturbation than did the 3D model this study showed that the density anomalies in the zonally averaged model propagated faster than color tracers being carried by advection/diffusion. This study also found that the time tendency of the maximum northern meridional overturning cell reached a maximum value after 7-8 years in the 2D zonally averaged model indicating that sub-decadal processes can be captured in such a model. Other studies using the WS 2D zonally averaged model have also investigated processes with timescales less than a decade. Schmittner and Stocker (2001) found that the WS model was able to simulate a global overturning that exhibited a strong seasonal cycle in agreement with 3D ocean models. They found that rapid changes in the maximum streamfunction in the Atlantic occurred on a seasonal timescale when fast freshwater flux perturbations were applied to the model.

In this study the quantity of interest is the transient amplification of the THC due to the nonnormal nature of the tangent linear operator. Since it was found that this mechanism is not strongly dependent on the values of vertical diffusivity or relaxation timescales of the surface temperature and salinity fields the region of parameter space chosen for this study gives the most realistic value for the maximum streamfunction, 10Sv, in the absence of wind forcing ($K_V = 1.0 \times 10^{-4} m^2 s^{-1}$, $\Gamma_T = 30$ days and $\Gamma_S = 120$ days). Although this gives a timescale for amplification that is only 6 years, this value agrees with the timescales for growth found in two other similar studies of nonnormal transient amplification of the THC. Using a coupled ocean-atmosphere GCM Tziperman et al. (2008) found the amplification timescale to be between 5 and 10 years while Zanna and Tziperman (2008 in press) calculated the timescale for maximum amplification of the THC to be 9 years in their 2D zonally averaged coupled ocean-atmosphere box model.

Another supporting result from the GCM study was that the growth of temperature and salinity anomalies occurred largely in the meridional direction indicating that the 2D model may be adequate for capturing the complex linearised dynamics of nonnormal THC perturbation growth.

Although the present study is the first to consider optimal perturbation growth of the THC involving both temperature and salinity fields using the WS model, previous studies have considered transient growth. The first study to apply the ideas of nonnormal dynamics to the THC was that of Lohmann and Schneider (1999), in which the nonnormal properties of the Stommel 2 box model of the THC were considered. They found that the optimal perturbation affecting long-term climate variability had little resemblance to the most unstable mode of the system. Their results suggested that climatic states which were associated with North Atlantic deep water (NADW) formation were located in a specific part of the phase space only where the NADW circulation with a large meridional salinity or small temperature gradient was not stable. This was supported by Tziperman (1997) who found inherently unstable climate behavior due to a weak THC. In agreement with the results of Lohmann & Schneider (1999), the present study finds that nonnormal dynamics lead to perturbations involving both temperature and salinity which display pronounced transient growth. The amplification timescale found in Lohmann and Schneider (1999) was shorter than that found in the present study, but detailed quantitative agreement cannot be expected because of the highly idealized nature of the model used in the earlier study.

Tziperman and Ioannou (2002) presented a detailed analysis of nonnormal dynamics of the THC using a 3 box model, for which two physical mechanisms for the transient

amplification of the THC were identified. One, with a transient amplification time scale of approximately two years, involved an interaction between the THC anomaly induced by rapidly decaying sea surface temperature anomalies and the THC anomaly induced by the slower decaying salinity modes. The second mechanism of transient amplification was primarily driven by an interaction between different slowly decaying salinity modes, and had a typical growth time scale of a few decades. For both mechanisms, the initial THC anomaly was zero because of the offsetting effects of temperature and salinity anomalies on the meridional density gradient. This earlier study agrees with the present study in finding substantial transient amplification on decadal timescales involving both temperature and salinity that is dominated by salinity dynamics.

Transient amplification of the THC in a less idealized model was studied by Zanna and Tziperman (2005), who employed a two dimensional coupled box atmosphere-ocean model to investigate possible physical mechanisms for the transient growth of THC anomalies. Their study found transient growth displaying maximum amplification after 42 years with optimal perturbations involving both temperature and salinity anomalies. This more recent study found that the amplification mechanism was the result of an interaction between a few damped (oscillatory and nonoscillatory) modes with decay times between 20 and 800 years. In agreement with this earlier study, the present study finds the optimal perturbation leading to the greatest transient growth involves interactions between temperature and salinity anomalies which combine in the initial conditions to produce a negligible initial THC perturbation. The present study finds the amplification mechanism is the result of an interaction between 5 highly damped and 11

oscillatory eigenmodes and their complex conjugates with oscillation times between 35 and 95 years. Both the previous study and the present study find that it is impossible to produce an initial THC perturbation of zero when using only the small subset of all dynamical modes that dominate the transient growth of the THC. All of the eigenmodes of the system are required to produce an initial perturbation of zero.

In a recent study, Sevellec et al. (2007) use a 2-D latitude-depth ocean thermohaline circulation model to study the variability of the ocean circulation perturbed by a freshwater flux and also find that the nonnormality of the dynamics leads to transient growth of the overturning circulation intensity. However, in the study of Sevellec et al. (2007), only surface salinity optimal perturbations are used to excite the THC: the temperature component is not included. This study finds that the maximum response of the circulation intensity occurred after 67 years, associated with a single weakly damped linear eigenmode with an oscillation timescale of 150 years. In the present study, with both active temperature and salinity contributions to the density of seawater, the timescales of optimal THC amplification and decay are considerably shorter. Perturbations in temperature and salinity persist for many decades, but in such a way that they counterbalance to produce little effect on the overturning strength after about 50 years. Sevellec et al. (2007) also obtain very different results from truncating the contributions from the eigenmodes of the linear operator, concluding that only a couple of eigenmodes and their biorthogonals determine the effect of initial perturbations on long timescales and that the finite growth for the overturning intensity is due to a single oscillatory mode. This study also finds that the finite growth is dominated by a small number of eigenmodes. The initial cancellation of the salinity and temperature

contributions to the THC anomaly is governed by the most highly nonnormal eigenmodes and the subsequent evolution of this cancellation is governed by 11 pairs of oscillating eigenmodes.

Using the GFDL coupled atmosphere-ocean general circulation model CM2.1, Tziperman et al. (2008) investigated the transient amplification of temperature, salinity and THC anomalies due to nonnormal dynamics; they found that there was significant growth of all anomalies with a typical growth time of 5 to 10 years with the THC anomaly displaying its maximum value at t=6 years. Many sensitivity studies were done to test the robustness of this timescale and it was found that while the timescale was robust to parameter changes in their linearised model the actual value of the amplification was not. The main conclusion drawn from this inverse modeling study was that the nonnormality of the THC dynamics cannot be ignored when estimating reliable predictability limits. The structure of the initial condition of the ocean-atmosphere state will influence the amplification of the THC after a length of time smaller than the expected decadal or centennial variability timescale of the THC.

Generalized stability theory has been shown to be a useful tool for the analysis of transient amplification of THC anomalies. The amplification timescale appears to be a parameter that is sensitive to the model formulation. When salinity and temperature dynamics are both active, the dynamics tend to involve an initial near cancellation of anomalies and the long term evolution is dominated by salinity dynamics.

4.4 Conclusions

Characterizing the variability of the thermohaline circulation is important for understanding internal variability in the Earth's climate system and for detecting trends of anthropogenic origin. In this chapter the ideas of generalized linear stability theory have been applied to the dynamics of the thermohaline circulation described by a 2-D zonally averaged ocean model. As a result of nonnormality of the linearised dynamics, nonorthogonal eigenmodes with different decay times interfere to create transient growth of THC anomalies in an asymptotically stable system. The optimal initial conditions that lead to this transient growth were examined using the tangent linear equation linearised about the steady state, and it was found that the maximum amplification of the THC anomaly occurs after about 6 years.

The major conclusions to be drawn from this chapter are:

- It is possible to obtain significant transient amplification of the THC.
- The amplification process involves temperature and salinity anomalies which combine to create a THC anomaly that is initially close to zero.
- The transient growth of the THC is dominated by the salinity dynamics.
- Large temperature and salinity anomalies persist for a long time after the overturning strength anomaly has decayed.
- Many latitudes show an initial decrease in THC strength before the intensification occurs.
- It is possible to identify a small subset of the dynamics which are responsible for the amplification process. The most nonnormal modes account for the cancellation of the salinity and temperature components of the THC anomalies at t=0.

- The mechanism of amplification is insensitive to model parameters, while the timing of the amplification is sensitive.

The dynamics considered in this chapter were of pure thermohaline circulation, as wind forcing was not accounted for. In reality, the meridional overturning circulation is strongly affected by surface wind forcing; Chapter 6 will consider optimal perturbation growth in the presence of surface winds. The following chapter will consider the stochastically forced WS model.

Chapter 5

Stochastic optimals

5.1 Introduction

This part of the study will provide insight into how the optimal perturbations are relevant to the response to fluctuation surface forcing and the role they play in the variability of the THC. The initial perturbation resulting in optimal transient amplification of the overturning circulation identified in Chapter 4 is dominated by high-latitude surface anomalies of salinity and temperature, but also involves anomalies at depth. Fluctuations in surface forcing can be expected to project on these optimal perturbations, but not perfectly. The relevance of these optimal perturbations to forced variability of the THC is characterised by the strength of the projection of the stochastic optimals (the spatial structures of the noise that result in maximum variance of the THC) on the optimal perturbations, the analysis of which is the focus of this chapter.

Modeling studies suggest that the variability of the THC on decadal-centennial timescales may be strongly influenced by fluctuations in surface forcing on much shorter timescales. Stochastic forcing has traditionally been used to represent such high frequency surface forcing. Hasselmann (1976) first proposed the concept of stochastic climate models as a method to study the influences of short-term atmospheric variability on long-term oceanic variability. The ocean acts as an integrator of the short-term atmospheric fluctuations by transforming the essentially white noise atmospheric forcing into a red response ocean signal. If the climate system has no internal mode of variability then the response to stochastic atmospheric forcing is a red spectrum (with energy

concentrated at the low frequency end of the spectrum). However, if the climate system has preferred modes of variability then stochastic forcing results in peaks in the response spectrum at the characteristic timescales of that variability. In general, there are two potential mechanisms of oscillatory variability of the THC: self-sustained THC oscillations due to internal nonlinearities in the climate system, or oscillations driven by stochastic atmospheric forcing which are linear in nature and would not exist without the energy from the external stochastic forcing.

Stochastic forcing has been used to model fluctuating freshwater fluxes (e.g. Mikolajewicz and Maier-Reimer 1990, Mysak et al. 1993, Spall 1993, Weisse et al. 1994, Pierce et al. 1995, Aeberhardt et al. 2000), thermal fluxes (e.g. Griffies and Tziperman 1995, Saravanan and McWilliams 1997, Kravtsov and Ghil 2004) and surface winds (e.g. Holland et al. 2001, Herbaut et al. 2002). Identifying spatial patterns of stochastic forcings that effectively excite oscillations in the THC has been the focus of many studies (e.g. Capotondi and Holland 1997, Saravanan and McWilliams 1997, Tziperman and Ioannou 2002, Zanna and Tziperman 2008, Sevellec et al. 2008). Using a 3 box model Tziperman and Ioannou (2002) determined the optimal spatial structure of the noise that resulted in maximal variance of the THC variability. It was shown that the optimal forcing induces low-frequency variability by exciting the salinity variability modes of the THC. However, the highly truncated structure of the 3 box model makes it impossible to answer the question of whether observations project onto these optimal modes: more complex models are needed to answer this question. Capotondi and Holland (1997) on the other hand considered the spatial pattern of stochastic forcing as a variable of the problem in their study that utilized the Cox (1984) version of the GFDL ocean GCM. The

period of oscillation of the THC was found to be independent of the spatial pattern, leading to the conclusion that the variability at the decadal timescale was an internal mode of the system and not associated with some characteristics of the forcing (although the amplitude of the response was found to depend on the spatial structure of the forcing). Saravanan and McWilliams (1997) found that spatial resonance (the forcing of a system with a spatial pattern resulting in oscillations of a preferred frequency) was responsible for exciting the oceanic decadal oscillation in their idealized ocean-atmospheric model coupled to a zonally averaged sector ocean.

The North Atlantic Oscillation (NAO) is one of the dominant large-scale modes of atmospheric and climate variability at middle and high latitudes. It is an alternation of atmospheric mass between the Arctic and subtropical Atlantic which varies on interannual-to-interdecadal timescales. The NAO is described by positive and negative phases with the positive phase characterised by a low pressure anomaly over the Arctic and Icelandic regions and a high pressure anomaly across the Azores. The result of these pressure differences is stronger than normal westerlies along the North Atlantic storm track which contributes to winters that are anomalously warm and wet in Europe and anomalously cold and dry in Canada and Greenland. The negative phase is weaker than the positive and tends to reduce the frequency and severity of storms along the North Atlantic storm track (Marsh 2000). Spatial patterns of heat flux variations that bear a strong resemblance to the North Atlantic Oscillation (NAO) have been found to drive multidecadal THC fluctuations in the GFDL ocean model (Delworth and Greatbatch 2000), HadCm3 coupled global ocean-atmosphere-sea-ice model (Dong and Sutton 2005) and the Bergen Climate Model (Bentsen et al. 2004). Using the new Southampton

Oceanography Centre air-sea flux dataset Marsh (2000) computed a surface-forced THC that supported his hypothesis that the NAO drives interannual-to-decadal variability in the THC.

While many studies have focused on the stability and variability of the THC in response to stochastic forcing very few have investigated the nonnormal dynamics of a stochastically forced THC. The existence of transiently growing (if asymptotically stable) perturbations in nonnormal systems makes the forced response of such systems particularly sensitive to the spatial structure of the forcing. Previous studies (Lohmann and Schneider 1999, Tziperman and Iaonnou 2002, Zanna and Tziperman 2008 in press, Sevellec 2006) have calculated the stochastic optimals for models of the THC but this analysis is the first to consider a model as complex as the WS model and to consider both temperature and salinity forcing. In this chapter the ideas of generalized stability theory will be used to analyze THC variability in response to high-frequency external forcing. In particular the spatial patterns of stochastic forcing that lead to enhanced variability of the THC will be calculated.

5.2 Response of the nonnormal system to continuous forcing

When a system that is governed by a normal operator is forced it exhibits a large response (that is, resonance) only if the forcing frequency is close to the oscillation frequency associated with one of the eigenmode pairs. In contrast, a system governed by a nonnormal operator may exhibit "resonance" at frequencies far from those of individual eigenmode (pairs). The optimal initial conditions found in Chapter 4 are examples of impulsive forcing but in geophysical systems the forcing will usually be continuous in time.

Some examples of surface mechanical and buoyancy forcings that drive the THC are evaporative and heat fluxes, precipitation, sea ice advection and melting, wind stresses and ocean eddy activity. Traditionally, an analysis of the eigenvalues alone has been used to give information about the resonance of a system subject to forcing. For a normal operator the preferred frequencies of a forced response are the eigenvalues of the linear operator that governs the system and the form of the response is associated with the corresponding eigenfunctions. Asymptotically stable nonnormal dynamical systems which exhibit large transient growth of perturbations also exhibit enhanced response to harmonic forcing (relative to a normal dynamical system with the same eigenspectrum).

Useful insight into the consequences of nonnormality for the dynamics of a linear system can be obtained by examining the tangent linear model driven by a harmonic signal of the form $V(t) = e^{zt} f$ where f is a constant vector and z is the complex forcing frequency. This system can be described by the equation $dP/dt = AP + e^{zt} f$ whose

solution is $P(t) = e^{zt}(zI - A)^{-1} f$. Thus, the resolvent of A, defined to be $R(z) = (zI - A)^{-1}$, can be interpreted as the operator that transforms forcing "inputs" of frequency z into corresponding response "outputs". The degree of resonant amplification that occurs in this process is equal to the resolvent norm, $\|R(z)\| = \|P(t)\| / \|e^{zt} f\|$. The resolvent is singular for values of z in the eigenspectrum of A, $z \in \sigma(A)$ (where the spectrum $\sigma(A)$ is the set of eigenvalues of A). The response of a nonnormal system is significantly larger at all frequencies than that anticipated from classical resonance arguments. This amplification effect is referred to as pseudoresonance (Trefethen and Embree 2005) and is expressed mathematically by the Bauer-Fike theorem which states that

$$1/dist(z, \sigma(A)) \leq \|R(z)\| \leq \mathrm{K}(E)/dist(z, \sigma(A)) \tag{5.1}$$

where $dist(z, \sigma(A))$ denotes the shortest distance of z from the spectrum of A in the complex plane and $\mathrm{K}(E) = \|E\|\|E^{-1}\|$ is defined as the condition number of the matrix E formed by the eigenvectors of A arranged in columns. In general, $1 \leq \mathrm{K}(E) < \infty$ with $\mathrm{K}(E) = 1$ if and only if A is normal. For a normal system, $\|R(z)\|$ is only large for z near an eigenvalue of A. For nonnormal matices $\mathrm{K}(E) > 1$ and the resolvent norm $\|R(z)\|$ will in general be greater than for a normal system with the same eigenspectrum. Figure 5.1 displays a plot of $\|R(z)\|$ versus Im(z) for the purely harmonic forcing case of Re(z)=0 for the tangent linear WS model with eigenspectrum $\sigma(A)$. Also shown is 1/dist(z,σ(A)) vs. Im(z) which corresponds to the response to harmonic forcing of a normal matrix with the same eigenspectrum. As expected the large nonnormal growth in

this system which was demonstrated in Chapter 4 leads to a response to harmonic forcing that is an order of magnitude larger than an equivalent normal response. Also noteworthy in Figure 5.1 is that the maximum response of the system to external forcing occurs at low frequencies.

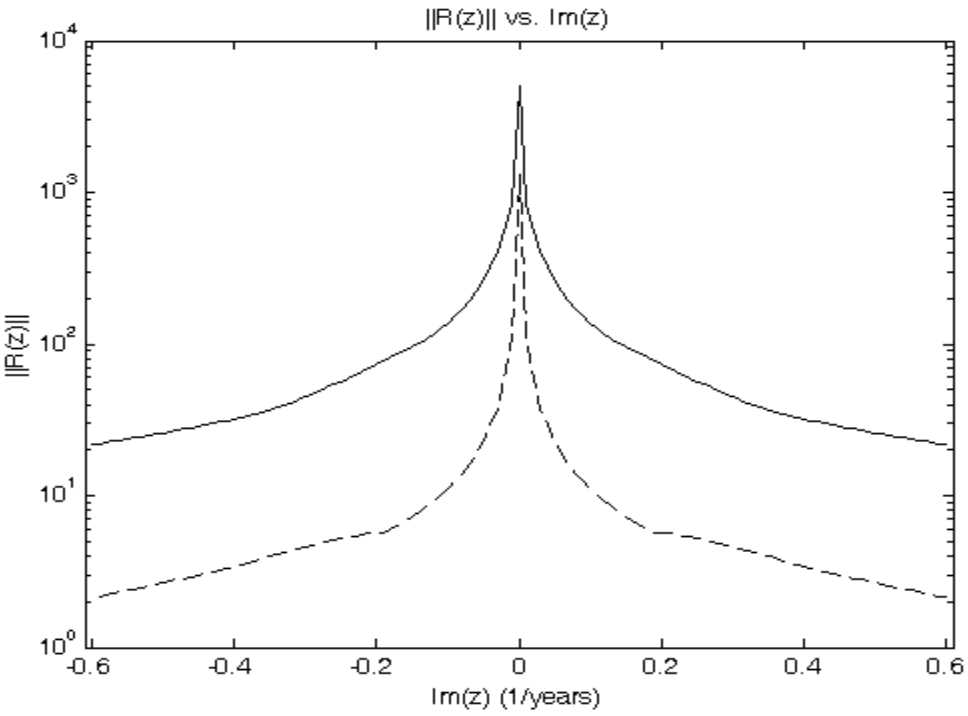

Figure 5.1. The norm of the resolvent ||R(z)|| vs. Im(z) (solid line) for the tangent linear WS model with eigenspectrum z. Also shown is 1/dist(z,σ(A)) vs. Im(z) (dashed line) for the same eigenspectrum.

The set of z such that $\|R(z)\| > \varepsilon^{-1}$ for any arbitrary ε>0 is called the ε-pseudospectrum of A. In words this means the ε-pseudospectrum is the open subset of the complex plane bounded by the ε^{-1} level curves of the norm of the resolvent (Trefethen and Embree 2005). The behavior of nonnormal matrices can be captured by plotting a few contour lines of their ε-pseudospectrum. Each contour line can be interpreted as a

line of equal resonance magnitude. If a complex frequency z belongs to an ε-pseudospectrum then an O(1) response is possible from an O(ε) forcing at this frequency. The Hille-Yoshida theorem states that if the ε-pseudospectrum of a matrix with negative real eigenvalues crosses the positive real axis such that the maximum value of Re(z) is greater than ε then there must always be transient growth (Trefethen and Embree 2005). This means that, $\left\|e^{tA}\right\| > 1$ only if $\sup_{z\in\rho} \mathrm{Re}(z) > \varepsilon$ for Re(z)>0, where ρ is a contour of constant ε. Note that for a normal operator epsilon-contours of the resolvent will cross the positive real axis for some values of epsilon, but transient growth will not be possible as the condition $\sup_{z\in\sigma_\varepsilon(A)} \mathrm{Re}(z) > \varepsilon$ is not met. While eigenvalues fail to capture the transient amplification of perturbations in a nonnormal system the ε-pseudospectrum provides a more geometric perspective. The ε-pseudospectrum for the two dimensional matrix defined in Chapter 2 is shown in Figure 5.2 for the highly nonnormal case of $\theta = \pi/100$ (Figure 5.2a) and the slightly nonnormal case of $\theta = \pi/10$ (Figure 5.2c). Also reproduced here for comparison are the plots of $\left\|e^{tA}\right\|$ in each case (Figures 5.2b & d). These plots clearly show that the farther the contours of the ε-pseudospectrum extend into the right half plane the greater the degree of nonnormality and the greater the degree of transient amplification.

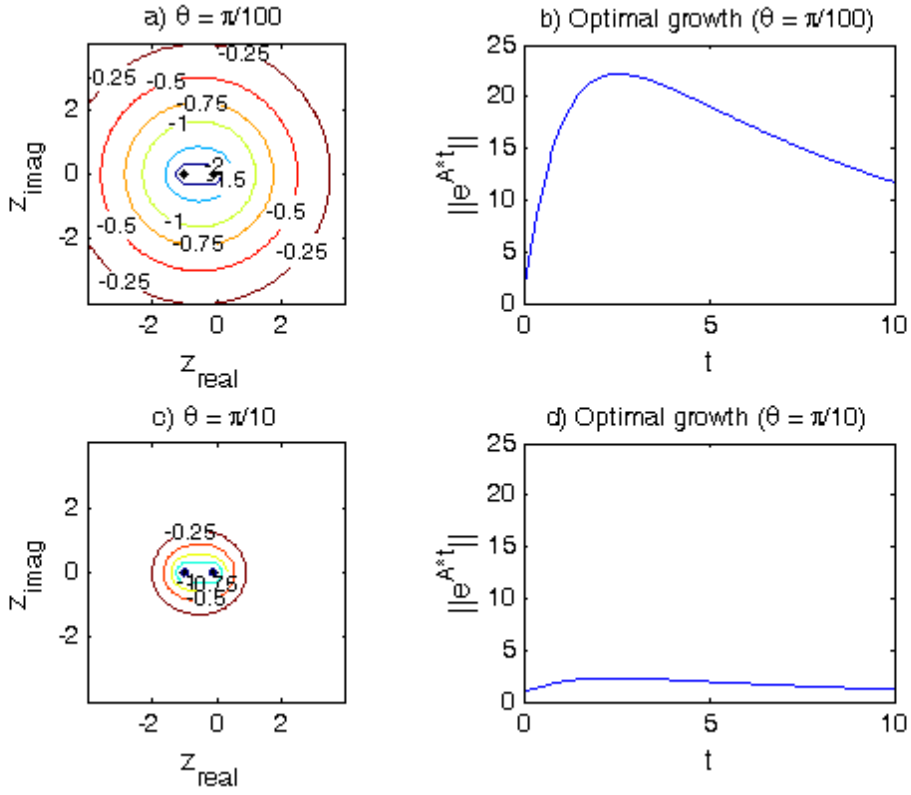

Figure 5.2. Illustration of the relationship between ε-pseudospectrum and transient growth for the two dimensional matrix defined in Chapter 2. Contour values are $\log_{10}(\varepsilon)$. a) ε-pseudospectra for $\theta = \pi/100$, b) $\left\|e^{tA}\right\|$ vs time for $\theta = \pi/100$, c) ε-pseudospectra for $\theta = \pi/10$ and d) $\left\|e^{tA}\right\|$ vs time for $\theta = \pi/10$.

The ε-pseudospectrum of the linear tangent WS model for $\varepsilon = 10^{-4}, 10^{-3}, 10^{-2}, 10^{-1.5}, 10^{-1.25}, 10^{-1}$ is shown in Figure 5.3. The eigenspectrum, $\sigma(A)$, of A is denoted by dots in the complex plane of Figure 5.3. For each contour value ε plotted in this figure the largest value of Re(z) that is found on each contour (indicated by an asterisk for selected contours) exceeds ε, (i.e. $\sup_{z\in\rho} \mathrm{Re}(z) > \varepsilon$). Figure 5.4 shows $\sup_{z\in\rho} \mathrm{Re}(z)$ versus ε. The dotted line defines the boundary of the region below which transient amplification does not occur. The solid line representing the results for the

present case is well above the dotted line (consistent with the fact that the system governed by the tangent linear operator of the WS model undergoes large transient growth of perturbations, as discussed in the previous chapter)

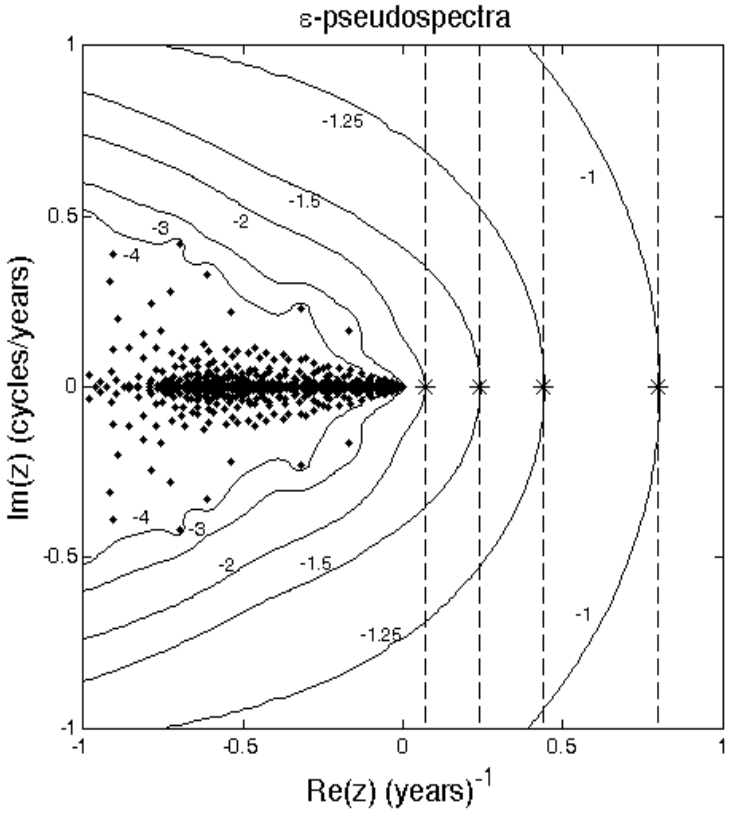

Figure 5.3 ε-pseudospectrum for the tangent linear operator of the WS model. Contour values are $\log_{10}(\varepsilon)$. The asterisks and corresponding dashed lines indicate $\sup_{z\in\rho} \mathrm{Re}(z)$ for selected values of ε.

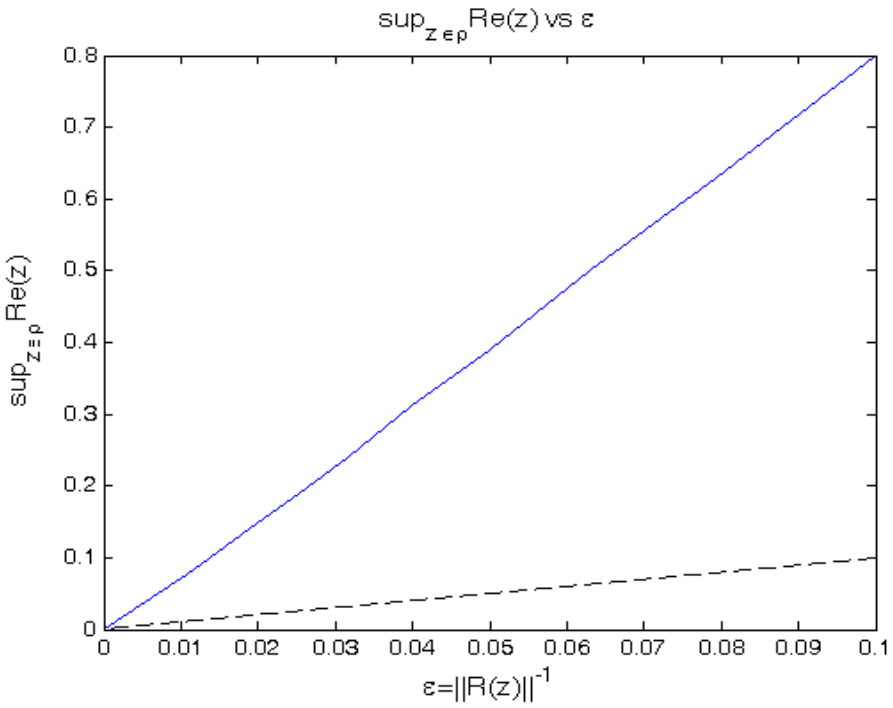

Figure 5.4. $\sup_{z\in\rho} \mathrm{Re}(z)$ versus ε for linear tangent WS model (solid line) and the 1:1 ratio (dashed line) below which transient growth is not possible.

5.3 Response of the system to stochastic forcing

The stochastically forced linear tangent model can be written as

$$\frac{dP}{dt} = AP + Ff(t) \tag{5.2}$$

where A is the linearised dynamical operator calculated numerically using the full nonlinear WS ocean model after it has been run to steady state for 12,000 years as described in Chapter 4, F is a matrix operator restricting the noise to the surface boxes only (i.e. $F(i,i) = 1$ for the i^{th} surface box and $F(j,k) = 0$ for all other boxes) and $f(t)$ is the stochastic forcing term. As the matrix F is diagonal, the surface forcing is also spatially uncorrelated. The solution to this equation is

$$P(\tau) = e^{A\tau}P(0) + \int_0^\tau ds e^{A(\tau-s)}Ff(s) = B(\tau,0)P(0) + \int_0^\tau dsB(\tau,s)Ff(s) \qquad (5.3)$$

where $B(t,s) = e^{A(t-s)}$ is the propagator from time s to time t. This solution is bounded since all of the eigenmodes of the dynamical operator decay exponentially with time. The initial condition term vanishes for large times since A is stable and therefore does not affect the stationary variance of the system. Thus this term is assumed to be zero without loss of generality. For simplicity, it is assumed that the forcing is a white-noise process with zero mean and uncorrelated in time, and that the statistics of the noise are separable in space and time, i.e. $\langle f_i \rangle = 0$ and $\langle f_i(t_m) f_j(t_n) \rangle = Q_{ij}\delta_{mn}$. The brackets $\langle\ \rangle$ denote an average over an ensemble of forcing functions and δ_{mn} is the Kronecker delta function. The matrix Q is called the spatial covariance matrix of the noise. The trace of Q can be interpreted as the rate at which random forcing injects variance into the system (DelSole 2003).The total response variance of the THC defined using the norm kernel X is

$$Var(\|P\|) \equiv \langle P_i(t) X_{ij} P_j(t) \rangle - \langle P_i(t) \rangle X_{ij} \langle P_j(t) \rangle \qquad (5.4)$$

This expression can be written in terms of the trace operator, $\mathrm{var}(\|P\|) = Tr(ZQ)$, (Tziperman and Ioannou, 2002) where

$$Z = \int_0^t dsF^T B^T(\tau,s) XB(\tau,s)F \qquad (5.5)$$

The eigenvectors of Z are called the stochastic optimals. They form a complete set of spatially orthogonal vectors that can be ordered by their eigenvalues (all of which are positive (Kleeman and Moore 1997)). The eigenvector with largest eigenvalue is referred to as the first stochastic optimal; forcing in this direction maximizes variance relative to

forcing in all other directions. Similarly, the second stochastic optimal will maximize variance over all possible structures that are orthogonal to the first, and so on for higher order optimals. As the stochastic optimals define a complete, orthogonal set of vectors, an arbitrary forcing function can be written as a sum of stochastic optimals and the response is governed primarily by the projection of the forcing on the leading optimals. If the forcing were composed of all the stochastic optimals with each contributing equally to the forcing then the fraction of the stochastic forcing variance explained by each stochastic optimal is the ratio of the eigenvalues of Z, ζ_i, to total response variance, $\zeta_i / Tr(Z)$ (Kleeman and Moore 1997).

The stochastic optimals of the linear tangent operator for the WS model are obtained from a 100-year integration of the discretized version of Eq. (5.5) with a time step of 5 days.

The matrix Z is independent of the integration time as long as this time is sufficiently longer than the optimization time of transient amplification, in this case 6 years (Tziperman and Ioannou 2002). Using the entire state vector to define Z yields 800 stochastic optimals (equal to the number of ocean grid points). The surface components of the stochastic optimals are obtained by multiplying by the matrix operator F; although the stochastic optimals have an expression throughout the entire domain of the model, only the surface structure is relevant to the response to fluctuating surface forcing. For this system, the external forcing cannot project entirely along the stochastic optimals. The fraction of variance explained by the first 20 stochastic optimals $\zeta_i / Tr(Z)$ is shown in Figure 5.5, which reveals that the first stochastic optimal accounts for nearly twice the

variance as the second. The first 20 of the total 800 stochastic optimals account for 78% of the total variance.

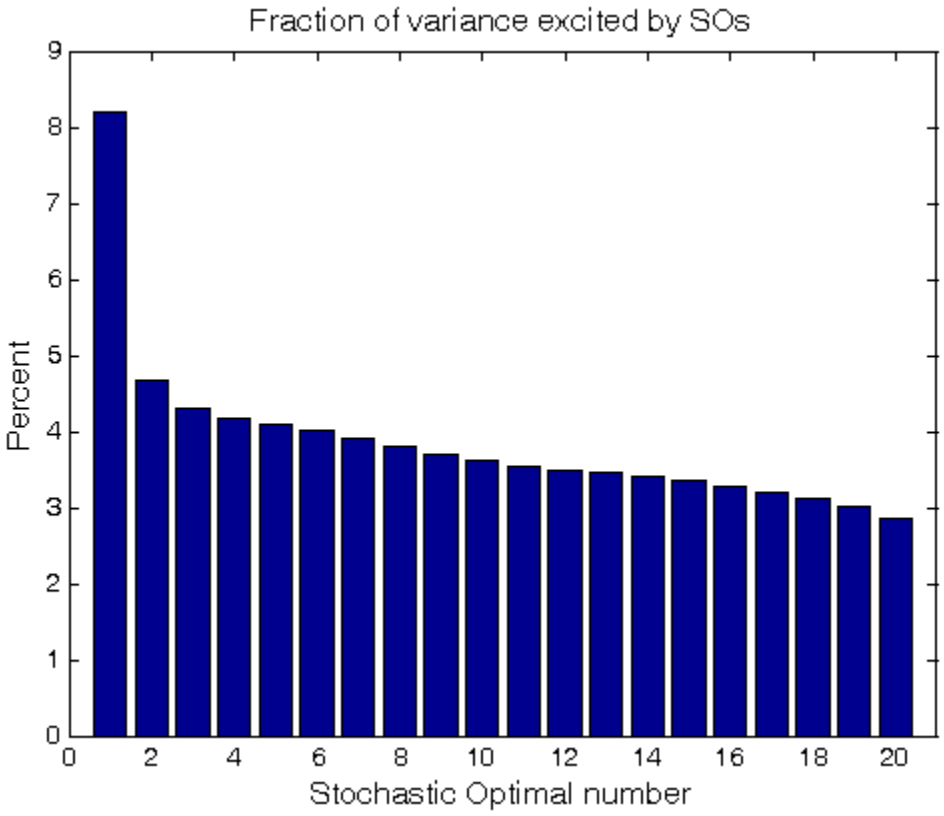

Figure 5.5. The percentage of variance, $\zeta_i / Tr(Z) * 100\%$, of the (spatially homogeneous and uncorrelated) stochastic forcing explained by each of the first 20 stochastic optimals where the $\zeta_i^{'} s$ are the eigenvalues of Z.

The temperature and salinity structures of the first two stochastic optimals (SO1 and SO2) are shown in Figures 5.6a) through d). For comparison the surface components of optimal initial temperature and salinity perturbations calculated from the linearised model equations that maximize the transient amplification of the THC on a timescale of 6 years (Chapter 4) are shown as dashed lines. The first stochastic optimal exhibits most of its structure at high latitudes with a salinity component of opposite sign and two orders of

magnitude larger than the temperature component. The spatial structure of the surface optimal initial conditions is nearly identical to that of the first stochastic optimals. Therefore the first stochastic optimal is expected to induce perturbations to the THC that will rapidly amplify.

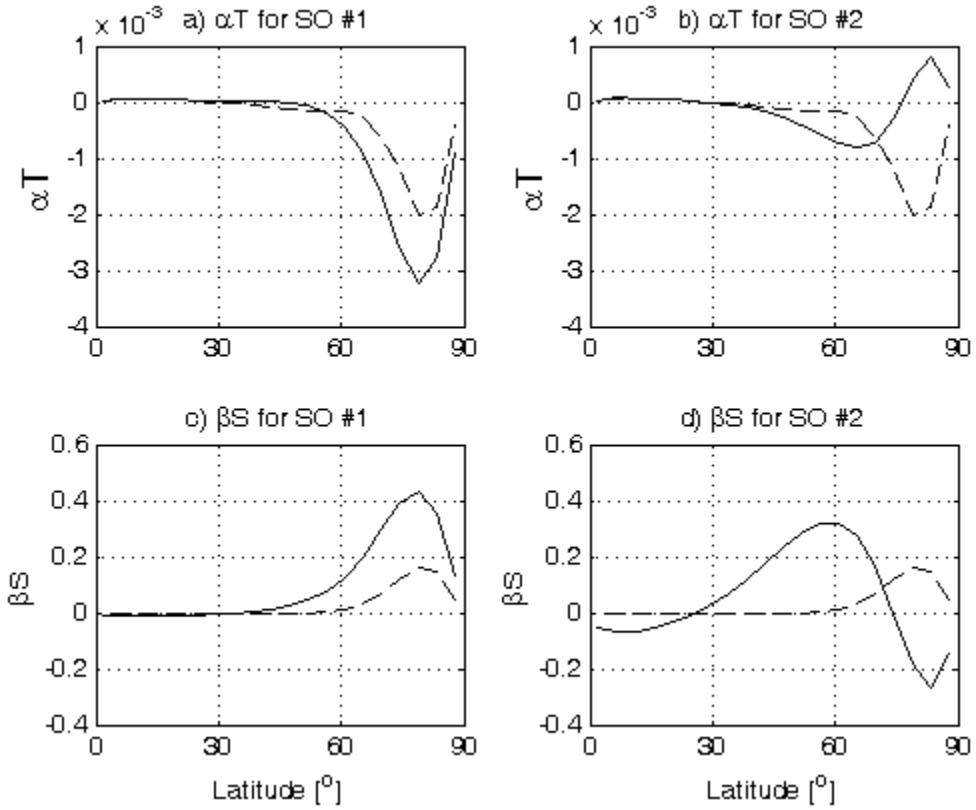

Figure 5.6. a) αT for SO1 (solid line), b) αT for SO2 (solid line), c) βS for SO1 (solid line) and d) βS for SO2 (solid line). Also shown in each plot as dashed lines are the corresponding values for the surface component of the optimal initial conditions, P0.

An optimal perturbation is an initial condition that optimizes spatial variance at a specified lead time (for this case, 6 years). In contrast, a stochastic optimal is a forcing function that optimizes spatial variance over the ensemble mean (or long times). The matrix Z is simply the time integral of the matrix that describes the evolution of the

magnitude of a perturbation with the constraint that the forcing is confined to surface boxes of the ocean. Because the optimal perturbation leads to an amplification of the THC norm defined in Eq. (4.5) that is more than 50% larger than the amplification that results when the next optimal perturbation vector is used as the optimal initial conditions the integral is dominated by the behavior of the system on the timescales of this perturbation. The major difference between the optimal initial conditions and the stochastic optimals is that the former's full spatial structure throughout the ocean basin is taken into account while the latter are limited to the surface boxes by the forcing matrix F : thus, while the surface expressions of the two structures are the same, the stochastic optimals do not project perfectly on the optimal perturbations. Nonetheless, the fact that the surface components of the optimal initial conditions are very similar to the stochastic optimals leads one to expect that the eigenmodes of the system that are responsible for transient amplification will also be the eigenmodes that are responsible for the large maintained variance of the system when forced with noise that projects strongly on the structure of the stochastic optimals (as will be discussed in detail later on).

The spatial structure of the second stochastic optimal shown in Figures 5.6b) and d) is significantly different than the first. Both the salinity and temperature components exhibit structure over a wider range of latitudes with each having two extrema; the dominant peaks at high latitudes are of the opposite sign to that of the first stochastic optimal. The salinity perturbation at very low latitudes is nonzero for the second stochastic optimal. For both of the first two optimals the salinity component is many orders of magnitude larger than the temperature component from which it can be

concluded that the stochastically induced response of the THC is dominated by the freshwater forcing component of the noise.

For stochastic forcing with the structure of the first stochastic optimal the discretized version of Eq. (5.2) can be written $P_{n+1} = P_n + \Delta t(AP_n + F\xi SO1)$ where P is the state vector of temperatures and salinities, A is the tangent linear operator of the WS model, ξ the white noise term (Gaussian with standard deviation $1/\sqrt{\Delta t}$) and SO1 is the first stochastic optimal vector. As the stationary covariance matrix C satisfies the Lyapunov equation $AC + CA^T = -FF^T$ (Farrell and Ioannou 1993a) the resulting variance of the THC anomaly is proportional to $Tr(FF^T)$. In all experiments the matrix F was scaled so that all nonzero diagonal elements of FF^T took the value 10^3. The integration of this equation was carried out for 1000 years with a time step of 5 days. A second model run was also done using the spatial pattern of SO2 in the stochastic forcing term. The time series of the norm defined in Eq. (4.3) for each of the two model runs are shown in Figures 5.7a) and b). As expected, the THC exhibits significantly more variance when forced with the first stochastic optimal than it does when forced with the second. Also shown in Figure 5.7c) are the time series of the temperature and salinity contributions to the norm for forcing with the first stochastic optimal. While the contribution from the salinity component is larger than that from the temperature component as would be expected from the magnitude of the salinity component of the first stochastic optimal, the temperature variability is more than an order of magnitude larger than would simply be expected from the stochastic optimals because of the

nonnormal nature of the response. The salinity-dominated optimal stochastic forcing excites a strong temperature response.

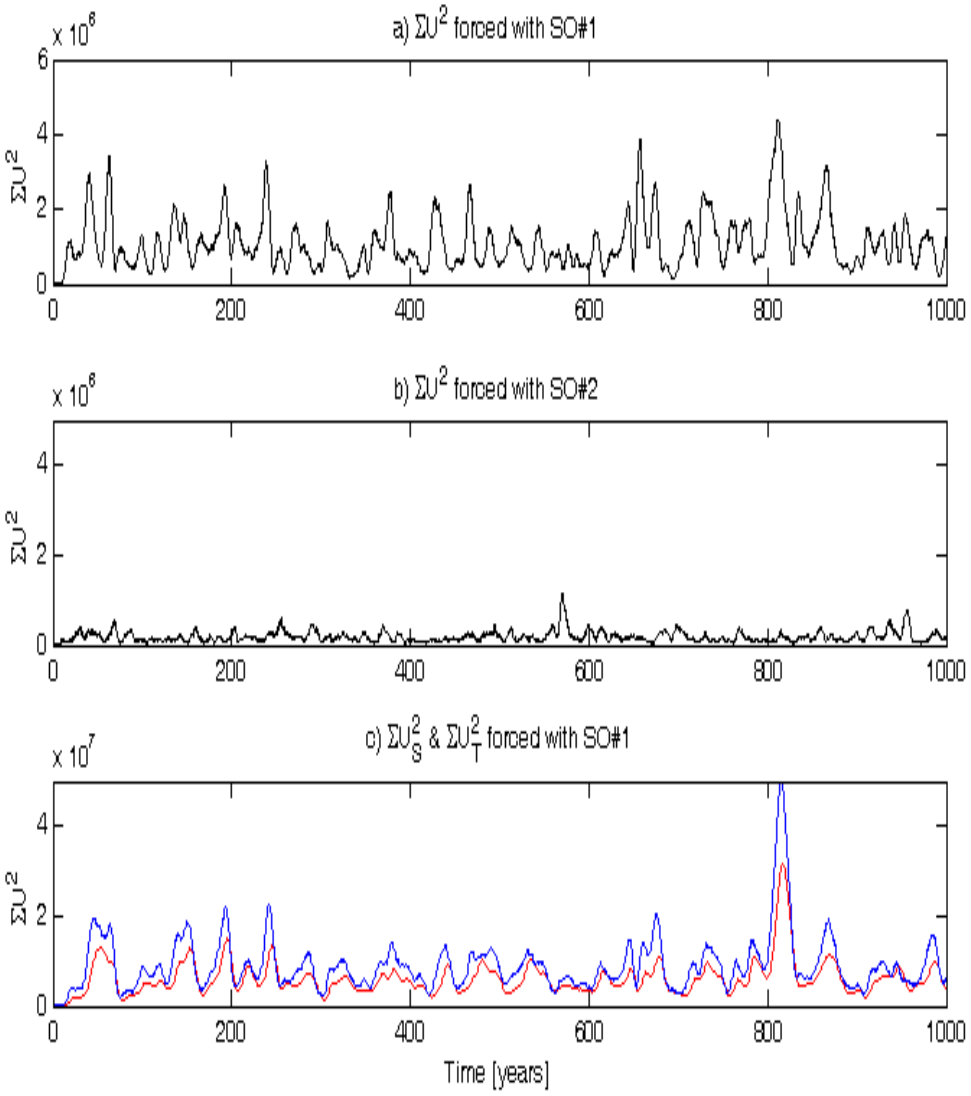

Figure 5.7.a) Time series of the norm ΣU^2 when the linear model is forced with SO1, b) Time series of the norm ΣU^2 when the linear model is forced with SO2 and c) time series of the temperature (red line) and salinity (blue line) components of the norm when the linear model is forced with SO1.

As a further illustration of the importance of the spatial structure of the first stochastic optimal in producing increased variance of the THC the linear model was stochastically forced with spatially uncorrelated white noise. The time series of the norm and its temperature and salinity components are shown in Figure 5.8. as expected from the fraction of variance explained by the first stochastic optimal (Figure 5.5) the resulting standard deviation of the norm for spatially uncorrelated forcing is significantly less than the variance obtained when the forcing had the spatial structure of the first stochastic optimal. It can also be seen from Figure 5.8 that the response to spatially uncorrelated noise has a high frequency component that is absent when the forcing has the spatial structure of the first stochastic optimal. In both cases the salinity component is stronger than the temperature component (although not substantially so).

The power spectral densities of the norm, $\sum U^2$, for the linear model forced with the first and second stochastic optimals are shown in Figure 5.9. Both spectra are basically red with most of the power in the stochastically induced response described by variance with periods greater than 10 years The spectra also do not show any significant peaks that indicate a preferred frequency of response: the forcing does not seem to be strongly exciting any oscillatory internal modes of variability. This is consistent with the results from Figure 5.1 which demonstrates that the largest response as measured by the resolvent norm occurs at forcing periods greater than 10 years. Eq. (5.1) shows that the norm of the resolvent is largely determined by the subset of the eigenspectrum that have largest Re(z) (i.e. the ones that are closest to the origin).

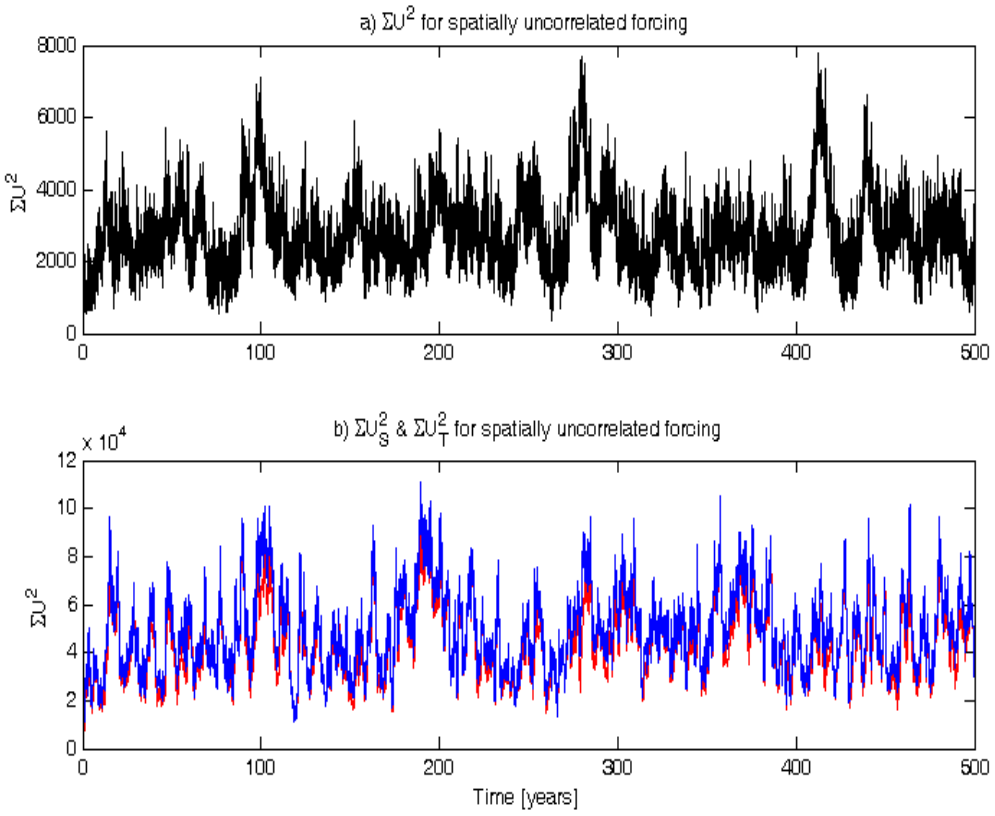

Figure 5.8. a) Time series of the norm ΣU^2 for spatially uncorrelated forcing and b) time series of the temperature (red line) and salinity (blue line) components of the norm for spatially uncorrelated forcing.

Figure 5.3 shows that this subset of eigenmodes tend to be very low frequency and therefore are not strongly oscillatory on the timescales considered in this study. The power spectral density for forcing with the second stochastic optimal has the same structure as for forcing with the first stochastic optimal but has a lower overall variance.

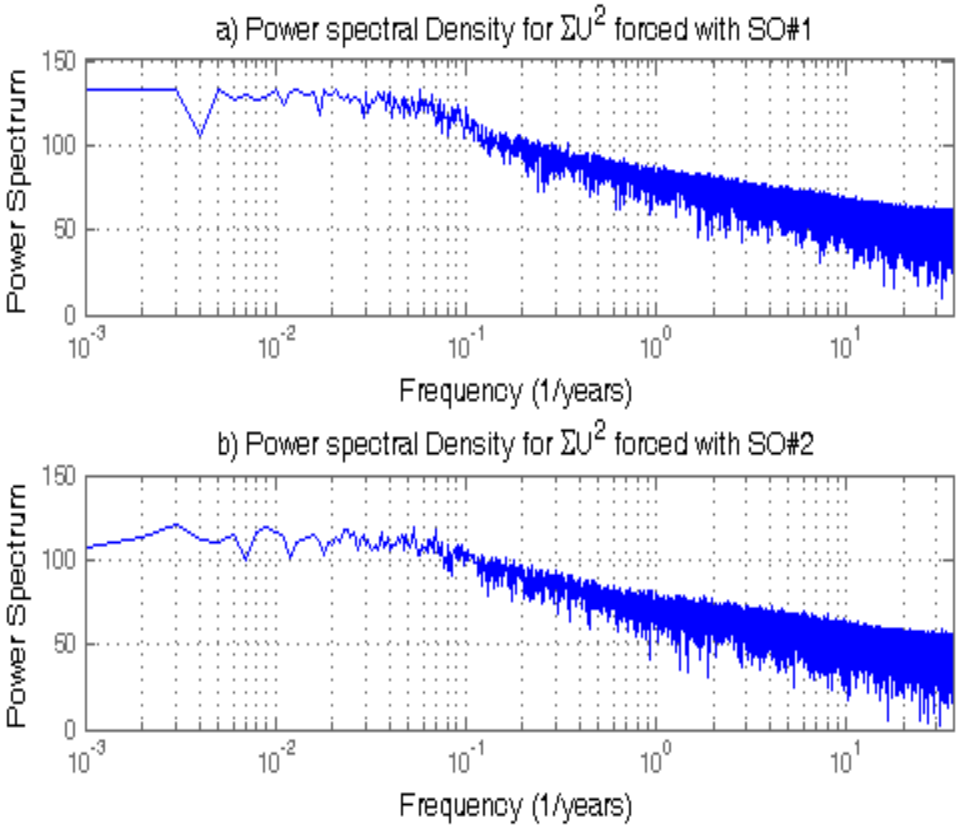

Figure 5.9. The power spectral density of ΣU^2 for the linear model forced with a) SO1 and b) SO2.

The power spectral density for the norm, $\sum U^2$, for the linear model forced with spatially uncorrelated noise is shown in Figure 5.10. The spectrum is still basically red but there is more energy concentrated at high frequencies than for the case of forcing with the first and second stochastic optimals. A hint of the peak that corresponds to the 227 year oscillation found by Mysak et al. (1993) is evident but not as prominent as in their results (in which spatially uniform random forcing of only the freshwater flux was considered).

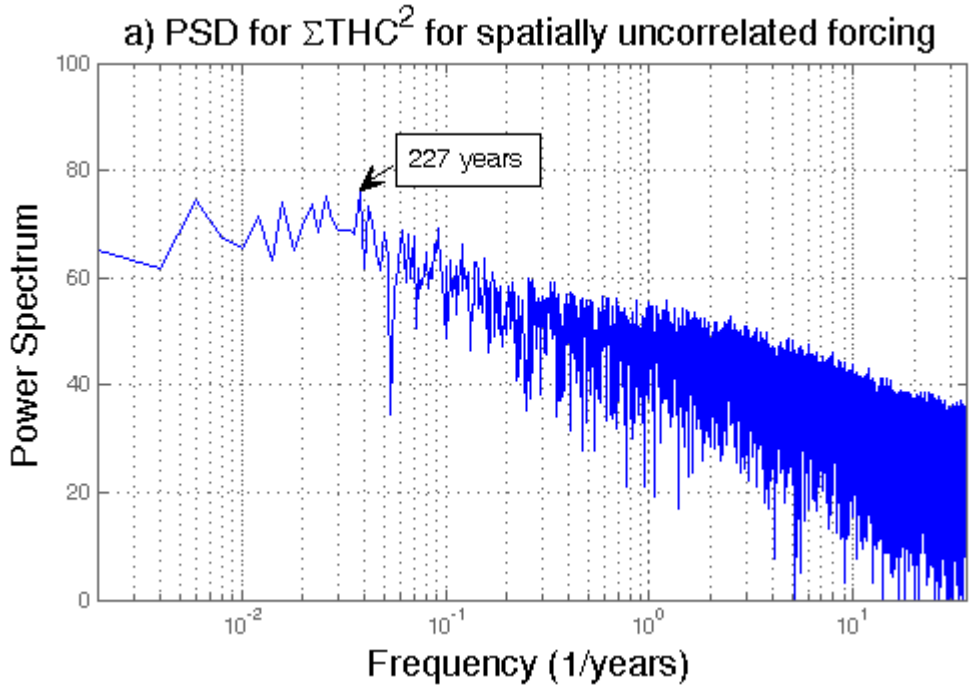

Figure 5.10. The power spectral density of ΣU^2 for the linear model forced with spatially uncorrelated noise.

The patterns that dominate the variance induced by the forcing are determined by calculating the Empirical Orthogonal Functions (EOFs, given by the eigenstructure of the covariance matrix) of the model's response to stochastic surface forcing. Each eigenvalue of the covariance matrix equals the variance accounted for by the pattern of its corresponding eigenvector. The pattern that corresponds to the largest eigenvalue is the first EOF. The stochastic optimals characterize the structures that excite large transient responses, while the EOFs are influenced by the superposition of the total time-integrated response to the forcing. The leading EOFs of temperature and salinity of the linearised model forced with the first and second stochastic optimals are displayed in Figure 5.11. The salinity EOFs account for 52% and 58% respectively of the induced salinity variance when forcing is from SO1 and SO2 respectively, while the temperature EOFs account

respectively for 44% and 37% of the temperature variance SO1 and SO2 respectively. In both cases, forcing with large-scale spatial structure excites a response with variability dominated by large-scale structures. Temperature EOF1 associated with forcing by SO1 (Figure 5.11a) is confined to the high latitudes and extends to the full depth of the ocean. In contrast the salinity component of the response (Figure 5.11c) extends to much lower latitudes even though the salinity component of the first stochastic optimal has a similar high latitude structure to the temperature component. Unlike the temperature component the salinity component is confined to the top 200 meters of the ocean. In other words the model's dominant response to stochastic temperature and salinity surface forcing is an intensive surface response for the salinity component and a milder deep response for the temperature component. The dominant pattern of the response of the model when forced with SO2 (Figures 5.11b and 5.11d) has a nearly identical temperature component as in the case of forcing with SO1 but has a salinity component with a dipole structure that extends to low latitudes.

Figure 5.12a) through f) shows the variance of the temperature and salinity fields as a function of latitude and depth for forcing with SO1, SO2 and spatially uncorrelated surface noise. The patterns of variance for forcing with SO1 and SO2 are very similar to the patterns of EOF1 for the same forcing. In addition to showing the spatial regions of large variance the plots in Figure 5.12 also show that overall the variance of the temperature and salinity fields is significantly larger for forcing with SO1 than for forcing with either SO2 or spatially uncorrelated surface noise. These variance plots

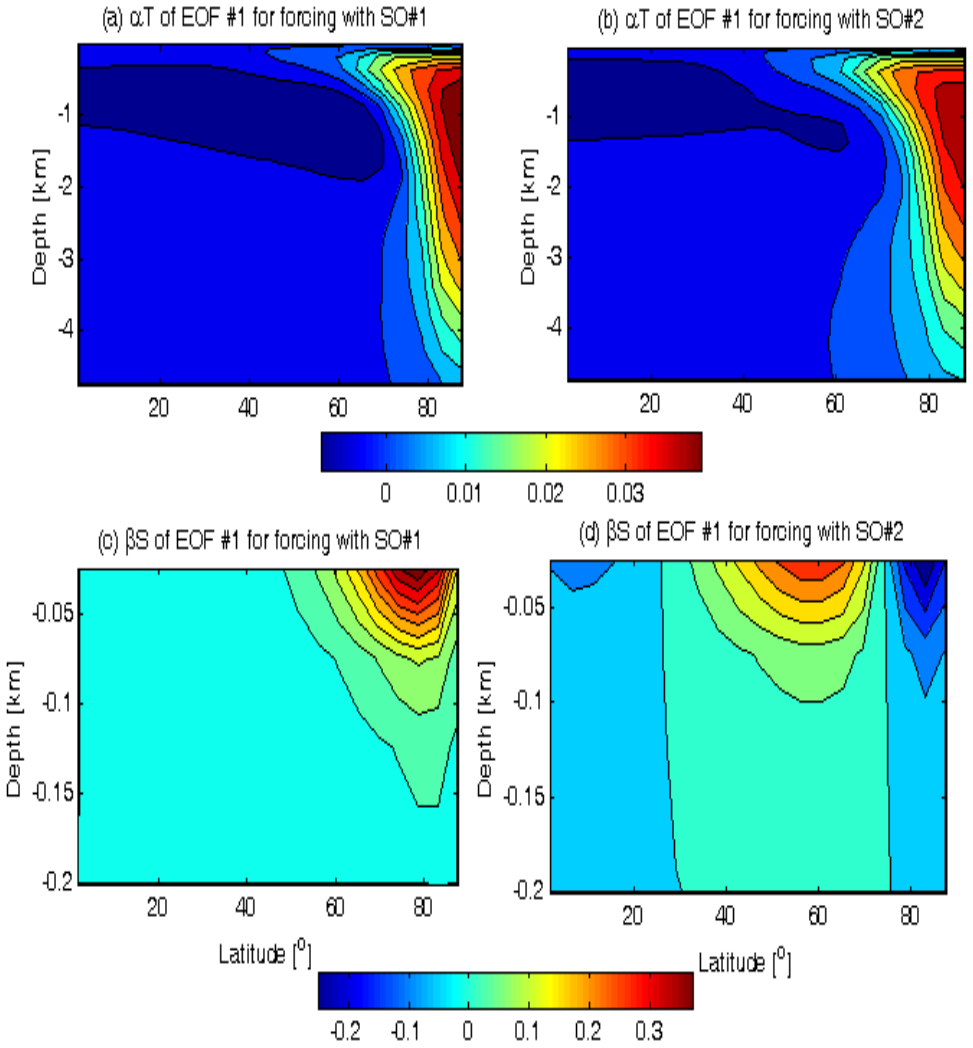

Figure 5.11. The first EOF of the response of the temperature and salinity of the linearised model forced with the first and second stochastic optimals. a) αT of EOF 1 for forcing with SO 1, b) αT of EOF 1 for forcing with SO 2, c)βS of EOF 1 for forcing with SO 1 and d) βS of EOF 1 for forcing with SO 2. Note that the maximum depth in c) and d) is 200m.

confirm the picture formed by the leading EOFs: the temperature response to optimal stochastic forcing is confined to high latitudes and extends to great depths while the salinity response occurs over a wider range of latitudes and is confined to the surface. The temperature and salinity responses to surface uncorrelated spatial forcing are

confined to the top 100 meters of the ocean with the greatest variance at the surface. The variance patterns for both salinity and temperature in this case have a steep vertical gradient but are uniform across all latitudes.

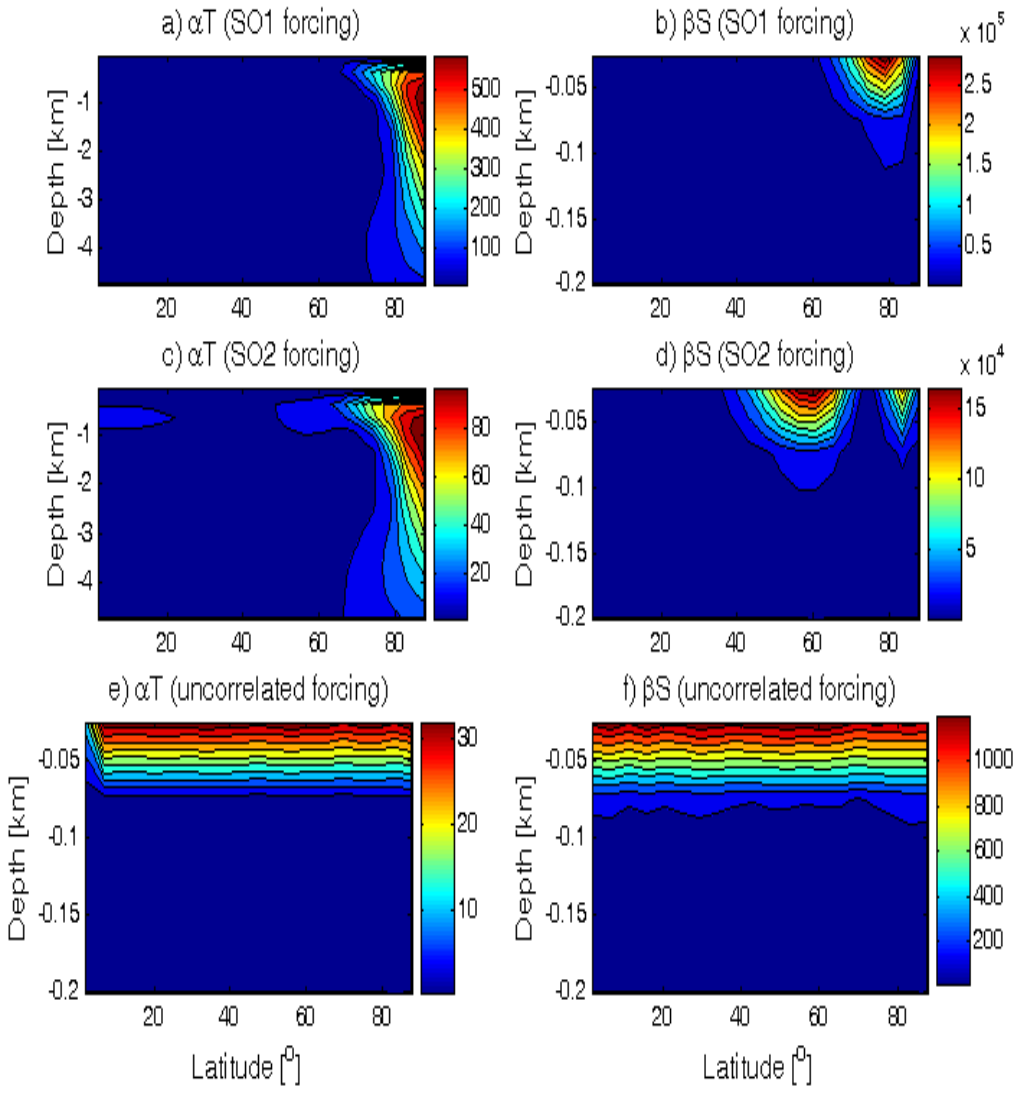

Figure 5.12. Variance of a) αT with forcing with SO1, b) βS with forcing with SO1, c) αT with forcing with SO2, d) βS with forcing with SO2, e) αT with forcing with uncorrelated noise and f) βS with forcing with uncorrelated noise.

To investigate the eigenmodes of A that are responsible for the structure of the stochastic optimals each stochastic optimal vector is written as the linear superposition of the eigenmodes of A, i.e. $SO = \sum_{k=1}^{k=800} a_k \hat{s}_k$ where $a_k = \hat{r}_k SO / \hat{r}_k{}^T \hat{s}_k$ are the projection coefficients (Chapter 2). A plot of each set of 800 projection coefficients for all 800 stochastic optimal vectors is shown in Figure 5.13. Those eigenmodes that have consistently large projection coefficients are the ones that are favored by the stochastic optimal vectors. It can be seen in Figure 5.13b) that 5 modes have consistently large projection coefficients. Two are oscillating complex conjugate pairs, the first pair with decay and oscillation timescales of 0.72 years and 1420 years respectively and the second pair with decay and oscillation timescales of 0.63 years and 478 years respectively. The other three favored eigenmodes are purely decaying ones with decay times of 0.65 years, 0.65 years and 0.63 years respectively. These five eigenmodes that have maximum projections onto the stochastic optimals were also found to be the same five highly nonnormal eigenmodes of the tangent linear matrix A that were critical to the structure of the optimal initial perturbations that lead to transient amplification of the THC on a timescale of 6 years (Chapter 4).

As discussed in Chapter 2 a measure of nonnormality of an eigenmode can be quantified by $\nu(k)$. A plot of $\nu(k)$ versus $\mathrm{Im}(\lambda_k)$ for each eigenmode of the tangent linear operator of the WS model A is given in Figure 5.14. The eigenmodes (indexed by k) are arranged according to increasing modulus of the eigenvalues of A. The largest values of $\nu(k)$ typically occur at low frequencies The top 5 eigenmodes identified in

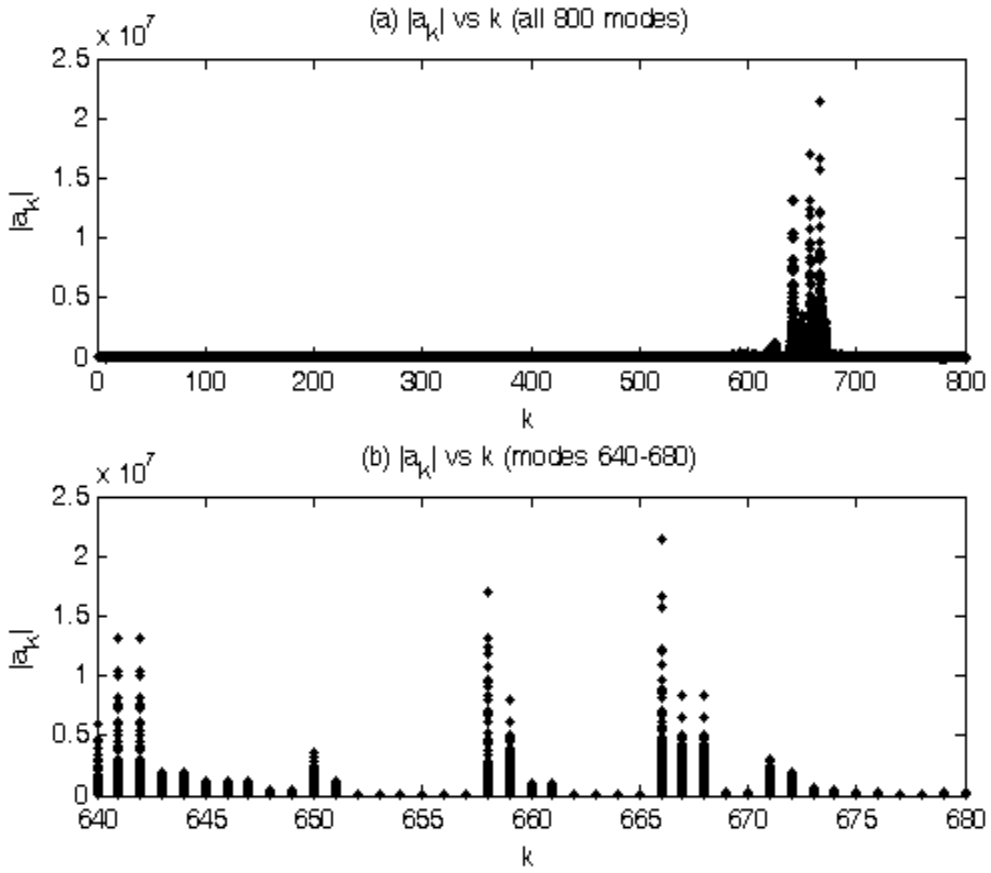

Figure 5.13. a) Projection coefficient computed by projecting each stochastic optimal vector onto the full set of 800 eigenmodes of A (k=1,..,800) and b) projection coefficients for eigenmodes k=640,..,680

Figure 5.13 are denoted by open circles in Figure 5.14, where it can be seen that they are some of the most nonnormal modes (large $\|v_k\|$) and correspond to low-frequency modes.

Plots of $\|v_k\|$ vs. $\|a_k\|$ for all 800 stochastic optimals and for just the first stochastic optimal are presented in Figures 5.15a) and 5.15b) respectively where it is confirmed that the most highly non-normal eigenmodes are among the eigenmodes that project most strongly onto SO1. The three modes with largest values of a_k (Figure 5.15b)

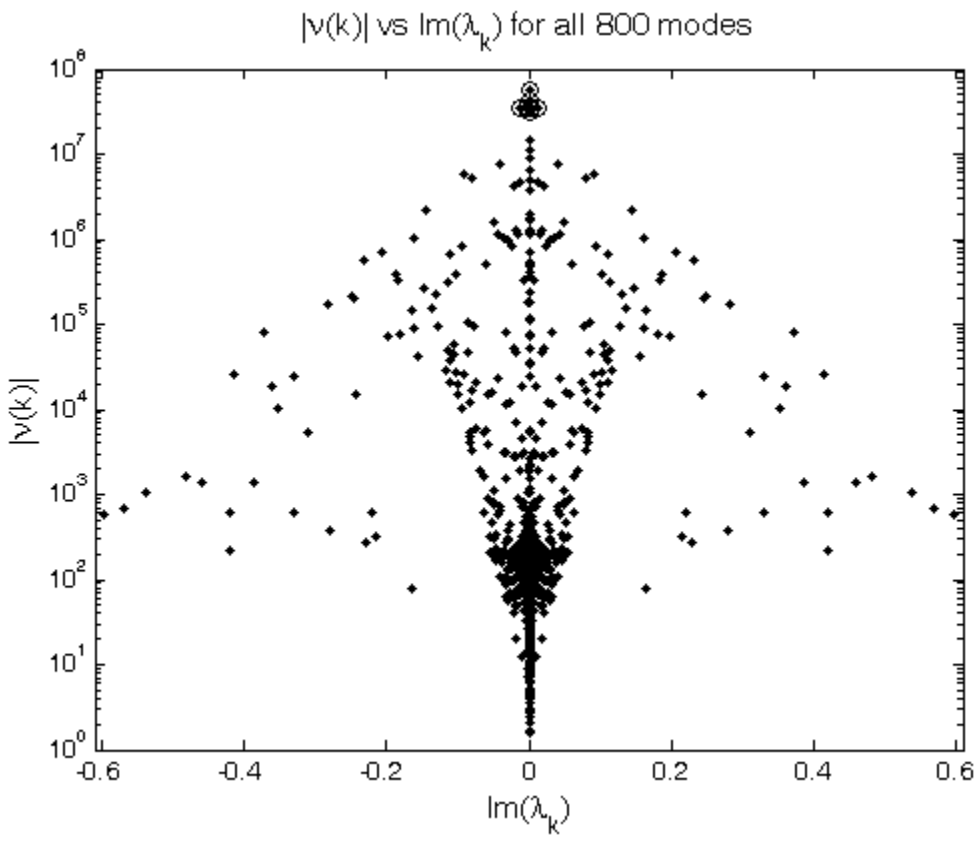

Figure 5.14. $\nu(k)$ vs. $\mathrm{Im}(\lambda_k)$ for each eigenmode k=1..800. The preferred eigenmodes by the stochastic optimal vectors correspond to the open circles.

were not selected as preferred modes because they do not consistently have a large projection onto all of the stochastic optimals. In Figure 5.13b) these three modes correspond to the pairs (645,646), (648,649) and (660,661), all of which have significantly smaller projection coefficients than the 5 preferred modes.

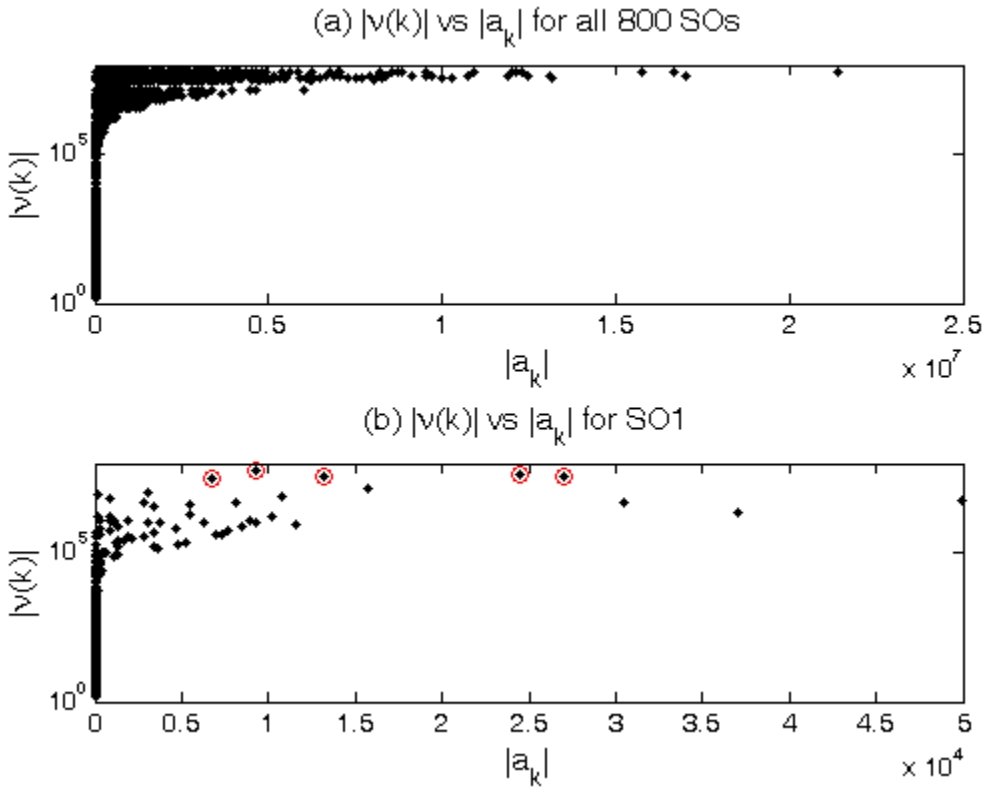

Figure 5.15. $\|v_k\|$ vs. $\|a_k\|$ for a) all 800 SOs and b) SO1. The five eigenmodes preferred by all of the stochastic optimals are circled in b).

5.4 Conclusions

This analysis leads to the following results. The stochastic perturbations associated with the first stochastic optimal (defined as the structure that leads to maximum variance of the THC) are confined to high latitudes of the Atlantic Ocean. The stochastically induced response resulting from these perturbations also occurs primarily in the North Atlantic with the temperature response penetrating to large depths and the salinity response an order of magnitude greater than the temperature response and confined to the surface. This implies that the salinity dynamics is the dominant mechanism of the response. The large stochastically induced variance of the THC is a result of transient growth of the

stochastically induced perturbations. This transient growth is due to the linear interference of the most highly nonnormal eigenmodes of the system and is the same mechanism that results in transient amplification of THC perturbations when the linear tangent model is perturbed by the optimal initial conditions found in Chapter 2. Figure 5.6 shows that the surface structure of the optimal initial conditions for temperature and salinity are very similar to the first stochastic optimal. Forcing the linearised model with noise with the spatial structure of the first stochastic optimal leads to significantly more variance than forcing with the second stochastic optimal as shown in Figure 5.7. The response is dramatically different for forcing with the spatial structure of the first and second stochastic optimals compared to forcing with spatially uncorrelated noise. Forcing with spatially uncorrelated noise produces higher frequency response than forcing with the stochastic optimals (compare Figures 5.7 to Figure 5.8).

The most nonnormal eigenmodes, which dominate the optimal transient response, are low frequency modes (Figure 5.14); this fact is consistent with the power spectrum in Figure 5.9 which shows that variance with periods greater than 10 years account for most of the power in the stochastically induced response.

The dominance of the nonnormal eigenmodes in producing and maintaining stochastically induced variance has been found to occur in studies of ENSO using models of varying complexity (Moore and Kleeman 2001, Moore et al. 2003). In a study of shear flows around obstacles Aiken et al. (2002) also showed that the most nonnormal eigenmodes of the circulation play a key role in governing the response of the system to stochastic forcing. Chhak et al. (2006b) applied the ideas of generalized stability theory to stochastic forcing of the North Atlantic wind-driven circulation. They found that the

induced perturbations from stochastic forcing with the stochastic optimals were a linear superposition of the most nonnormal eigenmodes with large amplitude. These preferred nonnormal modes were typically low frequency and they concluded that the transient growth occurred via interference of these modes as a result of differences in decay rate and/or frequency between the modes with both mechanisms being equally effective. Most of the power in the stochastically induced response of the wind driven circulation was found to be described by variance with low frequencies. Their conclusion that the shape of the power spectrum is a direct consequence of the nonnormal nature of the system is supported by the results of the present study. In this earlier study of the wind-driven circulation the structure of the stochastic forcing was generally basin wide whereas the stochastically induced response was localized to the western boundary region. In contrast the results of this study show that for the modeled THC the structure of the first stochastic optimal occurs primarily at high latitudes with the response also occurring at high latitudes.

Zanna and Tziperman (2008 in press) used a box model and generalized stability theory to study the stochastically induced response of the THC. Their conclusion that the salinity anomalies were the most efficient structures at sustaining THC variability is also a conclusion of the present study. However, there are major differences in their conclusions about the timescales of the response for forcing with the first and second stochastic optimals. They found that the variability excited by the first stochastic optimal had significantly longer time scales than the variability excited by the second stochastic optimal. This was not found to be the case with the WS model where the timescales for forcing with both the first and second stochastic optimals were similar. This difference

may be attributed to the fact that Zanna and Tziperman's model was coupled to an idealized atmosphere where the WS model used for this study is not. However, the general characteristics of the power spectrum of the stochastically induced response of the THC found in their box model study were very similar to the corresponding spectra found in the present study. The magnitudes of the salinity and temperature components of the first and second stochastic optimals were very similar in Zanna and Tziperman's model to those found in the present study, with both models characterised by a salinity component an order of magnitude larger than the temperature component. However, the stochastic optimals in the WS single hemisphere model have most of their structure at high latitudes while in the two hemisphere box model of Zanna and Tziperman's only the second stochastic optimal has most of its structure at high latitudes, (the first having basin wide structure).

Generalized stability theory can be used to identify the geographic areas that are likely to be significantly impacted by stochastic forcing. When stochastic forcing occurs in these regions increased variability of the THC can be expected. The results of this study reveal that the optimal forcing patterns of temperature and salinity anomalies that have the greatest impact on the THC are spatially coherent patterns that occur primarily at high latitudes. Optimal forcing induces low-frequency variability of the THC at high latitudes by acting as a source of continuous optimal perturbations.

Chapter 6

Wind stress

6.1 Introduction

Wind blowing over the ocean results in a transfer of energy from the atmosphere into the surface layers of the ocean. This energy is expended in generating surface gravity waves which propagate in the direction of the wind and is also transmitted downwards as a result of internal friction within the upper ocean. This internal friction comes from turbulence rather than molecular viscosity and leads to the development of wind-driven currents. The balance between the frictional forces (both internal and surface wind-stress) and the Coriolis force results in the average motion of the directly wind-driven layer of the ocean (known as the Ekman layer) being perpendicular and to the right of the direction of the wind in the Northern Hemisphere. For an ideal homogeneous infinite ocean the speed of the surface current is directly proportional to the surface wind stress. The volume of water transported in the Ekman layer is known as the Ekman transport and contributes significantly to the general ocean circulation. It is impossible to separate the wind-driven and density-driven (thermohaline) components of the oceanic circulation. Wind driving influences the sources and sinks of heat and salt for the ocean by transporting surface water from the tropics to latitudes where cooling and evaporation increases the density of the surface waters. The advection of salinity anomalies by the wind driven circulation to areas of deep-water formation may enhance or shut off the thermohaline circulation (Delworth et al. 1993, Weaver and Sarachik 1991). Another driving component of the thermohaline circulation that is affected by surface winds is the

freshwater flux. Evaporation, a negative freshwater flux, is determined by the latent heat loss which is directly proportional to the strength of surface winds.

Many studies have examined the relationship between wind stress and the THC. Winton and Sarachik (1993) found using an ocean GCM that long-term self-sustaining oscillations of the THC occur when the wind stress is turned off. Hughes and Weaver (1994) showed that by eliminating the wind stress in the Southern Ocean of their GCM deep water formation in the Southern Hemisphere ceases. Using a simple box model, Pasquero and Tziperman (2004) studied the effects of the horizontal upper-ocean wind-driven circulation (WDC) on the variability of the THC. They found that adding the WDC created self-sustained variability of the THC on interdecadal to centennial time scales. Although the WS model does not exhibit self-sustained oscillations of the THC due to wind stress forcing, Wright and Stocker (1992) found that adding wind stress significantly improved the comparison with observational estimates of the meridional heat and water fluxes. This chapter will consider the effects of surface wind stress on the nonnormal dynamics and stochastic optimals of the THC in the WS model.

6.2 Optimal initial conditions

To investigate the influences of wind stress on the nonnormal dynamics of perturbation growth of the THC a zonally averaged zonal wind stress was added to the meridional momentum equation. The meridional wind stress was not considered. A plot of the wind stress as a function of latitude is displayed in Figure 6.1a). The wind stress varies from westward in the tropical easterlies to eastward in the midlatitude westerlies. Thus the wind stress is negative at low latitudes and positive at midlatitudes. The wind stress is

again negative at high latitudes under the polar easterlies. The steady state temperature and salinity from the full nonlinear model after being run for 12,000 years under restoring boundary condition with wind stress are shown in Figures 6.1b) and 6.1d). These fields are very similar to the steady state temperature and salinity found with no wind stress, the primary difference being a slight upward bowing of the isotherms near the equator due to the Ekman fluxes. The values of the maximum linearised THC amplitude and of the optimization time for transient growth of THC perturbations were seen in Chapter 4 to be sensitive to the value of the vertical diffusivity in the absence of wind (Table 4.1). In order to generate a realistic maximum overturning streamfunction value of 10 Sv the vertical diffusivity was chosen to be $1.0\times10^{-4}m^2s^{-1}$ for the analysis of nonnormal dynamics in the absence of wind. The wind stress results in an Ekman transport which increases the maximum THC amplitude and so a smaller vertical diffusivity can be used to achieve a realistic maximum transport. To allow a direct comparison of nonnormal dynamics in the absence of wind, in the present case a vertical diffusivity of $0.4\times10^{-4}m^2s^{-1}$ was employed. This results in a maximum THC amplitude of 11.4 SV.

Figure 6.1c) shows the steady state streamfunction for the full nonlinear model. There are significant differences in the upper 1000m of the ocean between this steady state streamfunction and the steady state streamfunction for the case of no wind stress (Figure 4.1e). In this case there is equatorial upwelling, downwelling in the subtropics and upwelling in the subpolar region which brings salt to the sea surface. The present single-hemisphere model does not correctly produce the water mass structure of the Northern Hemisphere, and so the subtropical circulation cell extends to greater depths than observed. When the WS model includes both north and south hemispheres,

agreement between observed and simulated circulation and water mass structure is much better (Stocker and Wright 1991). In our study of pure thermohaline dynamics (Chapters 4 and 5), we considered a single hemisphere; in order to allow direct comparison with these earlier results, the following analysis will also focus on a single hemisphere.

Since the linearised THC amplitude (defined in Eq. 4.1) is meant to represent the net poleward flux anomaly it is defined only for the latitudes north of 20^{o}N where the net flux is northward. As a consequence of the wind-driven circulation, the linearised THC amplitude shown in Figure 6.1e) reaches its maximum value at 45^{o}N rather than at 76^{o}N (the location of the maximum in the absence of wind stress).

The optimal initial conditions were calculated for the linear tangent model with wind stress as outlined in Chapter 4. The optimal perturbation yields a maximum of THC amplification after 6 years, in agreement with the amplification timescale in the absence of wind (Chapter 4). The evolution of the optimal initial temperature and salinity conditions with wind stress are shown in Figure 6.2. The spatial evolution of the optimal initial conditions with and without wind stress are almost identical. (compare Figure 4.4 with Figure 6.2).

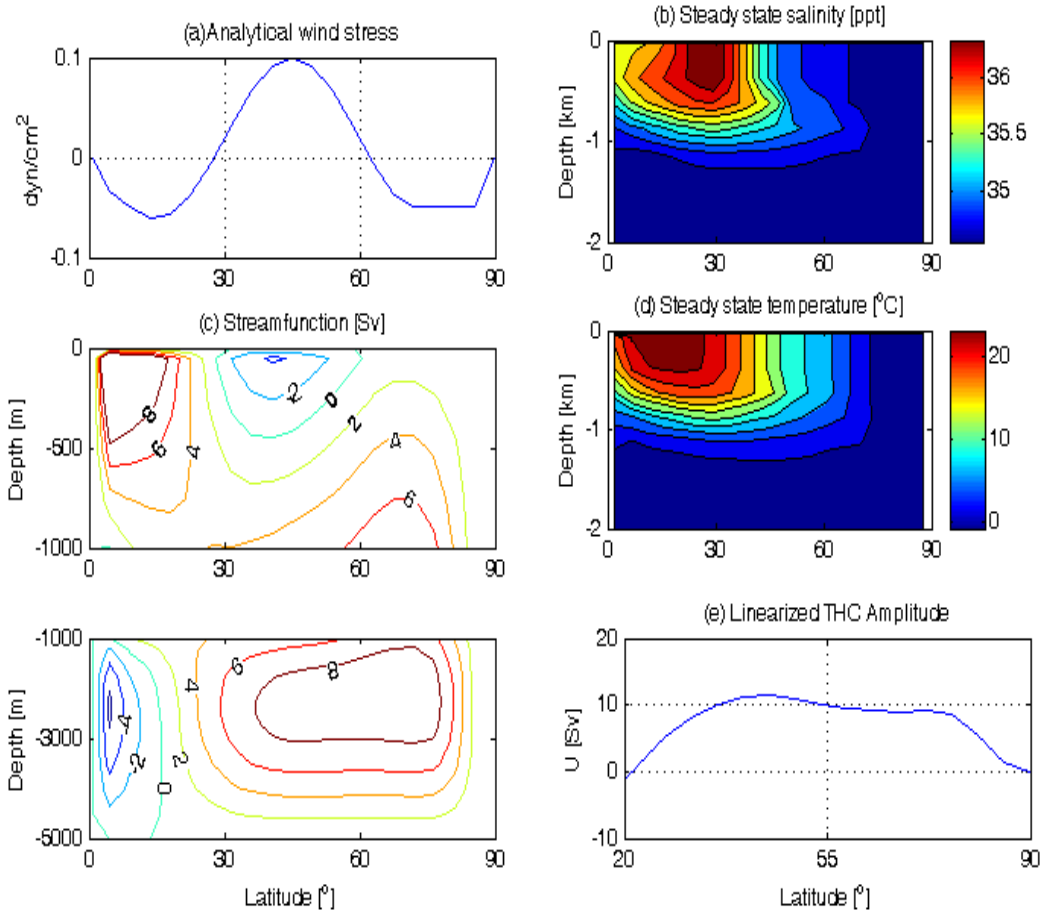

Figure 6.1. a) Analytical wind stress as a function of latitude b) steady-state salinity, c) steady state streamfunction, d) steady state temperature of the full nonlinear model with wind stress after 12,000 year spinup and e) linearised THC amplitude.

Paralleling the analysis of Chapter 4 the evolution of the linear THC anomaly and its contributions from the temperature and salinity as a function of latitude and time are shown in Figures 6.3 and 6.4. Once again the differences between the model run with and without wind stress are negligible.

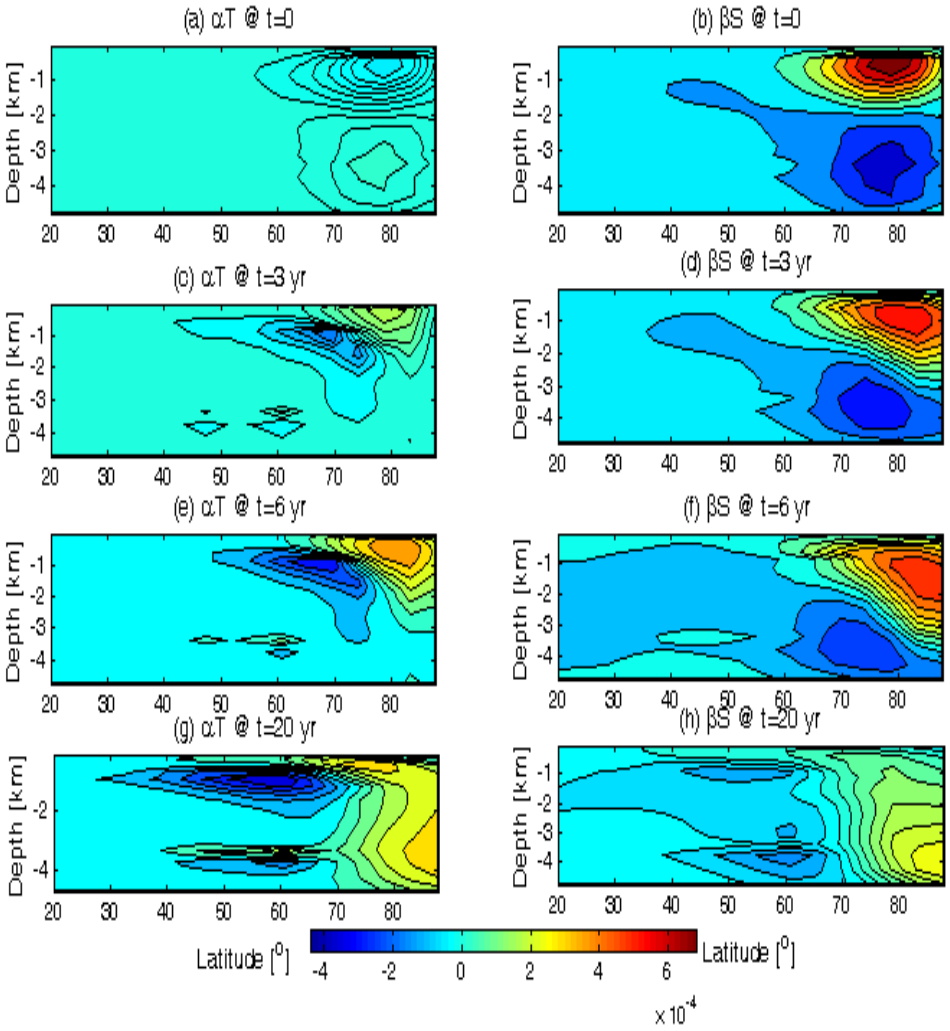

Figure 6.2. (a) Optimal initial temperature perturbation (αT) and (b) optimal initial salinity perturbation (βS) calculated from the linearised model equations with wind stress that maximize the transient amplification of the THC for τ = 6 years. (c) to (h) αT and βS perturbations at 3 yr, 6 yr and 20 yrs.

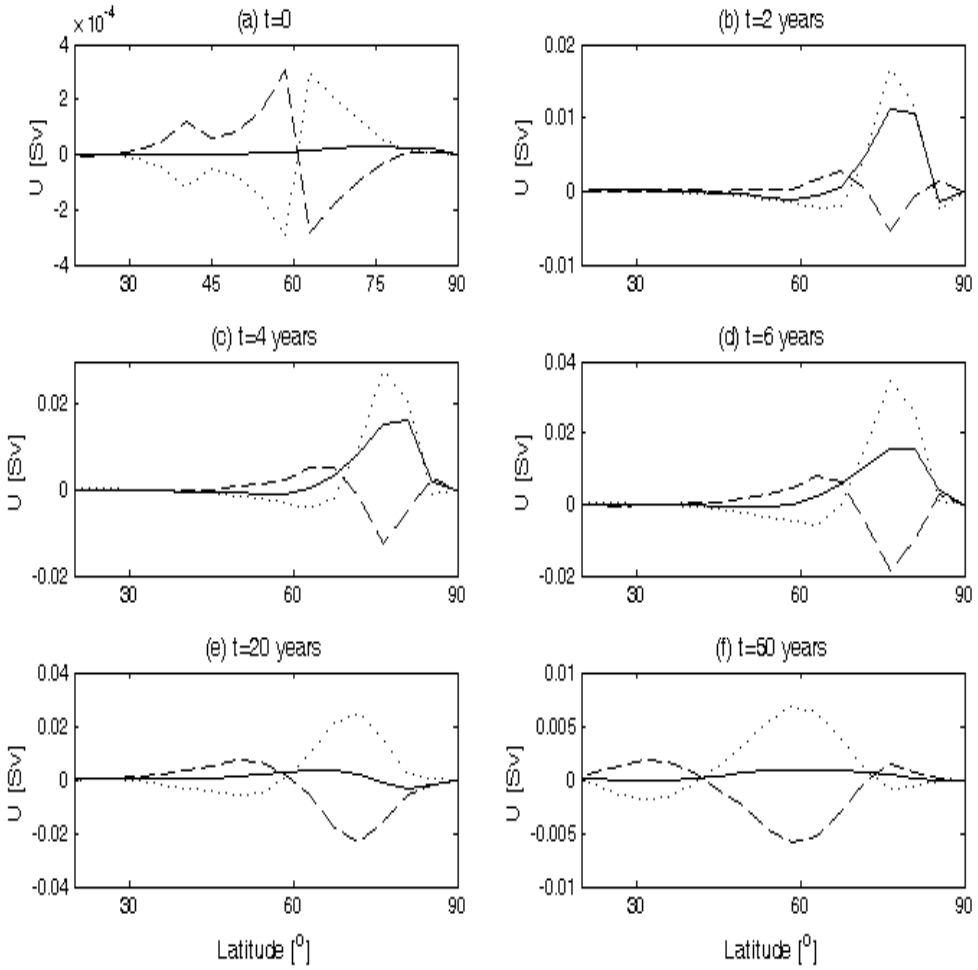

Figure 6.3. Evolution of the linear THC anomaly (solid line) and its contributions from the temperature (dashed line) and salinity (dotted line) as a function of latitude calculated from the linearised model equations with wind stress starting from the optimal initial conditions that maximize the transient amplification of the THC anomaly for τ = 6 years. (a) t=0, (b) t=2 years, (c) t=4 years, (d) t=6 years, (e) t=20 years and (f) t=50 years. (Note that the scaling for each plot is different and the maximum amplification occurs at t=6 years).

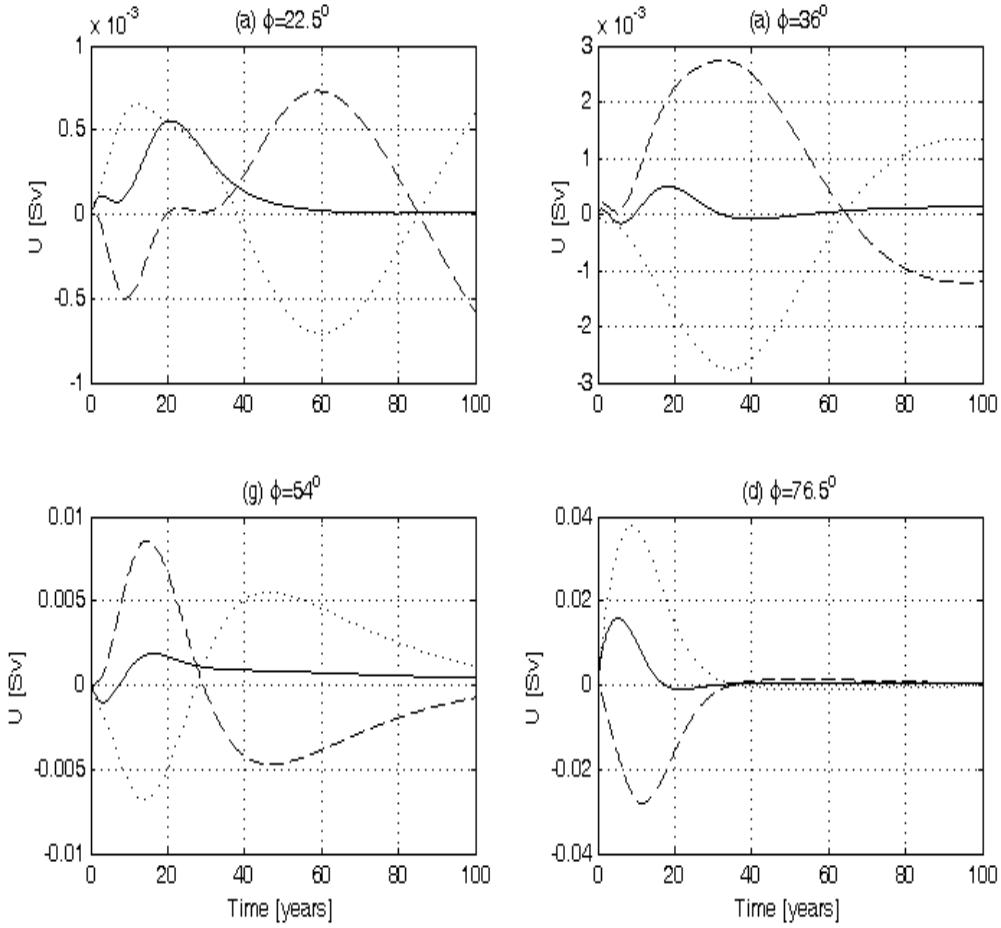

Figure 6.4. Evolution of the linear THC anomaly (solid line) and its contributions from the temperature (dashed line) and salinity (dotted line) as a function of time calculated from the linearised model equations with wind stress starting from the optimal initial conditions that maximize the transient amplification of the THC anomaly for $\tau = 6$ years. (a)$\varphi=22.5^o$, (b) $\varphi=36^o$, (c) $\varphi=54^o$ and (d) $\varphi=76.5^o$.(Note that the scaling of each plot is different and the maximum amplification occurs at 76.5^o)

Although the nonnormal dynamics of the linear model do not seem to be affected by the presence of wind stress the nonlinear model does show differences when wind stress is added. Figure 6.5 shows the evolution of the THC anomaly calculated from the full nonlinear model and linearised model both with wind stress. It can be seen by comparing the nonlinear evolution in this Figure 6.5 to that in Figure 4.8 that the THC

perturbation decays much more rapidly when wind stress is added to the nonlinear model. For perturbations of the same magnitude, the model including wind forcing displays considerably larger differences between the linearised and the fully nonlinear dynamics than the model without wind forcing. Evidently, wind forcing increases the importance of nonlinear processes to the dynamics of the THC (at least in this model).

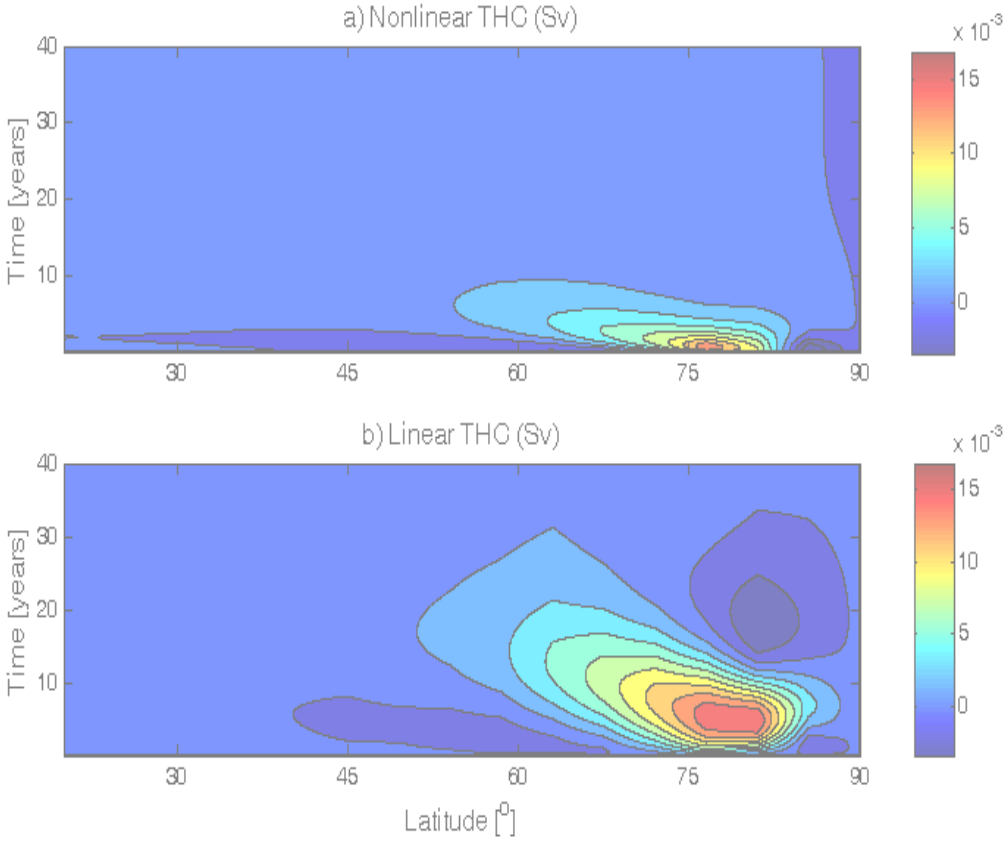

Figure 6.5. (a) THC anomaly calculated from the full nonlinear model with wind stress and (b) THC anomaly calculated from the linearised model equations with wind stress starting from the optimal initial conditions that maximize the transient amplification of the THC anomaly for τ=6 years

As noted above, to allow a direct comparison of non-normal dynamics in the absence of wind, in the wind forced-case a vertical diffusivity $K_v = 0.4 \times 10^{-4} m^2 s^{-1}$ was

employed. This results in a maximum THC amplitude of 11.4 Sv and an optimization time of 6 years, in agreement with the values found in the case of pure thermohaline circulation. The optimization time is not as sensitive to changes in the vertical diffusivity when wind stress is added to the model equations. For example, when the vertical diffusivity was changed from $K_v = 0.4 \times 10^{-4} m^2 s^{-1}$ to $K_v = 0.8 \times 10^{-4} m^2 s^{-1}$ in the absence of wind the optimization time changed from 11 years to 7 years (see Table 4.1) whereas this same change in vertical diffusivity in the presence of wind led to a change in the optimization time from 6 years to only 4.5 years.

6.3 Stochastic optimals

The first two stochastic optimals for the linearised model with wind stress are shown in Figure 6.6 along with the surface optimal initial conditions. As expected the temperature and salinity components of the first stochastic optimal (Figure 6.6a and c) have very similar structures to the optimal initial conditions but the second stochastic optimals (Figures 6.6 b and d) show much more low latitude structure when wind stress is included. This reflects the changes that occur in the streamfunction at low latitudes due to negative wind stress forcing in that region. Interestingly, this effect appears only as a slight increase in the temperature and decrease in the salinity components of the first stochastic optimal but as fairly large features in the second stochastic optimal. In the absence of wind stress the first and second stochastic optimals accounted for 8% and 4.5% of the variance respectively whereas in this case of including wind stress the first and second stochastic optimals account for 12% and 7% respectively. In the presence of

wind forcing, the sensitivity of the model to low-latitude forcing is substantially stronger than in the absence of wind forcing.

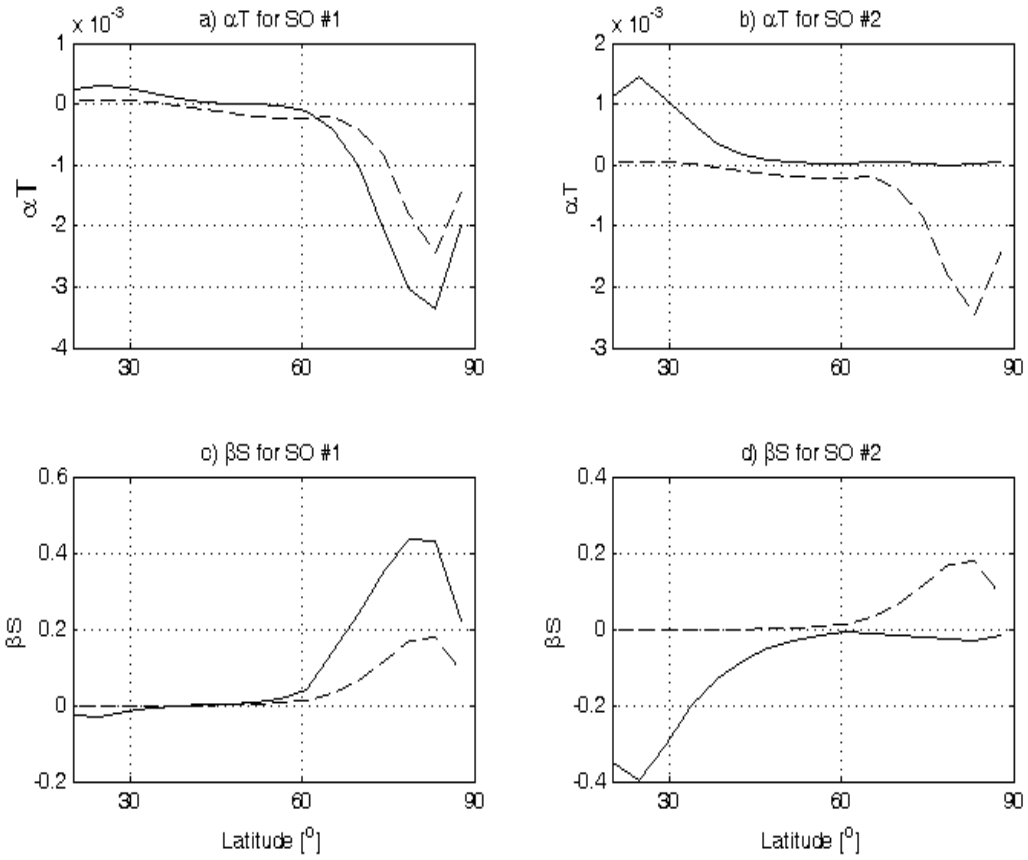

Figure 6.6. a) αT for SO1 (solid line), b) αT for SO2 (solid line), c) βS for SO1 (solid line) and d) βS for SO2 (solid line) for the model with wind stress. Also shown in each plot as dashed lines are the corresponding values for the surface component of the optimal initial conditions, P0

Time series of the norm ΣU^2 for the model with wind stress forced with SO1, SO2, and spatially uncorrelated forcing are shown in Figure 6.7. There is no essential difference between this response and the response from the model without wind stress. As found earlier, the variance from forcing with the second stochastic optimal is

significantly less than that from the first and the salinity component consistently dominates the response.

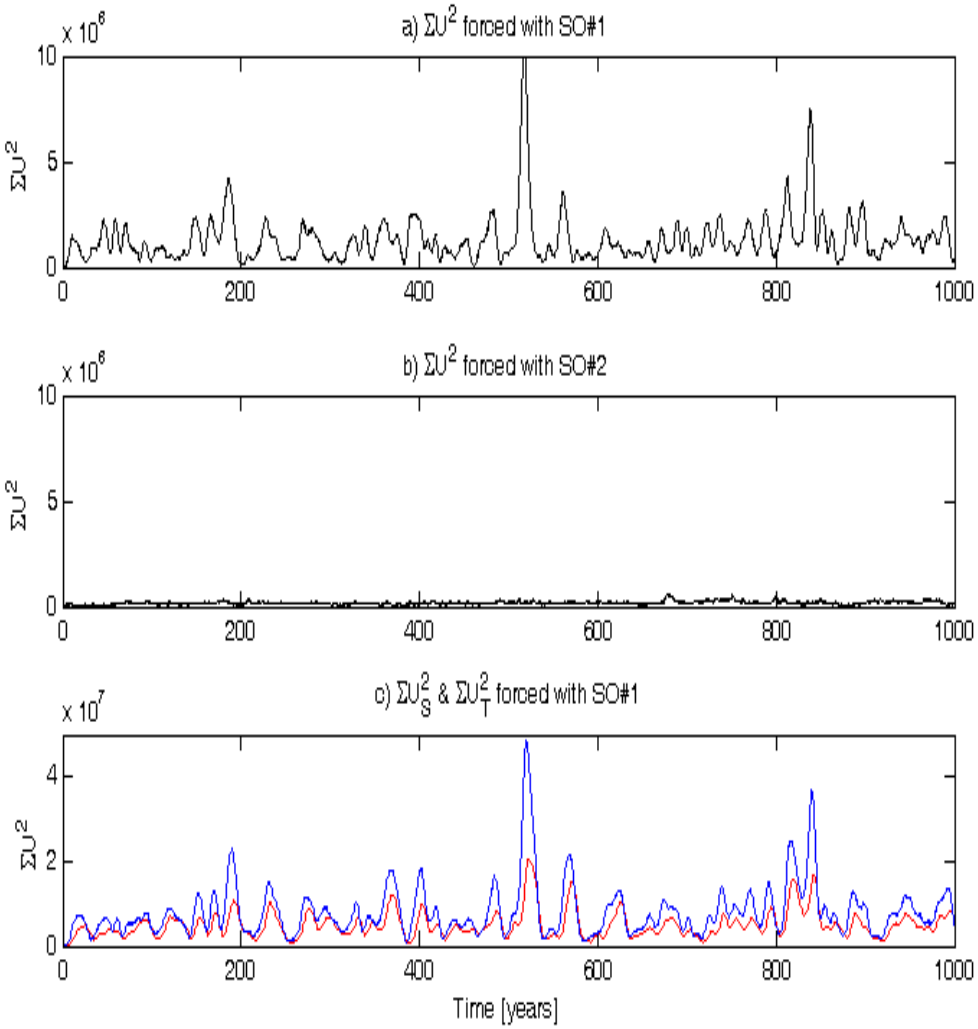

Figure 6.7.a) Time series of the norm ΣU^2 when the linear model with wind stress is forced with SO1, b) time series of the norm ΣU^2 when the linear model with wind stress is forced with SO2 and c) time series of the temperature (red line) and salinity (blue line) components of the norm when the linear model with wind stress is forced with SO1.

The first EOFs for the response of the model with wind stress when forced with SO1 and SO2 are shown in Figure 6.8. The salinity EOFs account for 52% and 51%

respectively of the induced salinity variance when forcing is from SO1 and SO2 respectively, while the temperature EOFs account respectively for 42% and 38% of the temperature variance SO1 and SO2 respectively. These values when wind stress is considered are very similar to the values without wind stress. The response for forcing with SO1 is very similar with and without wind however the response to SO2 is quite different when wind stress is considered. EOF1 in response to forcing with SO1 shows predominant structure at high latitudes, trapped near the surface for salinity but extending to depth for temperature. In contrast, EOF1 in response to forcing with SO2 displays strongest structure at low latitudes and penetrates much less to depth than EOF1 in response to forcing by SO1. This low-latitude response is consistent with the stronger values taken by second stochastic optimal at low latitudes, as described above.

6.4 Conclusions

Overall the results of the generalized stability analysis for the model that includes wind stress are very similar to the results for the model that does not include wind stress. The optimal initial conditions for both models are almost identical as are the evolutions of the THC perturbation amplitudes. The first stochastic optimal for both models have

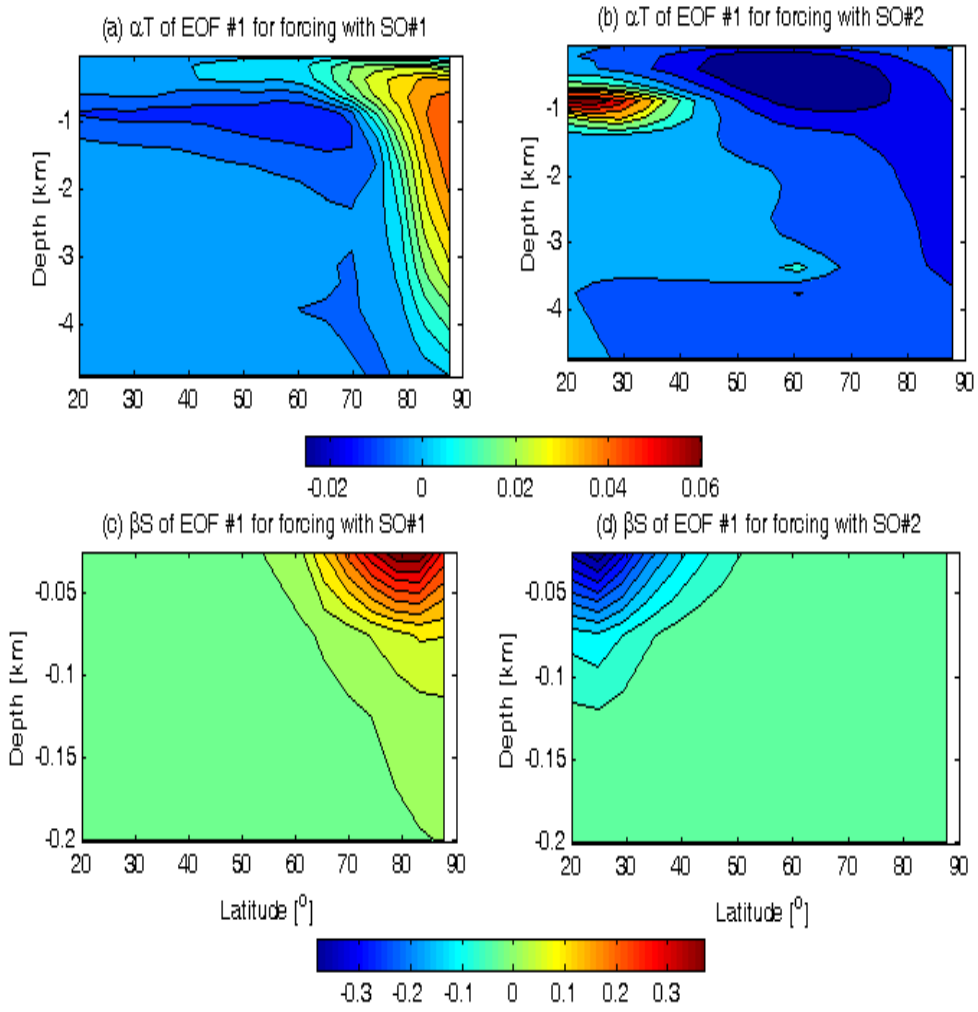

Figure 6.8. The first EOF of the response of the temperature and salinity of the linearised model with wind stress forced with the first and second stochastic optimals. a) αT of EOF 1 for forcing with SO 1, b) αT of EOF 1 for forcing with SO 2, c)βS of EOF 1 for forcing with SO 1 and d) βS of EOF 1 for forcing with SO 2. Note that the maximum depth in c) and d) is 200m.

similar structure and the response to stochastic forcing is also the same in both cases. There are some differences between the two simulations. In particular, the presence of wind forcing appears to make the model "more nonlinear", in the sense that there is a greater disagreement between the nonlinear and linearised evolutions of perturbations in the presence of wind forcing than in its absence.

By expressing the tangent linear equation of their coupled ocean-atmosphere system in terms of the physical processes that rendered the propagator nonnormal, Moore and Kleeman (1999) identified the surface perturbation wind stress in the tropics as being one of these processes. They argued that any physical mechanism that operates in only one direction renders the coupled system nonnormal. For example, the surface wind stress will drive ocean currents but ocean currents will not drive wind. Since the WS model used in this study is not coupled to an atmosphere this argument does not apply here. In the absence of this coupling, the results of this study indicate that the nonlinear dynamics and the mechanisms of transient growth of perturbations are independent of the wind stress term in the model equations.

Chapter 7

Conclusions

This study has investigated the amplification of THC anomalies and the response to stochastic forcing in the WS 2D zonally averaged ocean model due to nonnormal dynamics. The tangent linear matrix was obtained by perturbing the steady state temperature and salinity fields that resulted from running the full nonlinear WS model for 12,000 years under restoring boundary conditions. The ideas of generalized stability theory were then applied to the tangent linear WS model. Although the linear dynamics were stable, it was found that as a result of the nonnormal dynamics, significant growth of THC anomalies occurred due to the linear interference of nonorthogonal eigenmodes. The initial perturbations of the temperature and salinity fields that lead to maximum amplification of the THC anomalies, known as the optimal initial conditions, were dominated by high latitude surface anomalies, but also involved anomalies at depth. While salinity and temperature contributions to the overturning strength initially canceled out, as the optimal perturbation grew the salinity contribution dominated the response. Maximum transient amplification of the overturning strength was found to occur on sub-decadal timescales (although this timescale was sensitive to model parameters), and temperature and salinity perturbations persisted for decades after the THC perturbation had decayed. It was found that a small subset of the most nonnormal eigenmodes of the linearised system were responsible for the amplification process.

In addition, the techniques of generalized stability theory were used to calculate the patterns of stochastic surface forcing that resulted in maximum variance of the THC.

It was found that the first stochastic optimal had a structure very similar to the surface component of the optimal initial conditions. The stochastically induced response to forcing with the pattern of the first stochastic optimal was shown to result in significantly more variance of the THC than forcing from either the second stochastic optimal or spatially uncorrelated noise (with the same forcing amplitude). It was found that the most nonnormal low frequency eigenmodes dominated the stochastically induced response which occurred primarily at high latitudes. This analysis demonstrated that while both temperature and salinity perturbations contributed to variability of the overturning strength, the response was dominated by salinity fluctuations. While it is difficult to compare the results of this study to the real ocean because of the coarse resolution of the model and the lack of actual data the results of this study have demonstrated that those aspects of THC dynamics represented by the zonally-averaged WS model are particularly sensitive to high latitude temperature and salinity perturbations.

Finally, it was shown that the addition of wind stress did not have a large impact on the nonnormal dynamics of the linearised system. Adding wind allowed the value of the vertical diffusivity to be reduced to achieve the same maximum linearised THC amplitude as was used in the case with no wind stress.

Although the seasonal cycle and sea ice were not included in the 2D zonally averaged model it was shown to produce the latitude-depth structure of the steady state temperature, salinity and THC that compared reasonably well with observations. The advantage of a reduced complexity model such as the one used in this study is that is gives satisfactory results for the large scale flow and is suitable for long (1000 year) integrations.

This study has taken advantage of the separation in time scales between atmospheric forcing and oceanic response to represent atmospheric fluctuations as white noise. The ocean's response to this high frequency stochastic forcing was dominated by the optimal spatial patterns of forcing which acted as a source of continuous optimal perturbations. The mechanism of linear interference of nonnormal eigenmodes of the linearised system explained why the observed frequency spectrum of the response was broadly red and not strongly peaked at the frequencies of a weakly damped eigenmode. The mechanism of transient growth described in this study is predictable over a finite time interval. It was shown that when an optimal perturbation was used as the initial condition THC anomalies grew on a well defined timescale. This is an important step in trying to understand the variability of the THC and the coupling between the ocean-atmosphere general circulation and in developing the ability to predict climate change. Knowledge of the critical patterns of atmospheric forcing which lead to enhanced variability is necessary in order to effectively monitor, model, and study the coupled ocean-atmosphere climate.

Understanding the stability and variability of the THC is of importance because of the possibility of large and abrupt changes in the climate associated with the THC. Most previous studies of mechanisms of forced THC variability have focused on the eigenstructure of the linearised operator. Such linear eigenmode analyses are only useful as a first approximation to the nonlinear resonant response of a dynamical system to forcing. This study has shown that generalized linear stability can be used to characterise rich behavior in the linearised dynamics of the THC. In the future it would useful to repeat the analysis preformed in this study using more complex models which may

include multiple hemispheres, multiple basins, atmospheric coupling or sea ice to investigate further the physical mechanisms that lead to transient growth of perturbations of the THC. This study suggests that nonnormal THC dynamics should be seriously considered in studies of the stability and variability of the THC.

Bibliography

Aeberhardt, M., M. Blatter, and T. F. Stocker, 2000: Variability on the century time scale and regime changes in a stochastically forced zonally averaged ocean-atmosphere model. *Geophys. Res. Lett.*, **27**, 1303-1306.

Aiken, C. M., A. M. Moore, and J. H. Middleton, 2002: The nonnormality of coastal ocean flows around obstacles, and their response to stochastic forcing. *J. Phys. Oceanogr.,* **32**, 2955-2974.

Alexander, J., and A. H. Monahan, 2008: Nonnormal perturbation growth of pure thermohaline circulation using a 2-D zonally averaged model. *J. Phys. Oceanogr*., (in press).

Bentsen, M., H, Drange, T. Furevik, and T. Zhou, 2004: Simulated variability of the Atlantic meridional overturning circulation. *Climate Dynamics,* **22**, 701-720.

Broecker, W. S., 1997: Thermohaline circulation, the achilles heel of our climate system: Will man-made CO_2 upset the current balance. *Science,* **278**, 1582-1588.

Buizza, R., and T.N. Palmer, 1995: The singular-vector structure of the atmosphere global circulation. *J. Atmos. Sci*., **52**, 1434-1456.

Butler, K. M., and B. F. Farrell, 1992: Three-dimensional optimal perturbations in viscous shear flow. *Phys. Fluids*, **4**(8), 1637-1651.

Capotondi, A., and W. Holland, 1997: Decadal variability in an idealized ocean model and its sensitivity to surface boundary conditions. *J. Phys. Oceanogr.*, **27**, 1072-1093.

Cessi, P., 1994: A simple box model of stochastically forced thermohaline flow. *J. Phys. Oceanogr.* **24**, 1911-1920.

Chen, F., and M. Ghil, 1995: Interdecadal variability of the thermohaline circulation and high-latitudes surface fluxes. *J. Phys. Oceanogr*, **27**, 1072-1093.

Chhak, K. C., A. M. Moore, R. F., Milliff, G. Branstator, W. R. Holland, and M. Fisher, 2006a: Stochastic forcing of the North Atlantic wind-driven ocean circulation. Part I: A diagnostic analysis of the ocean response to stochastic forcing. *J. Phys. Oceanogr.*, **36**(3), 300-315.

Chhak, K. C., A. M. Moore, R. F., Milliff, G. Branstator, W. R. Holland, and M. Fisher, 2006b: Stochastic forcing of the North Atlantic wind-driven ocean circulation. Part II: An analysis of the dynamical ocean response using generalized stability theory. *J. Phys. Oceanogr.*, **36**(3), 316-334.

Clark, P. U., N. G. Pisias, and T. F. Stocker, 2002: The role of the thermohaline circulation in abrupt climate change. *Nature*, **415**, 863-869.

Cunningham, S. A., T. Kanzow, D. Rayner, D., M. O. Baringer, W. E. Johns, J. Marotzke, H. R. Longwirth, E. M. Grant, J. J. Hirschi, L. M. Beal, C. S. Meinen, and H. L. Bryden, 2007: Temporal variability of the Atlantic Meridional Overturning Circulation at 26^{o} N. *Science*, **317**, 935-938. (doi:10.1126/science.1141304.)

DelSole, T., and B. F. Farrell, 1995: A stochastically excited linear system as a model for quasigeostrophic turbulence: Analytic results for one and two layer fluids. *J. Atmos. Sci.,* **52(14),** 2531-2547.

DelSole, T.M., 1996: Can quasigeostrophic turbulence be modeled stochastically? *J. Atmos. Sc*i., **53**, 1617-1633.

DelSole, T.M., 1999: Stochastic models of shear-flow turbulence with enstrophy transfer to subgrid scales. J. Atmos. Sci., 56, 3692-3703.

DelSole, T.M., and A.Y. Hou, 1999: Empirical stochastic models for the dominant climate statistics of a general circulation model. *Mon Wea. Rev*., **127**, 2533-2545.

Delworth, T. L., and R. J. Greatbatch, 2000: Multidecadal thc variability driven by atmospheric surface flux forcing. *J. Climate*, **13**, 1481-1494.

Delworth, T., S. Manabe, and R. Stouffer, 1993: Interdecadal variations of the thermohaline circulation in a coupled ocean-atmosphere model. *J. Climate,* **6**, 1993-2011.

Dong, B. and R. T. Sutton, 2005: Mechanism of interdecadal thc variability in a coupled ocean-atmosphere GCM. *J. Climate*, **18**, 1117-1135.

Errico, R.M., T. Vukicecic, and K. Raeder, 1993: Examination of the accuracy of a tangent linear model. *Tellus*, **45A**, 462-477.

Fanning, A., and A. Weaver, 1998: Mechanism of interdecadal thc variability in a coupled ocean-atmosphere GCM. *J. Climate,* **11**, 709-715.

Farrell, B.F., 1982a: The initial growth of disturbances in baroclinic flow. *J. Atmos. Sci*., **39**, 1663-1686.

Farrell, B.F., 1982b: Pulse asymptotics of the Charney baroclinic instability problem. *J. Atmos. Sci*., **39**, 507-517.

Farrell, B.F., 1984: Modal and nonmodal baroclinic waves. *J. Atmos. Sci*., **41**, 668-673.

Farrell, B.F., 1985: Transient growth of damped baroclinic waves. *J. Atmos. Sci*., **42**, 2718-2727.

Farrell, B.F., 1988: Optimal excitation of neutral Rossby waves, *J. Atmos. Sci.,* **45**, 163-172.

Farrell, B.F., 1989: Optimal excitation of baroclinic waves. *J. Atmos. Sci*., **46**, 1193-1206.

Farrell, B.F., 1990: Small error dynamics and the predictability of atmospheric flows. *J. Atmos. Sci*., **47**, 2409-2416.

Farrell, B.F., and P.J. Ioannou, 1993d: Stochastic dynamics of baroclinic waves. *J. Atmos. Sci*., **50**, 4044-4057.

Farrell, B. F., and P. J. Ioannou, 1993a: Stochastic dynamics of baroclinic waves. *J. Atmos. Sci.,* **50(24)**, 4044-4057.

Farrell, B. F., and P. J. Ioannou, 1993b: Stochastic forcing of perturbation variance in unbounded shear and deformation flows. *J. Atmos. Sci.,* **50(2)**, 200-211.

Farrell, B. F., and P. J. Ioannou, 1995: Stochastic dynamics of the midlatitude atmospheric jet. *J. Atmos. Sci.,* **52(10)**, 1642-1656.

Farrell, B. F., and P. J. Ioannou, 1996: Generalized stability theory. Part I: autonomous operators. *J. Atmos. Sci.,* **53**(14), 2025-2040.

Ferranti, L., T.N. Palmer, F. Molteni, and E. Klinker, 1990: Tropical-extratropical interaction with the 30=60 day oscillation and its impact of medium and extended range prediction. *J. Atmos. Sci*., **47**, 2177-2199.

Ganachaud, A., and C. Wunsch, 2000: Improved estimates of global ocean circulation, heat transport and mixing from hydrographic data. *Nature,* **408(6811)**, 453-457.

Griffies, S. M., and E. Tziperman, 1995: A linear thermohaline oscillator driven by stochastic atmospheric forcing. J. Climate, **8**, 2440-2453.

Hasselmann, K., 1976: Stochastic climate models Part I. Theory, Tellus, **28**, 473-484.

Herbaut, C., J. Sirven, and S. Fevrier, 2002: Response of a simplified oceanic general circulation model to idealized NAO-like stochastic forcing. *J. Phys. Oceanogr*., **32**, 3182-3192.

Hirschi, J., and T. F. Stocker, 2002: Rapid changes of the oceanic circulation in a hierarchy of ocean models. *Tellus A*, **54A**, 273-287.

Holland, M. M., C. M. Bitz, and A. J. Weaver, 2001: The role of ice-ocean interactions in the variability of the north Atlantic thc. *J. Climate*, **14**(5), 656-675.

Huck, T., A. C. de Verdiere, and A. J. Weaver, 1999: Interdecadal variability of the thc in box-ocean models forced by fixed surface fluxes. *J. Phys. Oceanogr.*, **29**, 865-892.

Huck, T., and G. K. Vallis, 2001: Linear stability of the three-dimensional thermally-driven ocean circulation: application to interdecadal oscillations. *Tellus A,* **53A**, 526-545.

Ioannou, P. J., 1995: Nonnormality increases variance. *J. Atmos. Sci.*,**52**(8), 1155-1158.

Kleeman, R., and A. M. Moore, 1997: A theory for the limitation of ENSO predictability due to stochastic atmospheric transients. *J. Atmos. Sci.,* **54**, 753-767.

Kleeman, R., and A. M. Moore, 1999: A new method for determining the reliability of dynamical ENSO predictions. *Mon. Wea. Rev*., **127**, 694-705.

Knutti, R., and T. F. Stocker, 2002: Limited predictability of the future thermohaline circulation close to an instability threshold. *J. Climate,* **15**, 179-186.

Knutti, R., T. F. Stocker, and D. G. Wright, 2000: The effects of subgrid-scale parameterizations in a zonally averaged ocean model. *J. Phys. Oceanogr.,* **30**, 2738-2752.

Kravtsov, S., and M. Ghil, 2004: Interdecadal variability in a hybrid coupled ocean-atmosphere-sea ice model. *J. Phys. Oceanogr.*, **34**, 1756-1775.

Kuhlbrodt, T., A. Griesel, M. Montoya, A. Levermann, M. Hofmann, and S. Rahmstorf, 2007: On the driving processes of the Atlantic meridional overturning circulation. *Rev. Geophys*. **45**, RG2001. (DOI:10.1029/2004RG000166.)

Lacarra, J.-F., and O. Talagrand, 1988: Short-range evolution of small perturbations in a barotropic model. *Tellus*, **40A**, 81-95.

Levermann, A., A. Griesel, M. Hofmann, M. Montoya, and S. Rahmstorf, 2005: Dynamic sea level changes following changes in the thermohaline circulation, *Clim. Dyn.*, **24**, 347-354.

Levitus, S., 1982: Climatological atlas of the world ocean. *NOAA Prof. Paper,* **13**, 173 pp.

Lohmann, B., and J. Schneider, 1999: Dynamics and predictability of Stommel's box model. A phase-space perspective with implications for decadal climate variability. *Tellus,* **51A**, 326-336.

Lorenz, E.N., 1965: A study of the predictability of a 28-variable atmospheric model. *Tellus*, **17**, 231-333.

Manabe, S., and R. J. Stouffer, 1999: Are two modes of thermohaline circulation stable? *Tellus,* **51A(3)**, 400-411.

Marsh, R., 2000: Recent variability of the north atlantic thc inferred from surface heat and freshwater fluxes. *J. Climate*, **13**(18), 3239-3260.

McManus, J., R. Francois, J. M. Gherardi, L. D. Keigwin, and S. Brown-Leger, 2004: Collapse and rapid resumption of Atlantic meridional circulation linked to deglacial climate changes. *Nature,* **428**, 834-837.

Meehl, G. A., T. F. Stocker, W. D. Collins, P. Friedlingstein, A. T. Gaye, J. M. Gregory, A. Kitoh, R. Knutti, J. M. Murphy, A. Noda, S. C. B. Raper, I. G. Watterson, A. J. Weaver and Z. C. Zhao, 2007: Global Climate Change Projections. In *Climate Change 2007: The Physical Science Basis. Contribution of Working Group I to the Fourth Assessment Report of the Intergovernmental Panel on Climate Change,* S. Solomon, D. Qin, M. Manning, Z.Chen, M. Marquis, K.B. Averyt, M. Tignor, and H.L. Miller, Eds., Cambridge University Press, Cambridge, U.K., 747-846.

Mikolajewicz, U., and E. Maier-Reimer, 1990: Internal secular variability in an ocean general circulation model. *Climate Dynamics*, **4**, 145-156.

Monahan, A. H., J. Alexander, and A. J. Weaver, 2008: Stochastic models of the meridional overturning circulation: timescales and patterns of variability. *Phil. Trans. A*, **366**, 2527-2544.

Moore, A.M., and R. Kleeman, 1996: The dynamics of error growth and predictability in a coupled model of ENSO. *Quart. J. Roy. Meteor. Soc*., **122**, 1405-1446.

Moore, A.M., and R. Kleeman, 1997a: The singular vectors of a coupled ocean-atmosphere model of ENSO. Part I: Thermodynamics, energetics and error growth. *Quart. J. Roy. Meteor. Soc*., **123**, 953-981.

Moore, A.M., and R. Kleeman, 1997b: The singular vectors of a coupled ocean-atmosphere model of ENSO. Part II: Sensitivity studies and dynamical significance. *Quart. J. Roy. Meteor. Soc*., 123, 983-1006.

Moore, A. M., and R. Kleeman, 1999: The nonnormal nature of El Nino and intraseasonal variability. *J. Climate*, **12**, 2965-2982.

Moore, A.M., and R. Kleeman, 1999b: Stochastic forcing of ENSO by the intraseasonal oscillation. *J. Climate*, **12**, 1199-1220.

Moore, A.M., and R. Kleeman, 2001: The differences between the optimal perturbations of coupled models of ENSO. *J. Climate*, **14**, 138-163.

Moore, A. M., Cristina L. Perez, and Javier Zavala-Garay, 2002: A non-normal view of the wind-driven ocean circulation. *J. Phys. Oceanogr.,* **32,** 2681-2705**.**

Moore, A. M., J. Vialard, A. T. Weaver, D. L. T. Anderson, R. Kleeman, and J. R. Johnson, 2003: The role of air-sea interaction in controlling the optimal perturbations of low-frequency tropical coupled ocean-atmosphere modes. *J. Climate,* **16**, 951-968.

Mureau, R., F. Molteni, and T.N. Palmer, 1993: Ensemble prediction using dynamically conditioned perturbations. *Quart. J. Roy. Meteor. Soc*., **119**, 299-323.

Mysak, L., T. F. Stocker, and F. Huang, 1993: Century-scale variability in a randomly forced, two-dimensional thermohaline ocean circulation model. *Climate Dynamics.* **8**, 103-116.

O'Hare, G., A. Johnson, and R. Pope, 2005: Current shifts in abrupt climate change: The stability of the North Atlantic conveyor and its influence on future climate. *Geography*, **90(3)**, 250-266.

Pasquero, C., and E. Tziperman, 2004: Effects of a wind-driven gyre on thermohaline circulation variability. *J. Phys. Oceanogr.,* **34**, 805-816.

Pedlosky, J., 1987: *Geophysical Fluid Dynamics*. Springer-Verlag, New York, 624 pp.

Penland, C., 1989: Random Forcing and forecasting using principal oscillation pattern analysis. *Mon. Wea. Rev.,* **117**, 2165-2185.

Penland, C., and P.D. Sardeshmukh, 1995a: Error and sensitivity analysis of geophysical eigensystems. *J. Climate*, **8**, 1988-1998.

Penland, C., and P.D. Sardeshmukh, 1995b: The optimal growth of tropical sea surface temperature anomalies. *J. Climate*, **8**, 1999-2024.

Penland, C., 1996: A stochastic model of IndoPacific sea surface temperature anomalies. *Physica D*, **98**. 534-558.

Pierce, D. W., T. P. Barnett, and U. Mikolajewicz, 1995: Competing roles of heat and freshwater flux in forcing thermohaline oscillations. *J. Phys. Oceanogr.*, **23**, 2046-2064.

Rahmstorf, S., 2002: Ocean circulation and climate during the past 120,000 years. *Nature*, **419**, 207-214.

Saravanan, R., and J. C. McWilliams, 1997: Stochasticity and spatial resonance in interdecadal climate fluctuations. *J.Climate*, **10**, 2299-2320.

Saravanan, R., G. Danabasoglu, S. Doney, and J. C. McWilliams, 2000: Decadal variability and predictability in the midlatitude ocean-atmosphere system. *J. Climate*, **13**, 1073-1097.

Schmidt, G., and L. Mysak, 1996: The stability of a zonally averaged thermohaline circulation model. *Tellus A,* **48A**, 158-178.

Schmittner, A., 2005: Decline of the marine ecosystem caused by a reduction in the Atlantic overturning circulation, *Nature,* **434**, 628-633.

Schmittner, A. and A. J. Weaver, 2001: Dependence of multiple climate states on ocean mixing parameters. *Geophys. Res. Let*., **28,** 1027-1030.

Schmittner, A., and T. F. Stocker, 1999: The stability of the thermohaline circulation in global warming experiments. *J. Climate,* **12**, 1117-1133.

Schmittner, A., and T. F. Stocker, 2001: A seasonally forced ocean-atmosphere model for paleoclimate studies. *J. Climate,* **14**, 1055-1068.

Sevellec, F., M. B. Jelloul, and T. Huck, 2007: Optimal surface salinity perturbations influencing the thermohaline circulation. *J. Phys. Oceanogr.,* **37**, 2789-2808.

Spall, M. A. 1993: Variability of sea surface salinity in stochastically forced systems. *Climate Dynamics*, **8**, 151-160.

Stocker, T. F., and D. G. Wright, 1991: Rapid transitions of the ocean's deep circulation induced by changes in surface water fluxes. *Nature*, **351**, 729-732.

Stocker, T. F., and D. G. Wright, 1996: Rapid changes in ocean circulation and atmospheric radiocarbon. *Paleoceanography,* **11 (6)**, 773-795.

Stocker, T. F., D. G. Wright, and L. A. Mysak, 1992b: A zonally averaged, coupled ocean-atmosphere model for paleoclimate studies. *J. Climate,* **5**, 773-797.

Stocker, T. F., D. G. Wright, and W. S. Broecker, 1992a: The influence of high-latitude surface forcing on the global thermohaline circulation. *Paleoceanography,* **7(5)**, 529-541.

Stocker, T. F., W. S. Broecker, and D. G. Wright, 1994: Carbon uptake experiments with a zonally-averaged global ocean circulation model. *Tellus,* **46B**, 103-122.

Stommel, H., 1961: Thermohaline convection with two stable regimes of flow. *Tellus,* **13**, 224-230.

Timmermann, A., M. Latif, R. Voss, and A. Grotzner, 1998: Northern hemispheric interdecadal variability: a coupled air-sea model. *J. Climate*, **11**, 1906-1931.

Timmermann, A., S. I. An, U. Krebs, and H. Goose, 2005: ENSO suppression due to weakening of the North Atlantic thermohaline circulation. *J. Climate*, **18**, 2842-2859.

Trefethen, L. N., 1997: Pseudospectra of linear operators. *SIAM Rev*., **39**, 383-406.

Trefethen, Lloyd N., and Mark Embree, 2005: *Spectra and pseudospectra: the behavior of nonnormal matrices and operators*. Princeton University Press, New Jersey, 606 pp.

Tziperman, E., 1997: Inherently unstable climate behaviour due to weak thermohaline ocean circulation. *Nature,* **386(6625)**, 592-595.

Tziperman, E., and P. J. Ioannou, 2002: Transient growth and optimal excitation of thermohaline variability. *J. Phys. Oceanogr.,* **32**, 3427-3435.

Tziperman, E., J. Toggweiler, Y. Feliks, and K. Bryan, 1994: Instability of the thermohaline circulation with respect to mixed boundary conditions: Is it really a problem for realistic models. *J. Phys. Oceanogr.,***24**, 217-232.

Tziperman, E., Laure Zanna, and Cecile Penland, 2008: Nonnormal Thermohaline Circulation Dynamics in a Coupled Ocean-atmosphere GCM. *J. Phys. Oceanogr.,* **38**, 588-604.

Vellinga, M., 1996: Instability of two-dimensional thermohaline circulation. *J. Phys. Oceanogr.,* **26**, 305-319.

Vellinga, M., and R. A. Wood, 2002: Global climatic impacts of a collapse of the Atlantic thermohaline circulation. *Climatic Change,* **54**, 251-257.

Vellinga, M., and P. Wu, 2004: Low-latitude freshwater influence on centennial variability of the Atlantic thermohaline circulation. *J. Climate*, **17**, 4498-4511.

Weaver, A., C. Bitz, A. Fanning, and M. Holland, 1999: Thermohaline circulation: high-latitude phenomena and the difference between the Pacific and Atlantic. *Annual Reviews,* **27**, 231-285.

Weaver, A. J., and T. M. C. Hughes, 1994: Rapid interglacial climate fluctuations driven by North Atlantic Ocean circulation. *Nature*. **367**, 447-450.

Weaver, A. J., and E. Sarachik, 1991: Evidence for decadal variability in an ocean general circulation model: An advective mechanism. *Atmosphere-Ocean,* **29**, 197-231.

Weisse, R., U. Mikolajewicz, and E. Maier-Reimer, 1994: Decadal variability of the north Atlantic in an ocean general circulation model. *Journal of Geophysical Research*, **99**(C6), 12411-12421.

Winton, M., and E. S. Sarachik, 1993: Thermohaline oscillation induced by strong steady salinity forcing of ocean general circulation models. *J. Phys. Oceanogr.*, **23**, 1389-1410.

Wood, R. A., M. Vellinga, and R. Thorpe, 2003: Global warming and thermohaline circulation stability, *Philos. Trans. R. Soc. London. Ser. A,* **361**, 1961-1975.

Wright, D. G., and T. F. Stocker, 1991: A zonally averaged ocean model for the thermohaline circulation. Part I: Model development and flow dynamics. *J. Phys. Oceanogr.,* **21**, 1713-1724.

Wright, D. G., and T. F. Stocker, 1992: Sensitivities of a zonally averaged global ocean circulation model. *J. Geophys. Res.,* **97(C8)**, 12707-12730.

Wright, D. G., C. B. Vreugdenhil, and T. M. C. Hughes, 1995: Notes and correspondence: Vorticity dynamics and zonally averaged ocean circulation models. *J. Phys. Oceanogr.,* **25**, 2141-2154.

Wunsch, C., 2002: What is the thermohaline circulation? *Science*, **298**, 1179-1181.

Zanna, L., and E. Tziperman, 2005: Nonnormal amplification of the thermohaline circulation. *J. Phys. Oceanogr*., ***35, 1593-1605.***

Zanna, L., and E. Tziperman, 2008: Optimal Surface Excitation of the Thermohaline Circulation. *J. Phys. Oceanogr.,* **38**, 1820-1830.

Zavala-Garay, J., A. M. Moore, C. L. Perez, and R. Kleeman, 2003: the response of a coupled model of ENSO to observed estimates of stochastic forcing. *J. Climate*, **16**, 2827-2842.